UCRL-11997

University of California

Ernest O. Lawrence Radiation Laboratory

OPTICAL TECHNIQUES FOR THE STUDY OF PHASE BOUNDARIES

Berkeley, California

DISCLAIMER

Gordon Research Conference
on Electro Chemistry - Santa
Barbara, Calif. Jan. 28, 1965
Proceedings -

UCRL-11997

UNIVERSITY OF CALIFORNIA

Lawrence Radiation Laboratory
Berkeley, California

AEC Contract No. W-7405-eng-48

OPTICAL TECHNIQUES FOR THE STUDY OF PHASE BOUNDARIES

Rolf H. Muller

April, 1965

OPTICAL TECHNIQUES FOR THE STUDY OF PHASE BOUNDARIES*

Rolf H. Muller

Inorganic Materials Research Division,
Lawrence Radiation Laboratory
University of California
Berkeley, California

ABSTRACT

Principle, capability and limitation of certain optical techniques suitable for the study of surfaces and boundary layers are discussed. Techniques considered are: interferometry, flow tracing, Schlieren-optics, ellipsometry and film interference.

* Invited paper presented at the Gordon Research Conference on Electrochemistry, Santa Barbara, California, January 28, 1965.

Introduction

Phase boundaries are of interest in many branches of chemical science and technology. In particular, the solid-liquid phase boundary and the heterogeneous reactions occurring on it are prominent in electrochemical systems.

For the purposes of this discussion, two domains of an electrochemical interface may be differentiated (Fig. 1). The immediate neighborhood of the interface, often called "the surface", is a zone in the order of 100 Å thick. It contains transitional layers of atomic dimensions on both the liquid and the solid side of an imaginary line separating the two phases. This includes adsorbed and chemisorbed layers, lattice distortions and other factors affecting the chemical properties of the interface under static conditions. Kinetic parameters and catalytic activity depend on the characteristics of this domain. On the other hand, when a net reaction takes place across the interface at a finite rate, the associated mass transfer results in the formation of a boundary layer in the fluid phase with a typical dimension of 0.1 mm or 10^6 Å. The concept of boundary layers has been introduced in 1904 by Prandtl and is here taken to designate a zone near the phase boundary in which the properties of the fluid phase are different from those in the bulk.[1] Such properties may be concentration, temperature, flow velocity and the like. Phenomena in boundary layers primarily determine the rate of mass (or heat) transfer across the interface and are responsible for the limited rates of many electrochemical processes of technical interest.

The following is a discussion of optical techniques which I have found useful for the study of the interfacial domains outlined above. The techniques to be considered are interferometry, flow tracing and Schlieren optics for boundary layer phenomena (Table 1). Ellipsometry is used for the immediate neighborhood of the phase boundary and film interference when a gaseous phase is present in addition to the solid and the liquid.

Light is, in several respects, ideally suited as a probe for such studies because it allows continuous measurements with a minimum of disturbance to the object, does not require a special test environment, such as high vacuum, and allows good geometrical resolution. Also, several techniques result in photographs which are intuitively understandable, at least in a semi-quantitative way. Optical techniques are best suited for one or two-dimensional situations because the propagation direction of the light is not equivalent to the other two dimensions of space. In other words, it is desirable that the probe encounters over its path the same value of the variable to be measured. Otherwise, the compound effect which results from successively traversing areas of different properties is difficult to analyze.

If light is employed as a probe, various of its properties can be used to gain information about the medium traversed, as indicated in Table 2. As part of the electromagnetic spectrum, light possesses the properties of frequency and intensity which are widely used in colorimetry, spectroscopy, microscopy and similar techniques not to be discussed further here. Moreover, as a consequence of the transversal nature of light waves, the state of polarization is another measurable property

which has long been used by chemists working with optically active compounds. Changes in the direction of polarization of linearly polarized light are measured there. The more general case of elliptic polarization is analyzed in a technique appropriately called ellipsometry. Among the applications of ellipsometry to be discussed, its sentitivity to very thin adsorbed or reacted transitional layers is unique, reaching the atomic level. Two other topics to be discussed, Interferometry and Schlieren optics, are based on measuring changes in phase and propagation direction in density fields. The measured quantities are density in one case and its derivative, the density gradient in the other. Light interference can also be used for the measurement of relatively large film thicknesses, that is in the order of the wavelength of light.

Interferometry

The refractive index of a solution depends on the concentration. In many cases the relationship is almost linear over a wide concentration range, as illustrated for aqueous copper sulfate in Figure 2. The physical meaning of the refractive index as the inverse light propagation rate relative to that in vacuum is formulated in Table 3. Light travels more slowly in a medium of higher refractive index or, since the frequency stays the same, its wavelength is shorter.

The consequence of the above relationship is illustrated in Figure 3. Two tanks of identical geometry are filled with solutions of different concentration such that the upper tank possesses the higher refractive index. Light which enters the tanks in phase shows a phase difference after traversing them, due to the different propagation rates. This

difference is proportional to the refractive index difference Δn and the length d. It is convenient to define the optical path difference as the product of the two, as given in Table 4. The corresponding phase difference can, for instance, be expressed in number of wavelengths.

Figure 4 illustrates the one-dimensional refractive index field in a stratified tank A, where the phase difference is a function of location. Let us assume that the phase difference with respect to tank B, which serves as a reference of uniform refractive index, be zero in the center and plus or minus one half wave at the edges. A suitable superposition of the two beams issuing from both tanks then results in alternate dark and bright franges due to destructive and constructive interference. It is the purpose of an interferometer to provide the two light beams which possess a stationary point-by-point phase relationship or are coherent* with each other and to superimpose the resulting beams in order to make the phase differences visible as intensity variations.

The following are two examples of one-dimensional refractive index fields, mapped interferometrically as outlined above. Figure 5 represents the electrophoretic separation of blood serum in a rectangular cell according to Lotmar.[3] The fringe pattern seen in the bottom has been evaluated by plotting the refractive index gradient corresponding to one wavelength phase difference between fringes versus the fringe position.

---

* This classical definition of coherence, necessary for time-independent interference, does not include the requirements of uniform phase over a cross-section of the beam nor monochromaticity more recently associated with the term in connection with laser optics.

The different components show up as steps in the curve. Figure 6 shows the diffusion of two differently concentrated solutions at increasing times from an initially sharp boundary. Diffusion coefficients approaching differential diffusion coefficients can be determined from such data if concentration differences are kept small. It should be noted that in the examples just discussed, a phase difference of a fraction of a wavelength does not result in an additional fringe and has to be estimated by interpolation. This shortcoming is avoided by techniques which employ the displacement of fringes originally present, rather than their formation on a uniform background, and will be discussed next.

Jamin Interferometer

An interferometer which I have used extensively and would like to discuss in some detail is named after Jules Jamin, a French physicist, who lived 1818-86. As shown in the plan view diagram Figure 7, separaing and recombining of the coherent beams is accomplished by two plano-parallel glass plates. Collimated light is partially reflected on the front and back side of the first plate. Of the two resulting beams one passes through the object under investigation, in this case the vicinity of an electrode surface, the other serves as a reference, passing through the uniform bulk solution. After re-combination by the second plate a diaphragm selects the desired reflections. Usually, the plates are slightly tilted with respect to each other around a horizontal axis, which results in a series of horizontal interference fringes. The image formation is somewhat complicated by the necessity to simultaneously bring in focus the fringes of virtual origin at infinity and the cell

at a finite distance. To this end, a cylindrical lens of vertical axis is used which focuses the cell in the horizontal direction and does not disturb the interference fringes because it acts as a planoparallel plate in the vertical direction. Vertical* fringes in a Jamin interferometer have been made possible with optical compensating plates introduced by Antweiler (Figure 8). The aspherical optics are also necessary in this arrangement, thus limiting the application of both forms of the Jamin interferometer to one-dimensional refractive index fields.

Examples of Jamin interference pictures are given in Figure 9. The top shows the shadow of the electrode on the right. The area representing the solution is filled with interference fringes due to the permanent phase differences introduced by the tilting of the interferometer plates. These fringes become displaced vertically by the refractive index differences in the mass transfer boundary layer shown below. The distance drawn in as a scale represents a length of one millimeter normal to the electrode surface. Since each interference fringe represents a contour line of constant optical path difference, it gives a direct plot of concentration versus distance and can be evaluated as indicated in Figure 10. A typical result in the appropriate coordinate system is given in Figure 11. The measured points lie close to a computed curve. One can thus arrive at the concentration decrease at a cathode relative to the bulk solution which is 5 millimols per liter in this example and illustrates the sensitivity of the method. Furthermore, one can

---

* More exactly, fringes normal to the plane containing the two coherent beams.

measure the concentration gradient at the interface and the thickness of the boundary layer. The dependence of the boundary layer thickness on current density under natural convection is shown in Figure 12 for two heights on a vertical electrode. The slope of the line of -0.16 compares with a 0.2 power relationship derived by the theory of von Karman and Polhausen. Data for the concentration gradient at the interface, where mass transfer occurs by diffusion and migration only, are given in Figure 13.

An application of interferometry to diffusion studies taken from a paper by Svensson[9], is illustrated in Figure 14. The arrangement of a Rayleigh interferometer, which will not be further discussed, has been used here. The differentiation has been accomplished mechanically by slight displacement of two identical diffusing boundaries, but is also possible by purely optical means.[10,11]

A particular application of the Jamin interferometer to a two dimensional situation, illustrated in Figure 15, is due to Antweiler.[12] The interferometer plates are oriented parallel to each other, which results in a uniform intermediate intensity of the image. Changes in refractive index produce intensity variations and result in streaks similar to those obtained by Schlieren optics. For this resemblance, the somewhat misleading title of "interferomatric Schlieren optics" has been given to this technique. The pictures illustrate the turbulence of the boundary layer on a mercury drop, which results in a polarographic maximum, as compared to the normal boundary layer shown on the left. The intensity variations are parts of interference fringes and, therefore, originate at infinity. To focus them simultaneously with the

mercury drop, an objective with small aperture (and large depth of field) has been used.

Mach - Zehnder Interferometer

The mapping of two-dimensional refractive index fields by interferometry is rather complex. The most versatile instrument for this purpose is the four-plate or Mach-Zehnder Interferometer schematically shown in Figure 16. The independent orienting of the four reflecting surfaces allows the virtual origin of the interference fringes to be placed in the object, thus bringing both in focus with a stigmatic (spherical) objective. The boundary layer on a flat electrode under forced turbulent convection, shown in Figure 17, has been obtained with a Mach-Zehnder Interferometer by Lin, Moulton and Putnam.[13] A more striking example of a two dimensional refractive index field is given in Figure 18 showing a tube slightly heated above the surrounding air. Here a downward displacement of the interference frings corresponds to an increase in local temperature.

Multiple beam interference between reflecting cell walls has been employed more recently by O'Brien[15] for the interferomatic observation of two-dimensional refractive index fields. This technique requires only a rather simple optical arrangement, but may be limited by a cumulative effect of light deflection which has not yet been analyzed.

Characteristics of Interferometric Techniques

Table 5 gives a summary on interferometric techniques. They all measure the refractive index and most of them require a considerable

instrumental effort. However, the results can be easily evaluated with great precision. The sensitivity to small refractive index changes is proportional to the cell dimension in the propagation direction of the light. This dependence is shown in Figure 9 under the conservative assumption of 0.1 fringe displacement as sensitivity limit. It results in 2 x 10^{-4} M sensitivity for a 1 cm path. The limitations with respect to large refractive index gradients are due to the optical resolution of closely spaced interference fringes and the light deflection in index gradient fields, which will be discussed below. Geometrical resolution which can be obtained with interference optics is good because large numerical apertures can be employed with most arrangements.

Light Deflection

Interferometric measurements are of limited use for high refractive index gradients because of the light deflection in the gradient field (which forms the basis fo the Schlieren techniques). This light deflection is directed toward the higher refractive index, as indicated in Figure 20. It follows a hyperbolic cosine curve in a field of constant refractive index gradient k normal to the light propagation direction and can be approximated by $y \approx y_o + kx^2/2\, n_o$.* The angle of

---

* y = ordinate

y_o = ordinate at cell entrance

k = refractive index gradient

x = abscizza from cell entrance in original propagation direction

n_o = refractive index at entrance point

deflection α_1, calculated for such a case by the equation $\tan \alpha_1 \approx y/n_o\, k$, is shown in Figure 21, with the current densities of copper deposition producing the corresponding gradients at the interface drawn below the abscizza.

Light deflection has several effects on the interferogram. The lateral displacement a of the image (Figure 20) is illustrated in Figure 22. As an example, with a refractive index gradient at a 1 mm wide electrode corresponding to 24 mA/cm^2 current density the light deflection amounts to 15 microns, which is just noticeable. The deflection a depends on the square of the cell dimension y and is proportional to the index gradient k. The second effect caused by light deflection is a change in optical path due to the greater geometrical length of the curve compared to a straight beam and its passage through zones of different refractive index. It can be approximated by $d \approx -k^2x^3/6n_o$ * and is illustrated in Figure 23. For a cell of 1 mm depth and an index gradient corresponding to 24 mA/cm^2 current density the optical path error due to light deflection is 0.2 micron or about half a wavelength, which is certainly discernible. A third effect of light deflection concerns areas of changing refractive index gradients, where the superposition of beams from different paths can lead to a blurring of the interference fringes. The double-valuedness resulting at the edge of a Nernst-type diffusion layer is illustrated in Figure 24 and numerical computations for the same idealized situation

---

* d is the difference in optical path between the deflected beam and the undeflected issuing from the same point at the cell exit.

are presented in Figure 25. The dotted line indicates the interference pattern expected, without considering the effects of light deflection, and the shaded areas mark the shadows of the electrode surface with and without deflection. Under the assumptions of this analysis the fringe pattern shows a shift giving, surprisingly, an almost correct interfacial concentration and a blurred outer edge of the diffusion layer. In a real system with a smooth transition between boundary layer and bulk, the geometrical displacement and the multi-valuedness in the outer edge will be less severe, thus the apparent boundary layer thickness is smaller than the real one.

Flow Tracing

Hydrodynamic boundary layers on interfaces can be studied by microscopic flow tracing using suspended particles in the fluid. Typical velocity profiles obtained this way of the natural convection at a vertical electrode are given in Figure 26. Note that these hydrodynamic boundary layers are about an order of magnitude larger than the mass transfer boundary layers discussed above. The difference is due to the differences in diffusive transport of mass and momentum, expressed by the Schmidt number $Sc = \nu/D$, which is in the order of 1000, in the cases considered. A very different situation exists for the heat transfer in air, where both boundary layers are of the same dimension ($Pr \approx 1$). It is characteristic for the natural convection at a vertical electrode that the velocity maximum is located very close to the interface, about at the edge of the diffusion layer. The resulting large velocity gradients close to the interface account for the efficient stirring action of natural

convection despite its small velocity. As can be seen in Figure 26, with increasing current density the maximum velocity increases and moves closer to the interface. The respective relationships are shown in Figures 27 and 28. The measured values lie close to the theoretically expected dependence of $i^{2/5}$ and $i^{-1/5}$, respectively. The solid and dotted lines represent theoretical results according to different computational procedures[16].

Figure 29 shows time exposures of suspended particles near a vertical cathode. The first is a normal natural convection situation corresponding to the velocity profiles shown previously. The center picture shows a transitional stage of flow reversal which appears after extended periods of electrolysis at high current densities. The downward motion is due to the stratification in the cell. Diluted solution accumulated in the upper regions exerts a downward buoyancy force on the more concentrated solution which is drawn up from the lower parts. The fully developed flow reversal, shown at right, represents a drastic departure from the original hydrodynamic situation. Motion is confined to a very narrow zone while most of the liquid is at rest. This suppression of natural convection is analogous to the one caused by atmospheric temperature inversion. The strange concentration profiles associated with flow reversal on electrodes are illustrated in Figure 30. The concentration maxima and minima are due to the viscous transport of solution in the vertical direction and are not optical artifacts. Figure 31 gives a quantitative example of the abnormal concentration and velocity profiles under conditions of flow reversal.

Schlieren Optics

Schlieren methods are named by the German word "Schliere", most closely translated by "streak", which designates optical inhomogeneities of the type observed over a hot highway in the sun or around a dissolving sugar cube in a tea cup. Schlieren optics transform the rather elusive appearance of such refractive index fields into pictures which can be evaluated quantitatively. Let us consider again a stratified tank (Figure 32). A plane wave front may enter the tank normal to the window. Due to the more rapid propagation in the area of lower refractive index sketched for a certain increment of time the orientation of the wave front is changed in the tank. This amounts to a change in propagation direction or a curved light path. As long as small angles are involved the deflection ϵ is proportional to the derivative of the refractive index normal to the propagation direction.

Of the large number of ways in which these small angle deflections can be recorded, the shadowgraph technique illustrated in Figure 33, although not amenable to quantitative evaluation, is the simplest. If a point source casts a shadow of a transparent object, the light-deflecting optical inhomogeneities in it appear as areas of decreased intensity on the screen. The areas of increased intensity caused by the deflected light bear no simple relationship with the geometry of the optical disturbance. The Schlieren Shadowgraph technique has been used by Wranglen[17] to show the transition from laminar to turbulent boundary layers on vertical electrodes under natural convection (Figure 34).

A Schlieren method for the quantitative evaluation of a one-dimensional refractive index field is the Philpot-Svensson method

illustrated in Figure 35. Here, the vertical light deflections due to the stratified solution in the cell are transformed into horizontal displacements by an inclined slit. The simultaneous focussing of the cell in the vertical direction and the inclined slit in the horizontal direction by a cylindrical optics results in a plot of cell dimension versus angle of deflection or refractive index gradient. A typical example is the electrophoretic separation of plasma shown in Figure 36, together with its evaluation in terms of superimposed Gaussian curves.

In the Toepler Schlieren arrangement, the angle of deflection is transformed into a proportional intensity variation of the light. This is particularly useful for the observation of two-dimensional refractive index fields and can be accomplished in numerous ways, for instance, as illustrated in Figure 37 by partially intercepting the image of the light source with a knife edge. Light deflection in the object results in a lateral displacement of the image of the light source with respect to the knife edge. Thus, the light intensity available to the objective for the formation of the image of the object depends on the local angle of deflections. Toepler's arrangement results in pictures like that of a shock wave originating from an electric spark shown in Figure 38. Here, each shade of gray corresponds to a certain refractive index gradient. The refractive index profile one obtains by numerical integration corresponds to the relief-like appearance of the picture easily discernible by inspection. You will note that along a horizontal center line in Figure 38, the index gradient is completely undetermined because the light deflection parallel to the knife edge does not result in a change in intensity. The Schlieren picture of an anodically dissolving

lead electrode using a vertical knife edge is shown in Figure 39.

The quantitative evaluation of Toepler Schlieren pictures by integrating microdensitometry is rather tedious. If finite increments of different shades of gray are replaced by different colors, the evaluation becomes much simpler although less precise. Figure 40 shows an arrangement for this purpose where the knife edge is replaced by a series of differently colored stripes. These optics have been used by Brauer[20] for studies on the heat transfer boundary layer in water (Figure 41).

A different use of color in Schlieren optics has as its purpose the simultaneous measurement of direction and magnitude of the light deflection, rather than just its component normal to the knife edge. Thus, color represents an additional dimension in the picture. A very simple arrangement of this type is shown in Figure 42. While the undeflected light is absorbed by a dark disk in the center, deflected light passes through one of the colored segments which characterize the direction of deflection. The Schlieren picture of natural convection from a horizontal anode Figure 43 is a black-and-white print of a color picture obtained with the above arrangement. One can see the very complex pattern of cellular flow.

Table 6 summarizes some characteristics of Schlieren techniques which all measure the refractive index gradient. This can be done for even large two-dimensional refractive index fields with quite modest equipment requirements. The evaluation of results, however, is simple only on a qualitative level and usually difficult for high accuracy, where the use of densitometers or colorimeters is necessary. Sensitivity is limited for small refractive index gradients, but good for high

gradients. Geometrical resolution is limited because the large levers required for the small angle deflections to result in measurable displacement lead to long optical systems with small numerical aperture.

A comparison of Tables 5 and 6 shows that interference and Schlieren techniques complement each other in several respects. For this reason, the simultaneous use of both has been suggested by several authors and is illustrated in Figures 44 and 45. The first is from a combination of a Rayleigh interferometer and a Philpot-Svensson Schlieren system as applied to free electrophoresis. The second illustrates the different advantages of Toepler Schlieren optics and Mach-Zehnder Interferometer for the interpretation of the complex pattern of standing waves in a supersonic jet.

Ellipsometry

For observations in the immediate neighborhood of the phase boundary, ellipsometry is an eminently suited technique. In the following discussion on the state of polarization, only the electric vector of the electromagnetic radiation will be considered. Its relationship with the equally important magnetic vector is illustrated in Figure 46 for a linearly polarized sinusoidal wave. The schematic of an ellipsometer is given in Figure 47. Light from a monochromatic source is made parallel in a collimator and linearly polarized in a polarizer. Reflection on the object results in elliptic polarization. The elliptic polarization is analyzed by transformation into linear polarization with a compensator, the correct setting of which is determined by an analyzer. Figure 48 shows the decomposition of light waves into two orthogonal

linearly polarized components which are oriented parallel and normal to the plane of incidence. For the incident linearly polarized light, the two components are in phase and usually chosen to be of the same amplitude. After reflection, the two components show a phase difference with respect to each other and are of different amplitude. The resulting vector describes a helix in space the projection of which, on a plane normal to the propagation direction, is an ellipse. Phase difference and amplitude ratio of the two components, which are characteristic for the optical properties of the reflecting interface can be determined from the shape, orientation and sense of rotation of the ellipse. The influence of the phase difference on the ellipse is illustrated in Figure 49. The amplitude ratio determines the form of the rectangle in which the ellipse is inscribed.

The measured quantities phase difference $\Delta = \delta_{||} - \delta_{\perp}$ and amplitude ratio $\tan \psi = R_{||}/R_{\perp}$ can be interpreted in different ways. One is in terms of refractive index n and absorption index κ of the reflecting interface. The interrelation of the two pairs of variables is shown in the complex plane in Figure 50 with Δ as argument, $\tan \psi$ as modulus and n and k as parameters. Either of the two sets of equivalent data characterize the optical properties of a reflecting phase boundary and may be sufficient to predict the kinetic properties of smooth metal electrodes.

Typical values of optical constants determined for different electrode-electrolyte interfaces are given in Table 7. They differ from those expected on the basis of the electrode optical constants determined in an inert atmosphere, taking into account the refractive index of the

electrolyte, treated as an ideal dielectric. The difference appears to be due to ionic adsorption, dipole orientation etc. and suggest a future use of ellipsometry for the study of the electrolytic double layer. Similar discrepancies reported by McCrackin et al[25] for different solvents are reproduced in Table 8. They have been interpreted by the authors in terms of adsorbed moisture on the seemingly dry surfaces.

A particular strength of ellipsometry for surface studies lies in the interpretation of the measurements in terms of the thickness of transitional layers. Such layers may be adsorbed, chemisorbed or reacted and optically transparent or absorbing. A classical example by Winterbottom[26] for Fe_2O_3 on Fe is reproduced in Figure 51. The spiral on the left represents phase change Δ and amplitude ratio tan ψ in the complex plane. The beginning of the curve corresponds to the optical constants of the base material (iron) the end to those of the film material (iron oxide). The film thickness in Angstrom units appears as a parameter along the curve. The dependence of tan ψ and Δ on film thickness is also given in Carthesian coordinates. It can be seen that the sensitivity of the two values for film thickness varies in a periodic fashion. Under favorable conditions, fractions of an Angstrom unit can be resolved. Such capabilities are illustrated in Figure 52 by the adsorption isotherms determined as average film thickness for different alcohol vapors in argon adsorbed on silicon. Similar measurements may be possible for the adsorption from solutions.

Several limitations of film measurements by ellipsometry have to be borne in mind. One is that non-uniform coverage of the observed area is averaged out. As pointed out by Reddy[27], the width of the film thickness

distribution function can be estimated from the deviation of complete extinction in the ellipsometer. Another limitation is due to the necessity of having smooth reflecting surfaces. Submicroscopic variations, again, are averaged out. The determination of transitional layers by ellipsometry is governed by the measurement of two parameters Δ and tan Ψ to which possibly the angle of incidence ϕ may be added.

Eminent problems, at present unresolved, in the application of ellipsometry to electrochemical systems, relate to the space charge present in the electrolytic double layer, the possibility to account for a variability of optical constants in the depth of transitional layers and the possible change of the interfacial properties of the substrate due to the presence of the film cover. Care must also be taken to eliminate or account for the effects of extraneous transitional layers which can form, e.g. on cell windows.

Film Interference

A particular kind of interfacial phenomena concerns the presence of three different phases. Such a situation exists at the solid-liquid--gas interface of a gas electrode. It has been found[29,30,31] that electrolyte films which extend beyond the apparent liquid meniscus can exist on the vertical face of such gas electrodes. This situation, which is of importance for the design of fuel cells, is illustrated in Figure 53. A study has been undertaken to determine the geometry of such films and to find the factors which influence it. Of several techniques which may be considered for the measurement of film thickness as a function of position (Table 9), light interference suggests itself because of the

possibility of continuous observation with a minimum of disturbance to the object by the probe, little requirement for uniform film geometry and good sensitivity for the dimensions involved.

Film interference is due to reflection of an incident wave on front and back side of a film as illustrated in Figure 54. Depending on direction of polarization and angle of incidence, different phase relationships indicated schematically by positive and negative signs lead to destructive or constructive interference in films smaller than half a wavelength as illustrated in Figure 54 a and b. Under the second conditions destructive interference occurs (Figure 54 c) with an additional phase reversal due to the optical path in the film. Before presenting some typical results, I want to dwell on two aspects of this technique which have required special attention before meaningful results could be obtained. The first concerns the equal reflectivity of the two film surfaces, which is desired, but not generally the case, in order to obtain complete extinction under conditions of destructive interference. The second is a more precise consideration of phase change upon metallic reflection which usually is not a complete phase reversal as might be inferred from Figure 54.

Interference in a tapered film under monochromatic illumination results in bright and dark interference fringes. They are spaced at a distance corresponding to a one wavelength optical path increment in the film and are therefore more closely spaced for blue than for red light (Figure 55). The use of white light results in interference colors due to the superposition of many monochromatic fringe patterns. A sketch of the Michel-Levy interference color scale employed with the

polarizing microscope is reproduced in Figure 56. For our purposes the abscissa represents the optical path length in the film. The color series begins with black which means that the two reflections would have to be of exactly opposite phase as a vanishing film thickness is approached. In general, however, this is not the case. Values of the phase change in metallic reflection which were computed from the expected and measured optical constants of typical interfaces are given in Table 11.

Phase Considerations

Figure 57 illustrates the phase considerations necessary for the interpretation of film interference if only the first two reflections R_o and R_1 of an incident wave E are considered. In a typical case*, polarization normal to the plane of incidence, marked $\perp$ in Figure 54 results in a phase reversal for dielectric reflection and 112° phase change in the sense of a phase advance for the metallic reflection with respect to the incident wave.** From the latter value, the delay due to the optical path ΔS in the film has to be subtracted. ΔS depends on refractive index n, film thickness d and angle of refraction ϕ' as shown in the upper right. Thus, the phase of R_1 changes with increasing film thickness in the direction indicated by the double arrow in the complex plane diagram of Figure 57. The sum of the two complex amplitudes, a

---

* Nickel base, KOH film, 75° angle of incidence

** Using the coordinate system for incident and reflected waves shown in Figure 58.

measure of the observed interference intensity, therefore, first reaches a minimum with increasing film thickness, which is shown on the bottom of Figure 57. On the other hand, polarization parallel to the plane of incidence marked || in Figure 57 results in different phase shifts, such that an intensity maximum is first reached with increasing film thickness. As can be seen from Figure 57, the two modes of polarization result in approximately complementary interference patterns. Each of them can be characterized by the net phase change due to reflection δ_{refl} which may be defined as the difference between the phase changes associated with the reflections on the two film surfaces. Typical values of this quantity, which is all too often not considered, are listed in Table 12. The dielectric reflection results in 180° phase change at angles of incidence below Brewster's angle and 180° or 0° above it for polarization $\perp$ and ||, respectively (Table 10). The phase and amplitude change in metallic reflection can be computed from refractive index and absorption index of the interface determined with the ellipsometer for a given angle of incidence. The interdependence of the two pairs of variables is shown in diagrams Figure 59 and 60.*

A generalized chart of interference colors indicated in Figure 61 has been constructed in order to take the phase change due to reflection into account for the determination of film thickness (or optical path in the film) from interference colors. A KOH film on nickel, for instance, results in color series corresponding to horizontal lines at $\delta_{refl} = 68°$ and 312° for the two polarizations. It can be seen that the previously shown Michel-Levy scale is contained in Figure 61 along the horizontal center line and that the colors are not repetitive. The

*A detailed discussion of the absolute phase change in metallic reflection will be contained in a forthcoming report UCRL-11813.

practice of shifting a given color series in the horizontal direction, which has been recommended to account for different phase changes due to reflection, is therefore a poor substitute for choosing the correct ordinate.

Amplitude Matching

Another problem in obtaining light interference in a transparent film on a metal substrate is due to the usually much higher reflectivity of the film-metal interface as compared to the gas-film interface.

Therefore, no complete cancellation of the two waves occurs under condition of destructive interference, resulting in interference fringes of poor contrast or whitish color. Results from a theoretical analysis of this problem are illustrated in Figure 62, showing the amplitude ratio of the interfering reflections as a function of the angle of incidence. For polarization normal to the plane of incidence ($\perp$), the ratio increases with increasing angle of incidence from a very unfavorable figure and reaches the desirable value of one at a certain optimum angle $\phi_\perp$. Polarization parallel to the plane of incidence, on the other hand, results in an initial decrease of the amplitude ratio (or the contrast of the fringes) until at Brewster's angle ϕ_p no interference pattern at all is visible. After that, the complimentary pattern discussed before appears and reaches its optimum contrast at an angle of incidence $\phi_\parallel$, slightly different from $\phi_\perp$.

The application of "optimum angles of incidence" has been vital for the electrolyte film studies to be discussed. These angles depend on the optical constants of the metal as shown for a particular refractive index of the film in Figure 63. In practice, an angle of incidence between

$\phi_{\perp}$ and $\phi_{||}$ typically 75° can be used for both polarizations. The changing appearance of the same film under different angles of incidence and both modes of polarization can be seen in Figure 64. It will be noticed that in addition to their changing contrast the interference fringes show a vertical displacement (in the direction to thicker film regions) with increasing angle of incidence. This shift is due to the dependence of the optical path difference ΔS in the film on the cosine of the angle of refraction ϕ' as expressed in Figure 65. It can be used to ascertain the position of the origin of the film thickness scale as indicated in Figure 65. Although the extrapolation is too long for a precise test of the phase changes used in the data evaluation, it is precise enough to detect a possible error of a full interference order due to the misinterpretation of colors.

The electrolytic cells employed in the film studies are sketched in Figure 66. The polished metal electrodes were of rectangular or cylindrical geometry with counter-electrodes of large surface area located in separate compartments. The electrolyte levels were manipulated by a movable liquid reservoir, and controlled atmospheres were maintained in the cell volume not taken up by the liquid. As a rule, the cells were completely filled for the careful cleaning of the electrode surfaces, then the liquid levels were rapidly lowered at the beginning of an experiment. The subsequent drainage of the film was followed as a function of time. The optical arrangement used for this observation is given in Figure 67. Two collimated light beams, polarized parallel and normal to the plane of incidence, are directed toward the film-covered surface G. The respective reflections are collected by two objectives and

placed by a set of reflecting prisms M side by side on the frame N of a 16 mm movie camera geared for single frame exposure. The image of a clock K is also placed on each frame by the optical system H,I in order to record elapsed time. An automatic interval timer actuated the camera shutter and turned the illuminations off between exposures in order to avoid heating by light absorption. The quantitative evaluation of interference pictures like those shown in Figure 68 results in film profiles as those given in Figure 69 for consecutive times after lowering the liquid level. A stationary film is reached after a period in the order of 10 hours.

Consideration of gravitational and viscous forces only, results in the relationship of film thickness and physical constants, vertical coordinate and time given in Table 13. If this relationship holds, a plot of film thickness versus inverse square root of time should result in a straight line for a given film position and the slope of d^2 vs z/t should be a measure of the film viscosity. Figure 70 illustrates good agreement with the first equation down to a film thickness of about one micron, where a deviation leading to the stationary thickness sets in. The second relationship results in an apparent viscosity which is somewhat higher than that expected for the solution used. The technique may nevertheless be useful for specialized viscosity determinations. (Fig. 71)

The equilibrium film geometry results from a balance of interfacial forces and can therefore be expected to depend on the properties of the solid and liquid phases and the electrical potential applied across the interface. The influence of the electrode material has, in fact, been found and is illustrated in Figure 72 for oxygen-consuming nickel and

silver cathodes reflecting their different interfacial free energies. An effect of the electrochemical polarization also exists. For the system illustrated in Figure 73, higher cathodic polarization results in a thicker film. This phenomenon suggests the use of electrolyte films as an indicator for the determination of the electrocapillarity of solid electrodes. The situation is, however, complicated by the non-uniform distribution of potential, reaction rates and composition in the film.

The film response to variable polarization is illustrated in Figure 74. The transition, again, takes in the order of ten hours. Restoring the original polarization results in the original film profile, thus indicating the existence of an equilibrium situation. For nickel and aqueous potassium hydroxide, more dilute solutions have been found to result in a thinner equilibrium film, the one with distilled water touching the limit of interference color techniques (order of 100 Å). Therefore, if a vertical electrode surface covered by an equilibrium water film is brought in contact with a KOH solution, a thicker film grows against gravity. As shown in Figure 75, the transition also takes in the order of 10 hours.

This concludes the discussion of selected optical techniques as tools for the study of phase boundaries and the many problems of current interest associated with them.

ACKNOWLEDGEMENT

This work was performed under the auspices of the United States Atomic Energy Commission.

The following publishers (listed in alphabetical order) and authors have kindly permitted the reproduction of the figures indicated:

Acta Chimica Scandinavica, Sveävagen 166, Stockholm, Va, Sweden (Figs.14, 34,44).

Addison-Wesley Publishing Company, Reading, Massachusetts 01867 (Figs. 46, 58).

American Chemical Society, Industrial and Engineering Chemistry, 1155 Sixteenth Street, Washington 6, D.C. (Figs. 16, 17).

American Institute of Physics, Review of Scientific Instruments, 335 East 45th Street, New York, New York 10017 (Fig. 6), Dr. W. Lotmar.

Butterworths Scientific Publications, 125 High Holborn, London, W.C. 1, England (Figs. 7, 10, 11, 12, 26), Dr. N. Ibl.

Chimia, Schweizerischer Chemiker Verband, H. W. Sauerländer and Company, Aarau, Switzerland (Figs. 35, 36).

Electrochemical Society Journal, 1860 Broadway, New York, New York, 10023 (Fig. 52).

Journal of the Optical Society, 68 Hammond Street, Rochester, New York 14615 (Fig. 62).

Juris Verlag, Dr. H. Christen, Basteiplatz 5, Zurich 1, Switzerland (Figs. 27, 28).

Kern and Company, Ltd., Optical and Mechanical Precision Instruments, 5000 Aaran, Switzerland (Fig. 5).

Edward Arnold Ltd., 41 Maddox Street, London W.1, England (Fig. 51).

Springer Verlag, Postfach 3027, 69 Heidelberg 1, Germany. Dr. H. Schardin, Dr. M. Françon (Figs. 38, 48, 49).

VDI Verlag GmbH, Postfach 10-250 Dusseldorf, Germany (Fig. 45).

Verlag Chemie GmbH, Pappelallee 3, Weinheim/Bergstr., Germany (Figs. 8, 9, 15, 29, 30, 31, 41).

VEB Carl Zeiss Jena, Carl Zeiss Strasse 1, Jena, German Democratic Republic (Fig. 18).

Thanks are due to Dr. John M. Stone, Department of Physics, University of California, Berkeley, for reviewing the manuscript of this report.

Table 1

Optical Techniques for the Study of Phase Boundaries

Domain	Technique
Boundary layers	Interferometry
	Flow Tracing
	Schlieren optics
"Surfaces"	Ellipsometry
3 Phases	Film interference

Table 2

Optical Techniques in Chemistry

Light Property	Technique	Measured
Frequency	Colorimetry, Spectroscopy	Absorption, Emission
Intensity	Microscopy	Patterns
Polarization	Polarimetry, Ellipsometry	Opt. Activity Film thickness (low)
Phase	Interferometry	Refractive index Film thickness (high)
Propagation Direction	Schlieren optics	Refractive index gradient

Table 3

Definition of Refractive Index

$$n = \frac{c}{v}$$

n refractive index

c light velocity in vacuum

v light velocity in medium n

Table 4

Optical Path and Phase

$$\Delta p = \Delta n \, d \qquad\qquad \Delta z = \frac{\Delta n \, d}{\lambda_o}$$

Δp	optical path difference
Δn	refractive index difference
d	geometrical path length
Δz	phase difference in number of waves
λ_o	wavelength of light in vacuum

Table 5

Characteristics of Interferometer Techniques

Measured quantity	Refractive Index
Instrumental effort	Considerable
Evaluation of results	Simple, precise
Sensitivity for small gradients	Good (2×10^{-4} M)
Sensitivity for large gradients	Limited (10^{-3} M cm^{-4})
Geometrical resolution	Good (20 μ)

Table 6

Characteristics of Schlieren Techniques

Measured quantity	Refractive index gradient
Instrumental effort	Modest (excl. densitometer)
Evaluation of results	Simple if semiquantitative, difficult if exact
Sensitivity for small gradients	Limited
Sensitivity for large gradients	Good
Geometrical resolution	Limited (small aperture)

Table 7

Electrode Surfaces

Apparent Optical Constants

Electrolyte 3.5n KOH

Electrode	Expected		Measured	
	n	K	n	K
C	1.49	0.50	1.19	0.35
Ni	1.28	1.95	0.55	1.40
Ag	0.13	20.6	0.55	2.93

Table 8

Apparent Optical Constants of Chromium Immersed in Different Solvents. Values Computed from Data Reported by McCrackin et al[25]

Angle of Incidence ø	Immersion Medium	Expected n	Expected κ	Measured n	Measured κ
60°	Methanol	2.18	1.44	3.21	1.35
70°	Water	2.18	1.44	3.28	1.33
70°	Acetone	2.15	1.44	3.30	1.33
70°	Cylohexane	2.05	1.44	3.25	1.35
70°	Toluene	1.95	1.44	3.34	1.33

Table 9

Techniques for Film Thickness Measurement

Type	Strength	Weakness
Mechanical	Independence of Electrolyte and Electrode materials	Sensitivity, Discontinuous point to point measurement Disturbance by probe
Electrical	Continuous measurement	Dependence on electrolyte conductivity Uniform film needed Disturbance by probe
Optical	Continuous, 2-dimensional minimum disturbance	Dependence on film refractive index

Table 10

Dielectric Reflection, Phase Change

Angle of incidence > 54°

Electrolyte	δ dielectric	
	$\perp$	$\parallel$
KOH 3.5n	180°	0°

Table 11

Metallic Reflection, Phase Change

Electrolyte 3.5n KOH, angle of incidence 45°

Electrode	δ_{metal} Expected ⊥	Expected ∥	Measured ⊥	Measured ∥
C	150°	120°	133°	105°
Ni	151°	126°	112°	48°
Ag	136°	117°	136°	94°

Table 12

Film Interference

Phase Change Due to Reflections

angle of incidence 75°

electrolyte 3.5n KOH

$$\delta_{refl.} = \delta_{dielectric} - \delta_{metal}$$

Electrode	$\delta_{refl.}$ ⊥	$\delta_{refl.}$ ∥
C	47°	255°
Ni	68°	312°
Ag	44°	266°

Table 13

Film Thinning Under Gravitational and Viscous Forces

$$d = \left(\frac{\mu}{\rho g}\right)^{\frac{1}{2}} z^{\frac{1}{2}} t^{-\frac{1}{2}}$$

$$d^2 = \frac{\mu}{\rho g} \frac{z}{t}$$

d = electrolyte film thickness

μ = electrolyte viscosity

ρ = electrolyte density

g = gravitational constant

z = electrode coordinate from upper edge

t = time

References

1. H. Schlichting: "Boundary Layer Theory" McGraw-Hill, New York (1960[4]).
2. Landolt-Bornstein, HW 2, 989, Springer, Berlin (1923).
3. Kern Optical Company, Micro-Electrophoresis Apparatus LK 30, Pamphlet.
4. W. Lotmar: "An Interferometric Micro-Electrophoresis Apparatus". Rev. Sci. Instr. 22, 886-90 (1951).
5. N. Ibl: "Methods for the Study of the Diffusion Layer". Proc. 7th meet. CITCE pp. 112-33 Butterworth, London (1957).
6. H. J. Antweiler: "Lichtstarkes Messverfahren fuer Sedimentations, Elektrophorese und Diffusionsversuche". Chem. Ing. Techn. 24, 284-8 (1952).
7. N. Ibl, R. Muller: "Optische Untersuchungen der Diffusionsschicht und der hydrodynamischen Grenzschicht an belasteten Elektroden". Z. Elektrochem. Ber. Bunsenges. phys. Chem. 59, 671-76 (1955).
8. N. Ibl, R. Muller, A. Frei, "Study of the Natural Convection at Current Densities Smaller than the Limiting Current Density" Proc. 8th meet. CITCE pp. 179-84 Butterworth, London (1958).
9. H. Svensson: "An Interferometric Method for Recording the Refractive Index Derivative in Concentration Gradients". Acta Chem. Scand. 3, 1170-77 (1949).
10. H. Svensson: as above, "II Arrangement for and Theory of Purely Optical Differentiation of the Refractive Index Function". Acta Chem. Scand. 4, 1329-46 (1950).
11. H. Svensson, R. Forsberg, L. A. Lindstrom: as above, "III The Construction of the Optical Differentiators and Experimental Test of the Method". Acta Chem. Scand. 7, 159-66 (1953).

References (Continued)

12. H. J. Antweiler: "Methoden zur Beobachtung der Diffusionsschicht bei der Elektrolyse". Z. Elektrochem. 44, 719-24 (1938).

13. C. S. Lin, R. W. Moulton, G. L. Putnam: "Interferometric Measurements of Concentration Profiles in Turbulent and Streamline Flow". Ind. Eng. Chem. 45, 640-46 (1953).

14. G. Hansen: "Messung kleiner Brechungsunterschiede durch Lichtablenkung und Interferenz". Zeiss Nachr. 3, 302-12 (1940).

15. R. N. O'Brien: "Interferometer for Electrochemical Investigations". Rev. Sci. Instr. 35, 803-6 (1964).

16. R. H. Muller: "Optische Untersuchungen der natuerlichen Konvektion bei der Elektrolyse". Diss., Juris-Verlag, Zurich, (1956).

17. G. Wranglen: "A Shadow Schlieren Method for the Study of Diffusion Boundary Layers at Electrodes". Acta Chem. Scand. 12, 1543-4 (1958).

18. E. Wiedemann: "Methodik und Anwendungen der Elektrophorese." Chimia 2, 25-35 (1948).

19. H. Schardin: "Die Schlierenverfahren und ihre Anwendungen". Ergebn. Exakt. Naturwiss. 20, 303-439, Springer (1942).

20. H. Brauer: "Schlierenoptische Beobachtungen bei der Waermeuebertragung". Chem. Ing. Techn. 34, 73-78 (1962).

21. H. Svensson: "A Method for Production of High-Intensity, Multi-Fringe Rayleigh Interference Patterns." Acta Chem. Scand. 5, 1301-10 (1951).

22. T. Zobel: "Verwendung von Lichtinterferenzen in der Technischen Messung". Z. Verein deutscher Ingen. 81, 619-24 (1937).

23. B. Rossi: "Optics", Addison-Wesley, Reading, Massachusetts (1959^2)

References (Continued)

24. M. Françon: "Interférence, diffraction et polarisation", Encyclopedia of Physics, 24 S. Flugge, ed., Springer, Berlin (1956).

25. F. L. McCrackin, E. Passaglia, R. R. Stromberg, H. L. Steinberg: "Measurement of the Thickness and Refractive Index of Very Thin Films and the Optical Properties of Surfaces by Ellipsometry." J. Res. Natl. Bur. Standards 67A, 363-77 (1963).

26. A. B. Winterbottom: "Optical Methods for the Determination of Films on Metals etc." Appendix in U. R. Evans: "Metallic Corrosion, Possivity and Protection". Arnold, London (1946^2).

27. A. K. N. Reddy: private communication.

28. H. H. Claussen: "An Ellipsometer Investigation of Vapor Adsorption on Etched Silicon". J. Electrochem. Soc. 111, 646-52 (1964).

29. F. G. Will: "Electrochemical Oxidation of Hydrogen on Partially Immersed Platinum Electrodes. I Experiments and Interpretation, II Theoretical Treatment" J. Electrochem. Soc. 110, 145-51, 152-60 (1963).

30. D. N. Bennion, to be published in J. Electrochem. Soc.

31. R. H. Muller, to be published in J. Electrochem. Soc.

32. R. H. Muller: "Thickness Measurement of Transparent Thin Films on Metal Surfaces by Light Interference." J. Opt. Soc. Amer. 54, 419-20 (1964).

33. E. M. Chamot, C. W. Mason: "Handbook of Chemical Microscopy" Vol. I, p. 489 (Wiley (1958^3)." Vol. I p. 489. Wiley (1958^3).

34. R. H. Muller: "Light Interference in Transparent Thin Films on Metal Surfaces". UCRL-10963, July 1963.

35. D. N. Bennion, private communication.

Figure Captions

Fig. 1. Regions of electrochemical interfaces.

Fig. 2. Refractive index of copper sulfate solutions at 17.5°C in sodium light (Data from Landolt-Bornstein[2]).

Fig. 3. Refractive index and light propagation rate.

Fig. 4. Phase change in one-dimensional refractive index field as basis of interferometer techniques.

Fig. 5. Electrophoretic separation of human serum, descending branch (Kern[3]).

Fig. 6. Diffusion of 10% $CdSO_4$ into 9% $CdSO_4$ solution (Lotmar[4]).

Fig. 7. Jamin interferometer for diffusion layer studies with horizontal fringes (Ibl[5]).

Fig. 8. Jamin interferometer with compensating plates for vertical fringes according to Antweiler (Antweiler[6]).

Fig. 9. Jamin interferometer, interference picture of electrode boundary layer with horizontal fringes. (a) Unpolarized, (b) Cathodic current density 2.2 m A/cm^2, 0.6 M $CuSO_4$ (Ibl and Muller[7]).

Fig.10. Evaluation of concentration profile in boundary layer from interferogram (Ibl[5]).

Fig.11. Interferometrically measured concentration profile in the copper desposition from $CuSo_4$ solution at a current density of 0.32 mA/cm^2 (Ibl, Muller and Frei[8]).

Fig.12. Dependence of diffusion layer thickness on current density on a vertical electrode under natural convection, 0.6 M $CuSO_4$ (Ibl, Muller and Frei[8]).

Fig. 13. Concentration gradient at the interface in copper deposition under natural convection.

Figure Captions (Continued)

Fig.14. Diffusing boundary, concentration and concentration gradient profiles obtained by interferometry (Svensson[9]).

Fig.15. Interferometric Schlieren pictures of the boundary layer on a dropping mercury electrode (Antweiler[12]).

Fig.16. Mach-Zehnder Interferometer (Lin, Moulton and Putnam[13]).

Fig.17. Mach-Zehnder interference picture of electrode boundary layer under turbulent forced convection (Lin, Moulton and Putnam[13]).

Fig.18. Mach-Zehnder interference picture of two-dimensional temperature field around heated tube (Hansen[14]).

Fig.19. Sensitivity of interferometric measurements as a function of cell dimension traversed by the light. Based on $CuSO_4$ in water and fringe displacement of 1/10 fringe spacing as limit of detectability.

Fig.20. Errors due to light deflection in refractive index field.

Fig.21. Angles of light deflection and refraction defined in Fig.20 for cell dimension 0.25 cm in the direction of light propagation.

Fig.22. Lateral distance of light deflection in refractive index gradients k corresponding to 6, 12 and 24 m A/cm^2 in $CuSO_4$.

Fig.23. Error in optical path due to light deflection.

Fig.24. Light deflection in boundary layer of the Nernst type with resulting multi-valuedness at exit.

Fig.25. Fringe pattern computed for Nernst type boundary layer by taking light deflection into account. Refractive index gradient $k = 0.37\ cm^{-1}$, cell dimension $l = 0.25$ cm.

Figure Captions (Continued)

Fig.26. Velocity distribution of natural convection for various current densities. Solution 0.6M $CuSO_4$, total electrode height x = 14 cm, measurement at 7 cm (Ibl, Muller and Frei[8]).

Fig.27. Value of natural convection velocity maximum as a function of current density, electrode height 7 cm (Muller[16]).

Fig.28. Position of natural convection velocity maximum as function of current density, electrode height 7 cm (Muller[16]).

Fig.29. Flow traces of the hydrodynamic boundary layer near a vertical cathode. a) Normal natural convection, b) transition, c) fully established flow reversal due to stratification of the solution (Ibl and Muller[7]).

Fig.30. Abnormal concentration profiles due to stratification of the solution. a) Anode, b) Cathode. (Ibl and Muller[7]).

Fig.31. Velocity and concentration profiles under fully developed flow reversal due to stratification of the solution (Ibl and Muller[7]).

Fig.32. Light deflection by refractive index gradient as basis of Schlieren optical techniques.

Fig.33. Schlieren shadowgraph system.

Fig.34. Shadowgraph of laminar and turbulent boundary layers on vertical electrodes under natural convection (Wranglén[17]).

Fig.35. Philpot-Svensson Schlieren method for one-dimensional refractive index fields (Wiedemann[18]).

Fig.36. Philpot-Svensson diagram of an electrophoretic separation and its evaluation in terms of Gaussian distribution curves. (Wiedemann[18]).

Figure Captions (Continued)

Fig.37. Toepler Schlieren system.

Fig.38. Toepler Schlieren picture of the shock wave from a spark in air, horizontal knife edge (Schardin[19]).

Fig.39. Toepler Schlieren picture of the anodic dissolution of a tube-shaped lead electrode under natural convection, vertical knife edge, 170 m A/cm^2.

Fig.40. Color Schlieren method for differentiating between increments of light deflection in one direction.

Fig.41. Color Schlieren picture of heat transfer boundary layer on vertical tube showing transition from laminar to turbulent natural convection (black and white reproduction, Brauer[20]).

Fig.42. Color Schlieren method for differentiating between directions of light deflection.

Fig.43. Color Schlieren picture of the natural convection from a dissolving horizontal anode, method for differentiating directions of light deflection (black and white reproduction).

Fig.44. Simultaneous use of Rayleigh interferometer and Philpot-Stevensson Schlieren techniques for electrophoresis (Svensson[21]).

Fig.45. Simultaneous use of Mach-Zehnder interferometer and Toepler Schlieren techniques on a radially symmetrical supersonic jet (Zobel[22]).

Fig.46. Electric and magnetic vectors in linearly polarized light (Rossi[23]).

Fig.47. Ellipsometer.

Fig.48. Decomposition of linearly and elliptically polarized light (Françon[24]).

Figure Captions (Continued)

Fig.49. Influence of phase difference on elliptic polarization (Françon[24]).

Fig.50. Relationship of phase difference Δ, amplitude ratio tan ψ, refractive index n and absorption index κ for reflection under 45° angle of incidence.

Fig.51. Effect of an Fe_2O_3 film of increasing thickness on an Fe substrate on the elliptic polarization of the reflected light (Winterbottom[26]).

Fig.52. Adsorption isotherms of different alcohols on an etched silicon surface determined by ellipsometry (Claussen[28]).

Fig.53. Two-dimensional solid-liquid-gas interface with electrolyte film formed on the solid phase.

Fig.54. Film interference, phase relationships of incident and reflected light.

a) for distructive interference with very low film thickness.

b) for constructive interference with very low film thickness.

c) for distructive interference with additional $\lambda/2$ optical path between reflections in the film (Muller[32]).

Fig.55. Interference in a wedge-shaped film with monochromatic light of different wavelengths.

Fig.56. Michel-Levy scale of interference colors for birefringent crystals between crossed Nicol prisms. d = thickness of crystal plate, n_2-n_1 = birefringence, Δs = relative phase retardation. b = blue, w = white, y = yellow, r = red, g = green. (Sketched from color chart given by Chamot[33]).

Fig.57. Film interference, phase relationships.

Figure Captions (Continued)

Fig.58. Coordinate systems used for incident and reflected waves (Rossi[23]).

Fig.59. Relationship of phase δ and amplitude R relative to incident wave for reflection on interface of refractive index n and absorption index κ under 45° angle of incidence. Polarization normal to plane of incidence.

Fig.60. Same as Fig. 59, polarization parallel to plane of incidence.

Fig.61. Generalized scale of interference colors as a function of phase change due to reflection $\delta_{refl.}$ and optical path length in the film Δs. w = white, r = red, b = blue, y = yellow, g = green.

Fig.62. Interference in a transparent film (n = 1.365) on different metal surfaces. Amplitude ratio of interferring reflected waves as a function of angle of incidence for both modes of polarization (Muller[32]).

Fig.63. Optimum angles of incidence for observation of interference in a transparent film (3.5NKOH) on electrodes of optical constants n_2 and κ_2, for both modes of polarization.

Fig.64. Appearance of interference pattern in the same KOH film on Ni under different angles of incidence for both modes of polarization (Muller[34]).

Fig.65. Film interference under different angles of incidence. Extrapolation of optical path length to check origin of thickness scale.

Fig.66. Electrolytic cells for film studies with rectangular and cylindrical electrodes.

Fig.67. Optical arrangement for slow motion movie photography of electrolyte film formation.

Figure Captions (Continued)

Fig.68. Light interference in electrolyte films at different stages of thinning (black and white reproduction of color prints).

Fig.69. Formation of electrolyte film on unpolarized flat nickel electrode 3.5N KOH, N_2.

Fig.70. Formation of electrolyte film on polished nickel surface after withdrawal from the liquid (3.5N KOH, N_2, h = 1.5cm).

Fig.71. Apparent electrolyte viscosity determined from film thinning rate (N_2, h = 1.5cm).

Fig.72. Equilibrium film profiles on different metals (3.5N KOH, O_2, 50 μA/cm).

Fig.73. Equilibrium film profiles on nickel at different current densities (3.5N KOH, O_2, o flat, Δ cylindrical electrodes).

Fig.74. Film response to variable polarization. (3.5N KOH, O_2, flat and cylindrical nickel electrodes).

Fig.75. Film growth on nickel (3.5N KOH on H_2O, h = 1.5 cm, unpolarized).

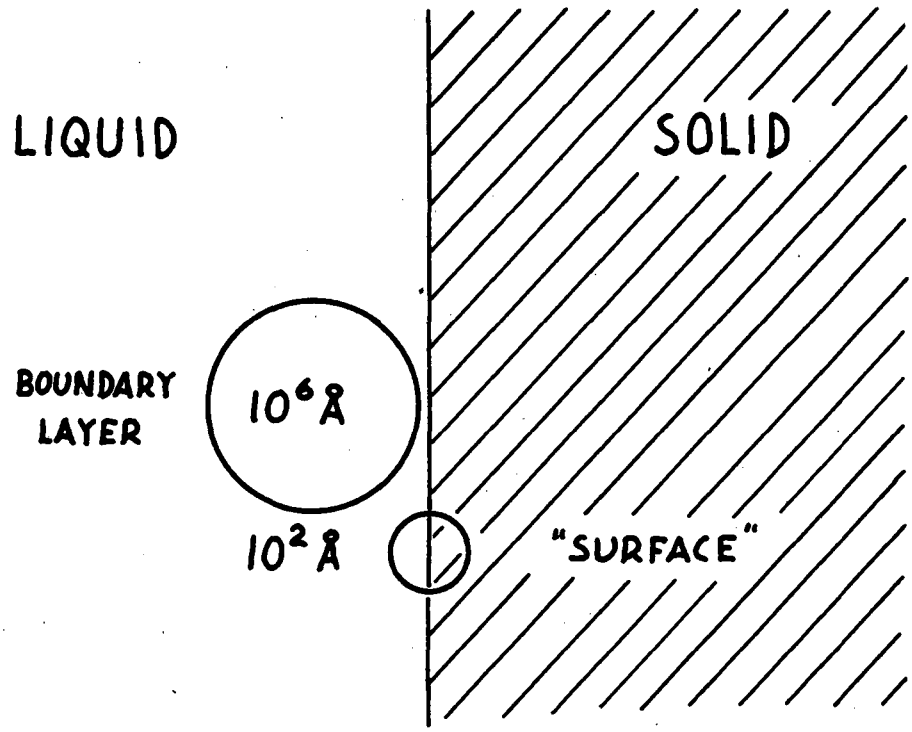

REGIONS OF ELECTROCHEMICAL INTERFACES

MUB-6104

Fig. 1

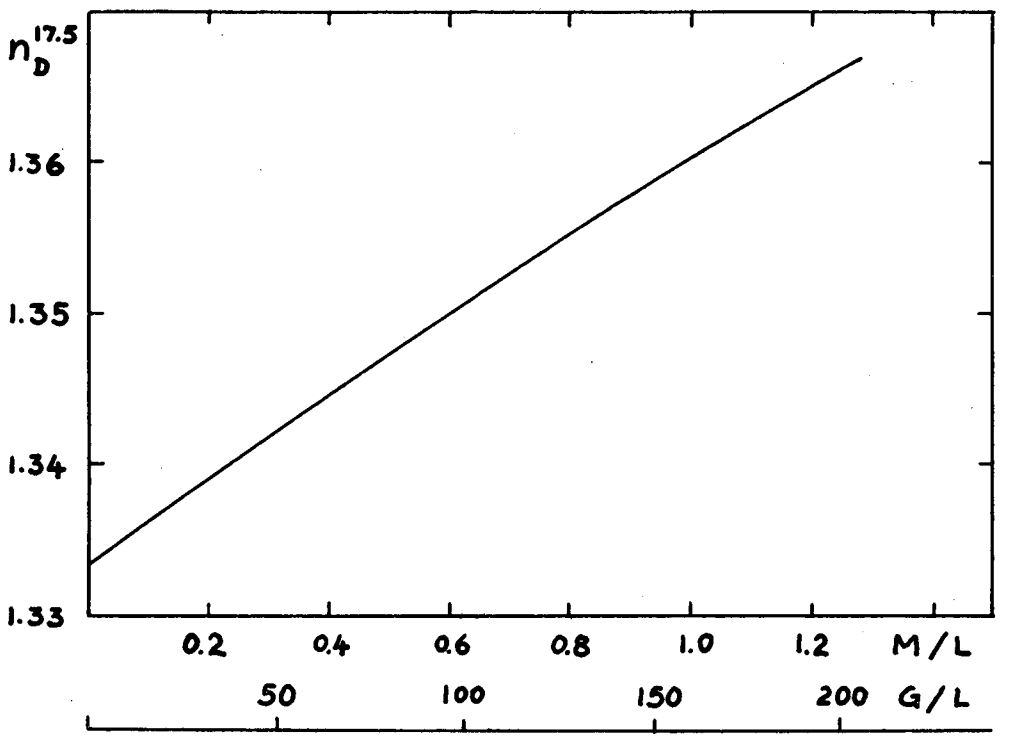

REFRACTIVE INDEX OF COPPER SULFATE SOLUTIONS

MUB-6105

Fig. 2

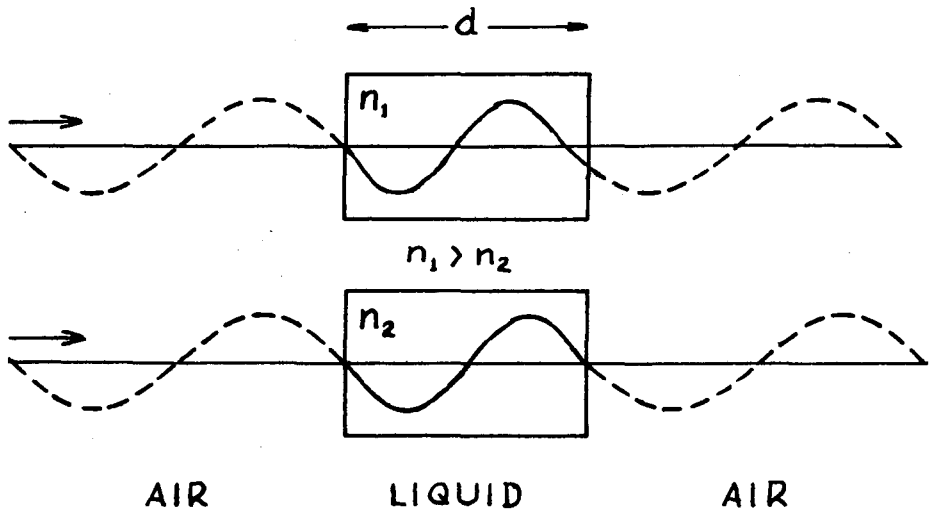

Refractive Index and Light Propagation Rate

MU-35598

Fig. 3

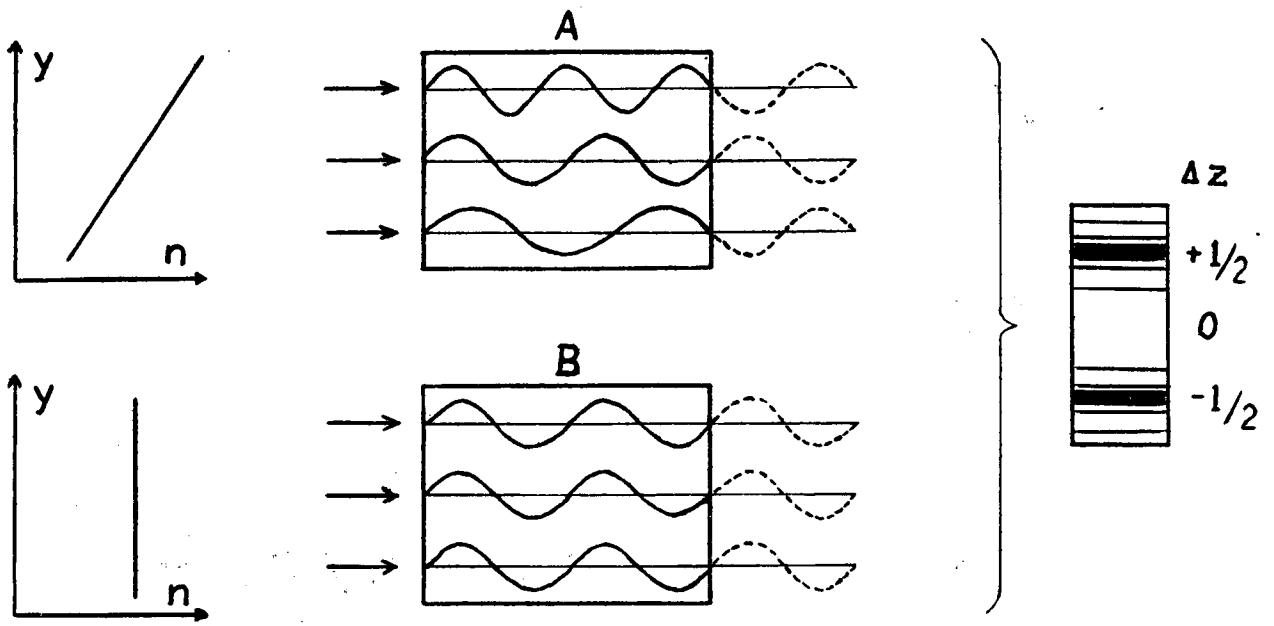

Phase Change in Refractive Index Field

MUB-6106

Fig. 4

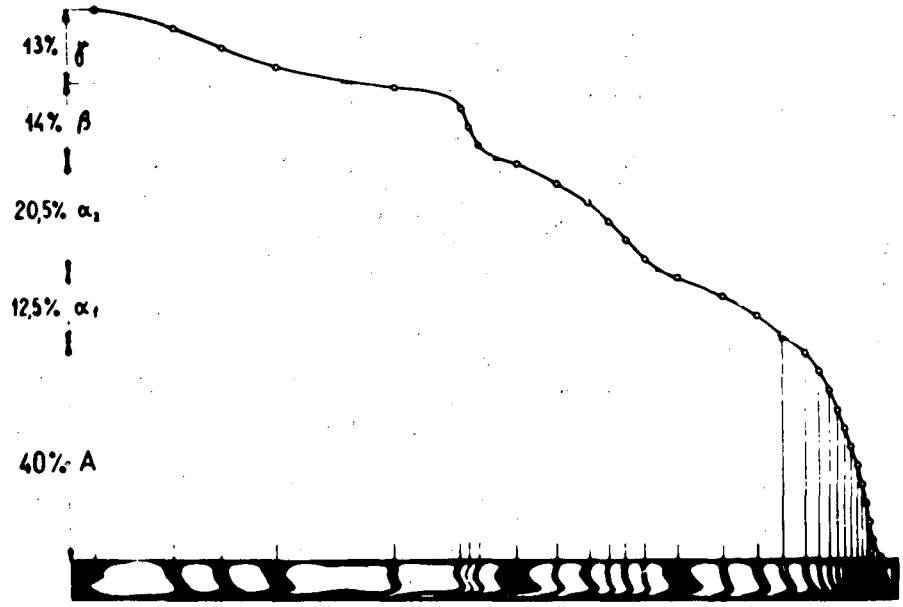

Auswertung einer Aufnahme von normalem menschlichem Serum. Absteigender Ast, Laufzeit 37 ' bei 8,3 V cm. Michaelispuffer.

MU-35623

Fig. 5

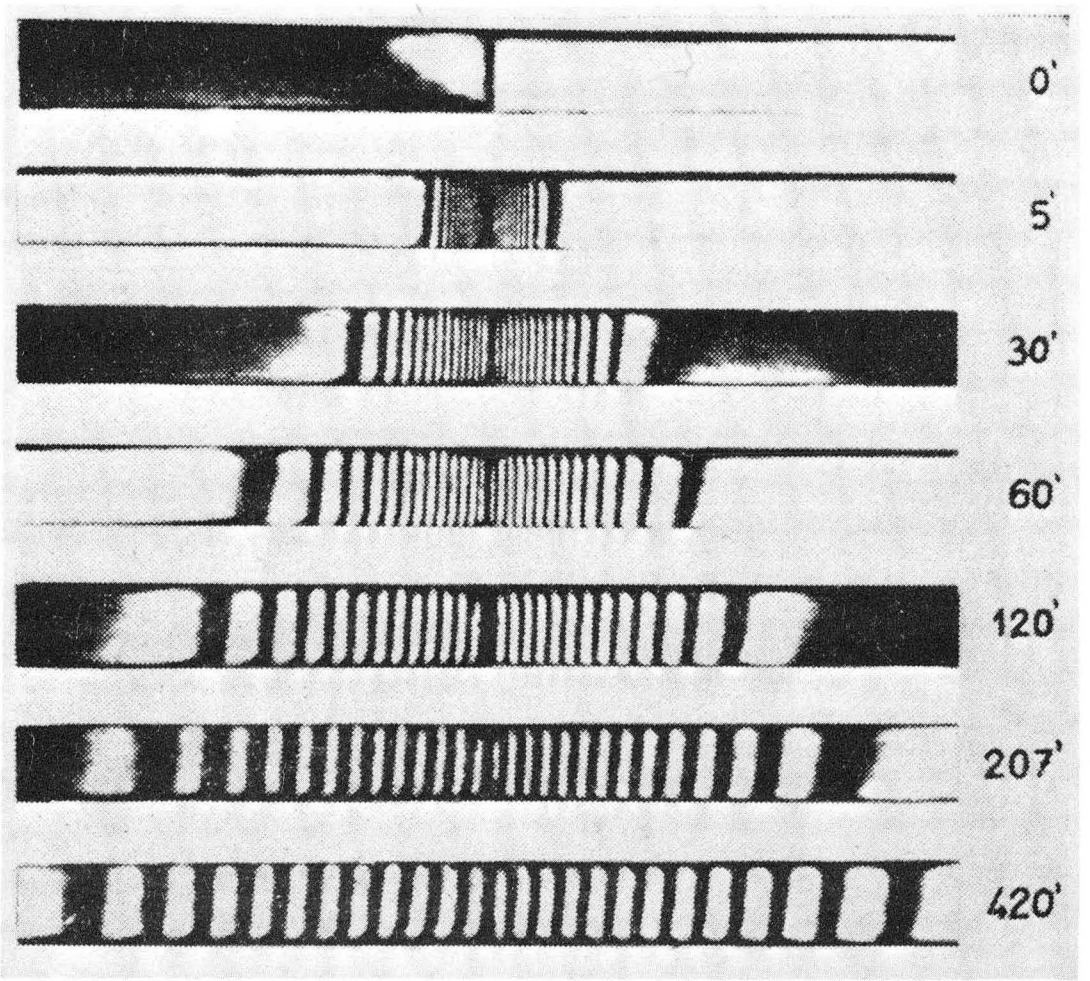

ZN-5131

Fig. 6. Diffusion of 10% cadmium sulfate solution into 9% cadmium sulfate. Magnification 5X.

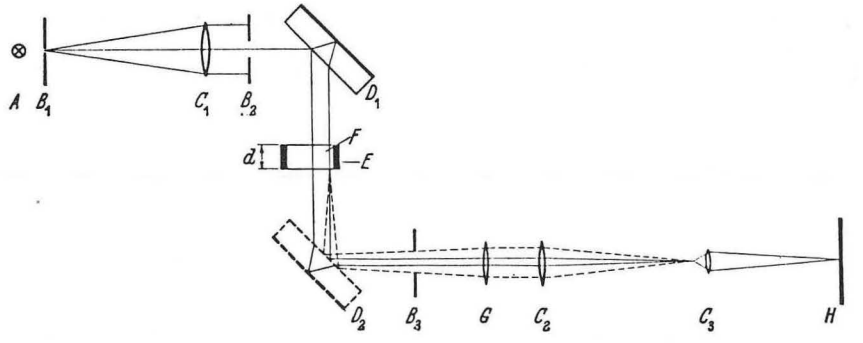

Interferometric arrangement for the direct recording of the concentration distribution
(Ibl, Barrada, and Trümpler[33])

A: light source; B_1, B_2, B_3: diaphragms; C_1, C_2, C_3: spherical lenses; D_1, D_2: Jamin plates; E: electrode; F: electrolysis cell; G: cylindrical lens; H: photographic plate; d: depth of the electrolysis cell

MU-35599

Fig. 7

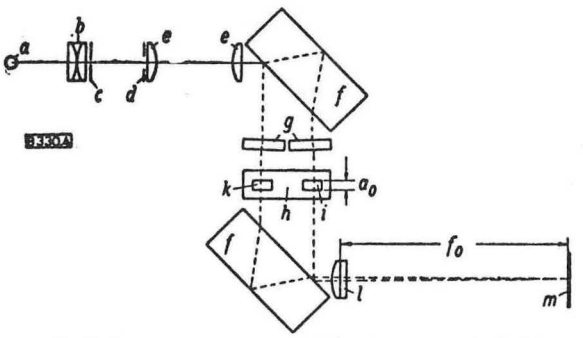

Optische Anordnung des Meßsystems zur Aufzeichnung eines *n*,x-Diagramms
a **Lichtquelle,** ***b*** **Kondensor,** ***c*** **senkrechter Spalt,** ***d*** **Blende,** ***e*** **Linsen,** ***f*** ***Jamin*****-Platten,** ***g*** **Zusatzplatten,** ***h*** **Cuvette mit Meßkanal** ***i*** **und Vergleichskanal** ***k,*** ***l*** **asphärisches Objektiv,** ***m*** **Bildebene im Abstand** f_0 **vom Objektiv,** a_0 **Cuvettentiefe**

MU-35600

Fig. 8

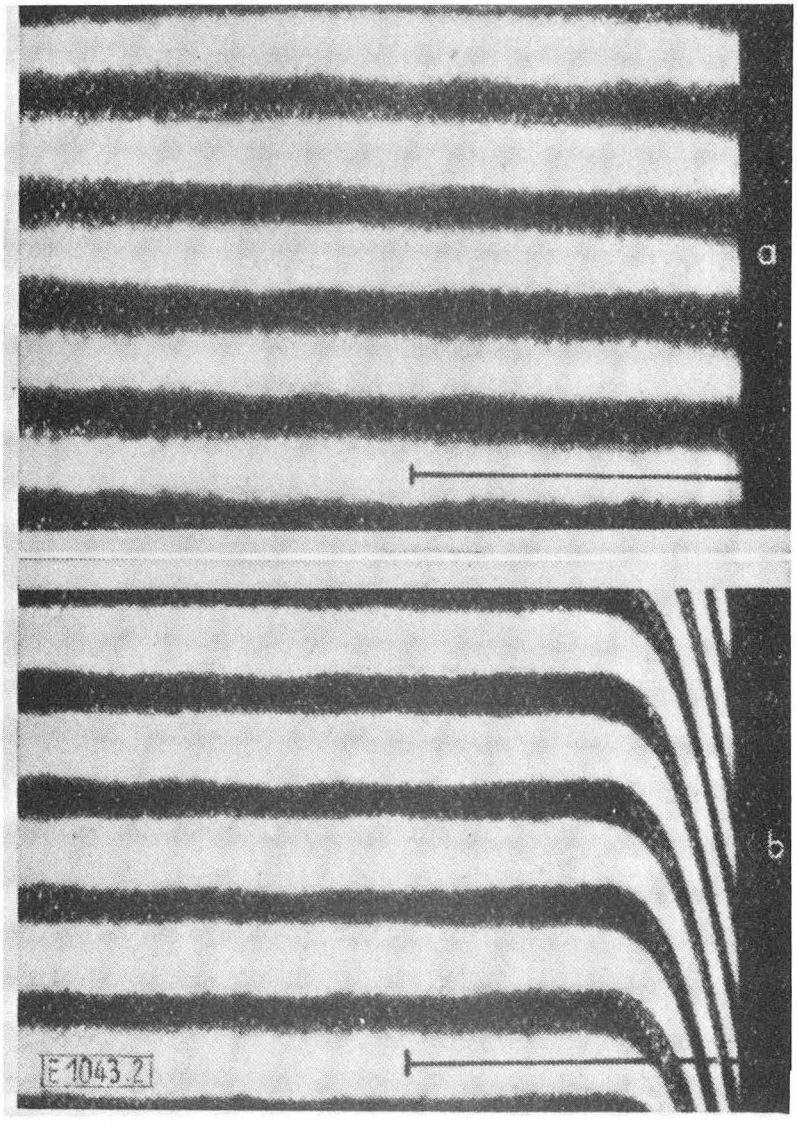

ZN-5132

Fig. 9

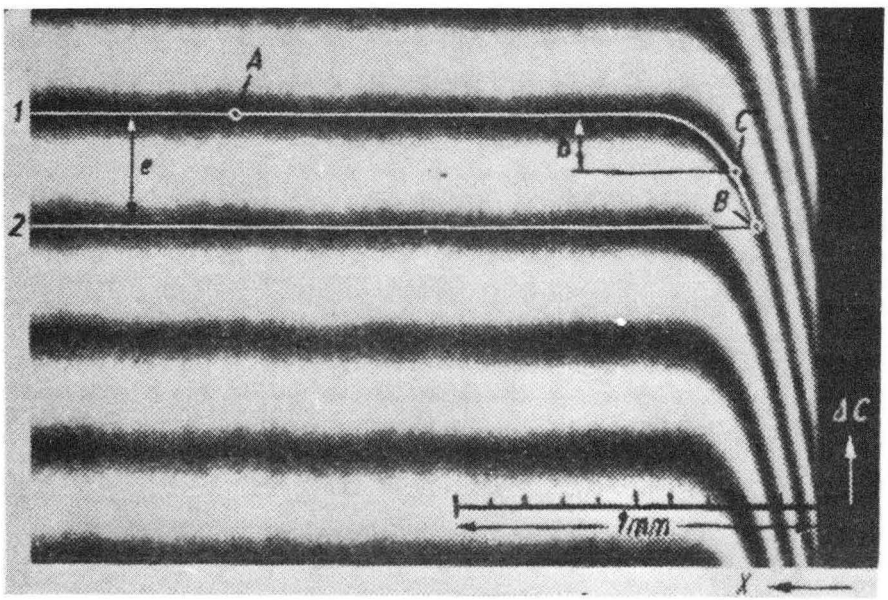

ZN-5133

Fig. 10

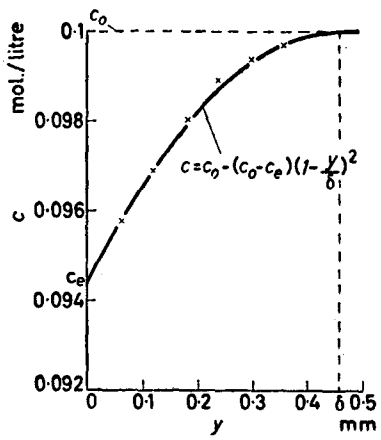

MU-35601

Fig. 11

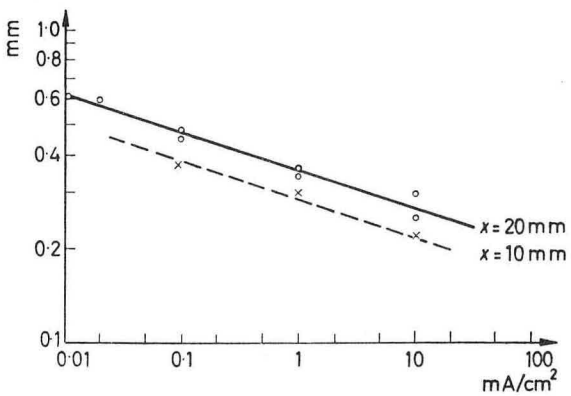

MU-35602

Fig. 12

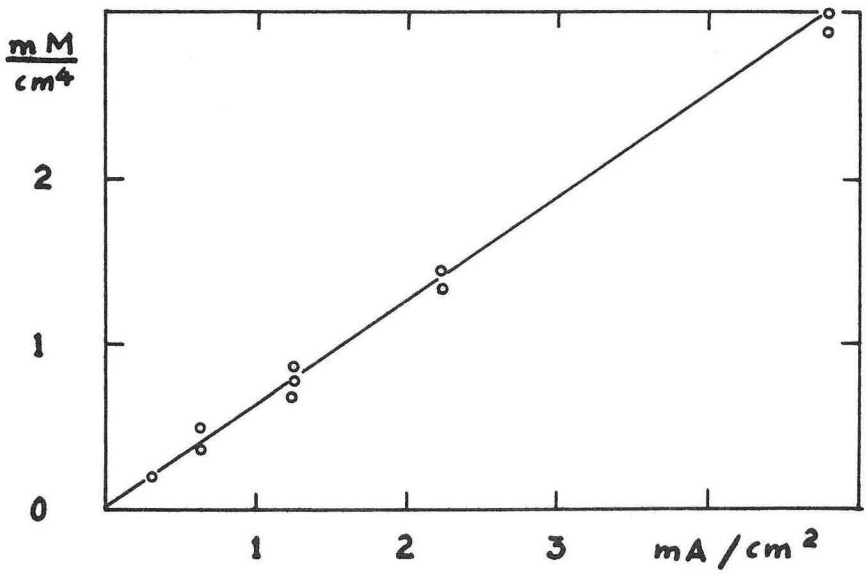

CONCENTRATION GRADIENT AT THE INTERFACE

MUB-6107

Fig. 13

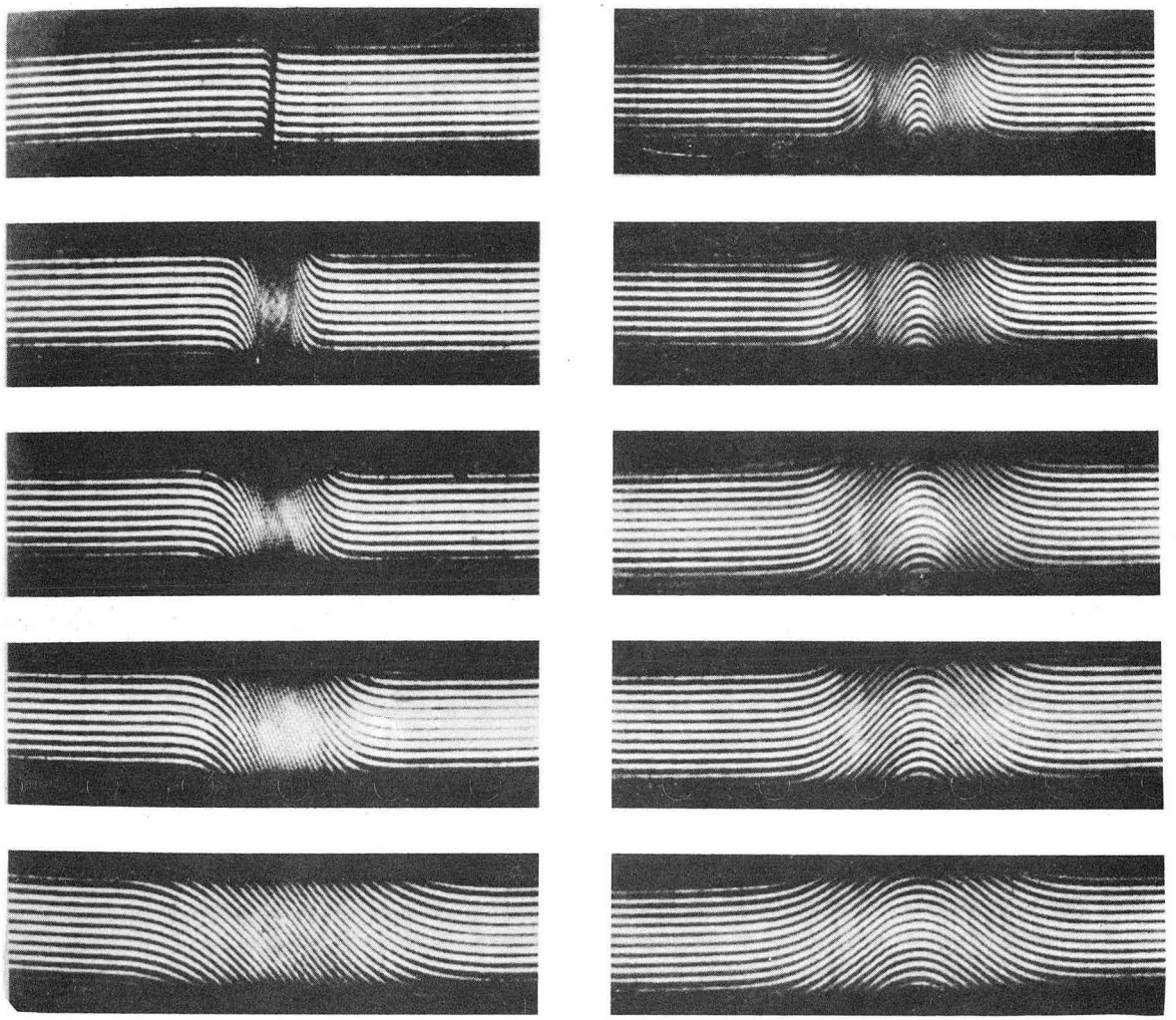

ZN-5134

Fig. 14. Left: Interference pictures obtained with the aid of the modified Rayleigh interferometer, showing the diffusion of a 0.2% solution of sucrose against water.
Right: Interference pictures obtained with the aid of the modified Rayleigh interferometer using 2 identical diffusion boundaries, slightly shifted with respect to each other, of an 0.2% sucrose solution against water in the twin cell.

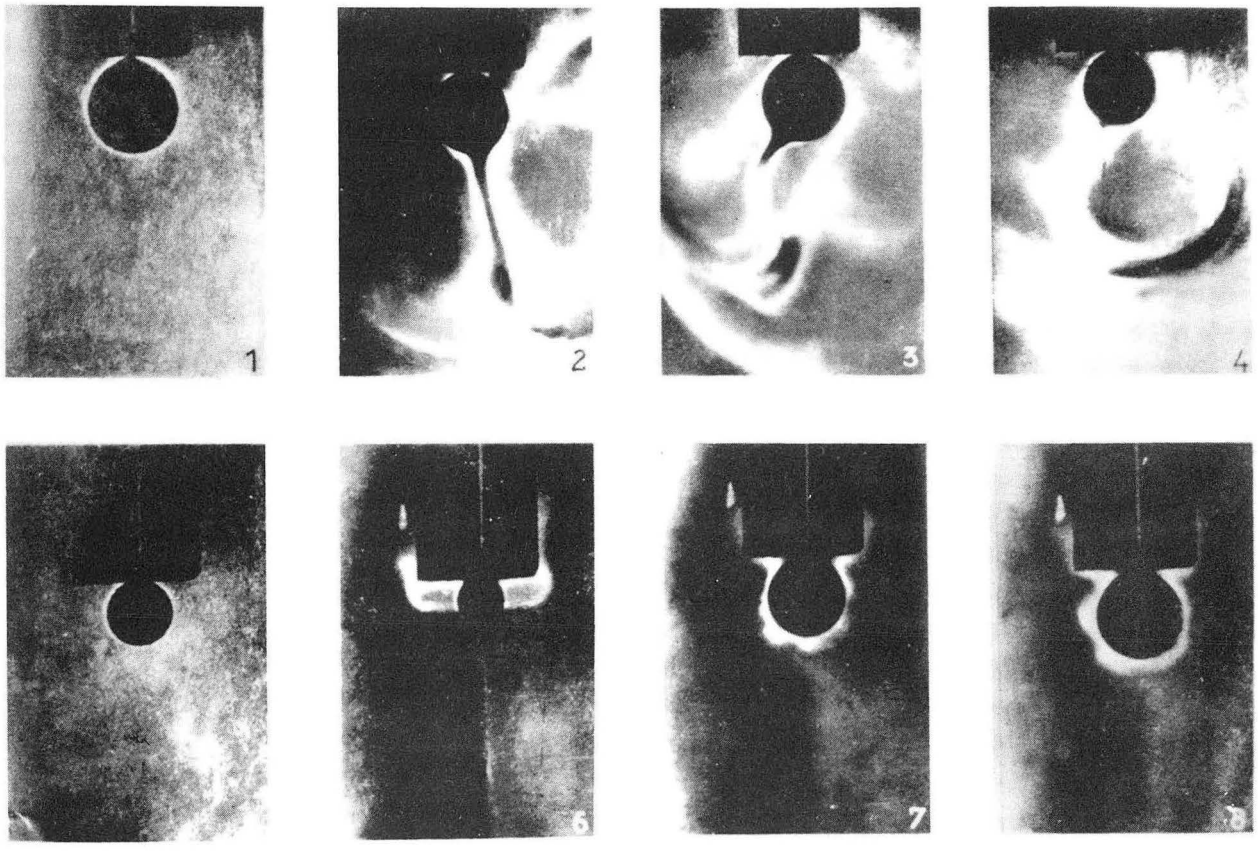

ZN-5135

Fig. 15. Strömungsbilder bei der Reduktion an der Queeksilbertrop fkathode.
Bild 1. Ungestörte Diffusionsschicht beider Reduktion einer n/50 $FeCl_3$-Lösung.
Bild 2-4. Strömungen des Elektrolyten von oben nach unten bei derselben Lösung, aber geringerem potential.
Bild 5. Ungestörte Diffusionsschicht bei der Reduktion einer n/50 $NiCl_2$-Lösung.
Bild 6. Glockenformige Strömung des Elektrolyten bei derselben Lösung aber geringerem potential.
Bild 7 and 8. Wirbelartige Strömung bei der Reduktion einer n/10 $NiCl_2$-Lösung.

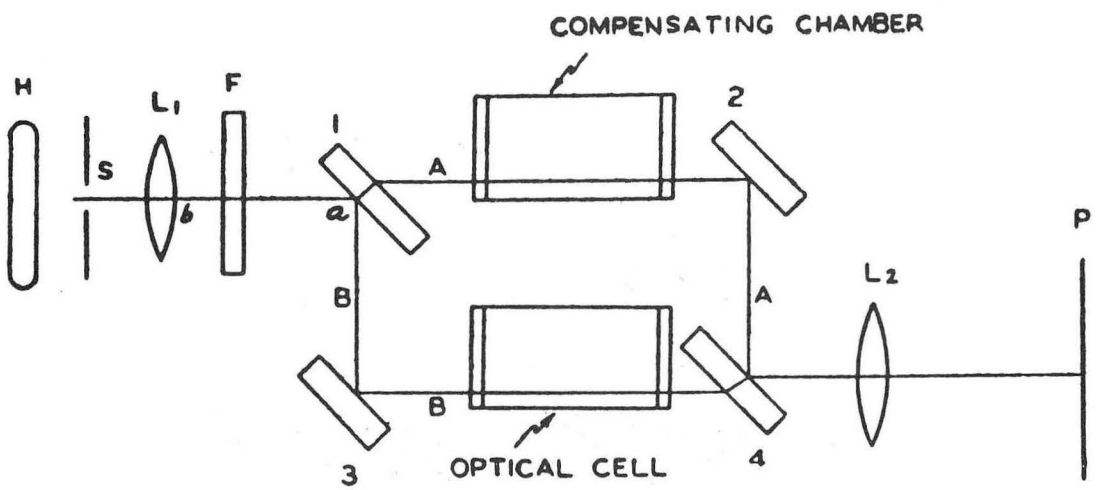

MU-35603

Fig. 16

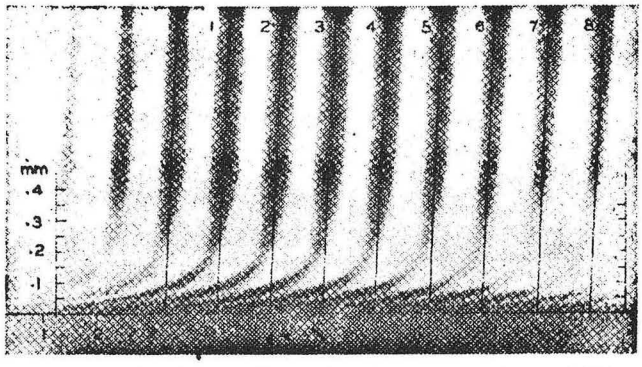

Interference Fringe Displacement at Re = 7200

Test 69

MU-35604

Fig. 17

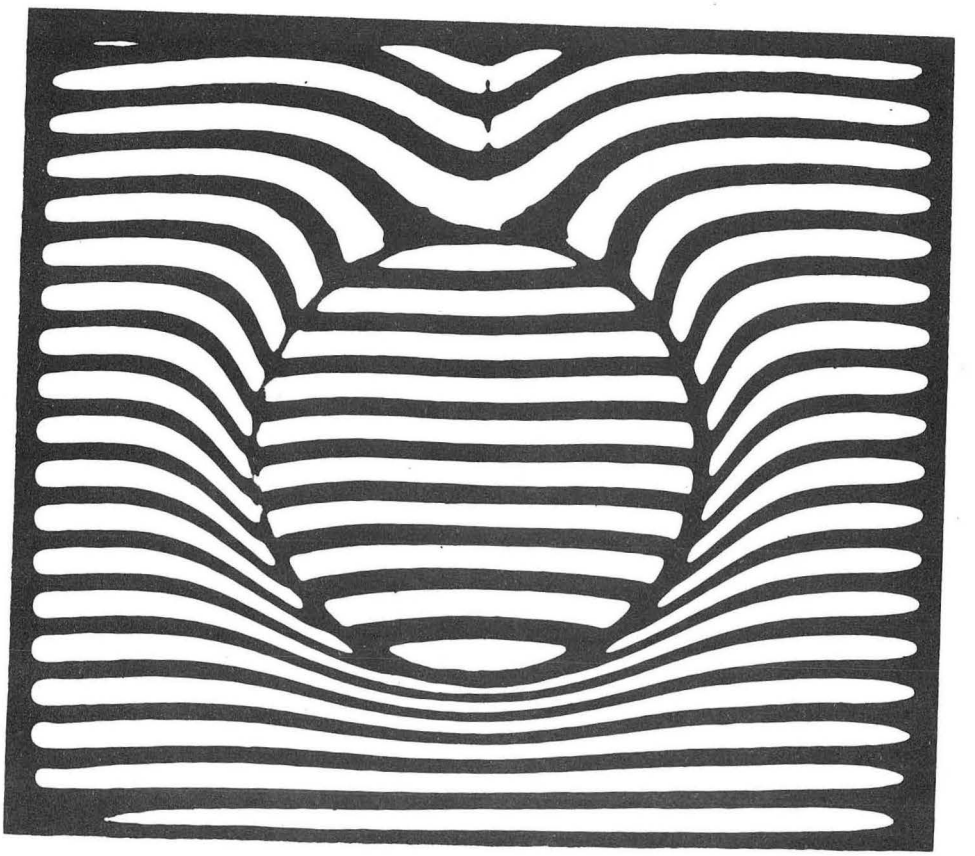

MU-35624

Fig. 18

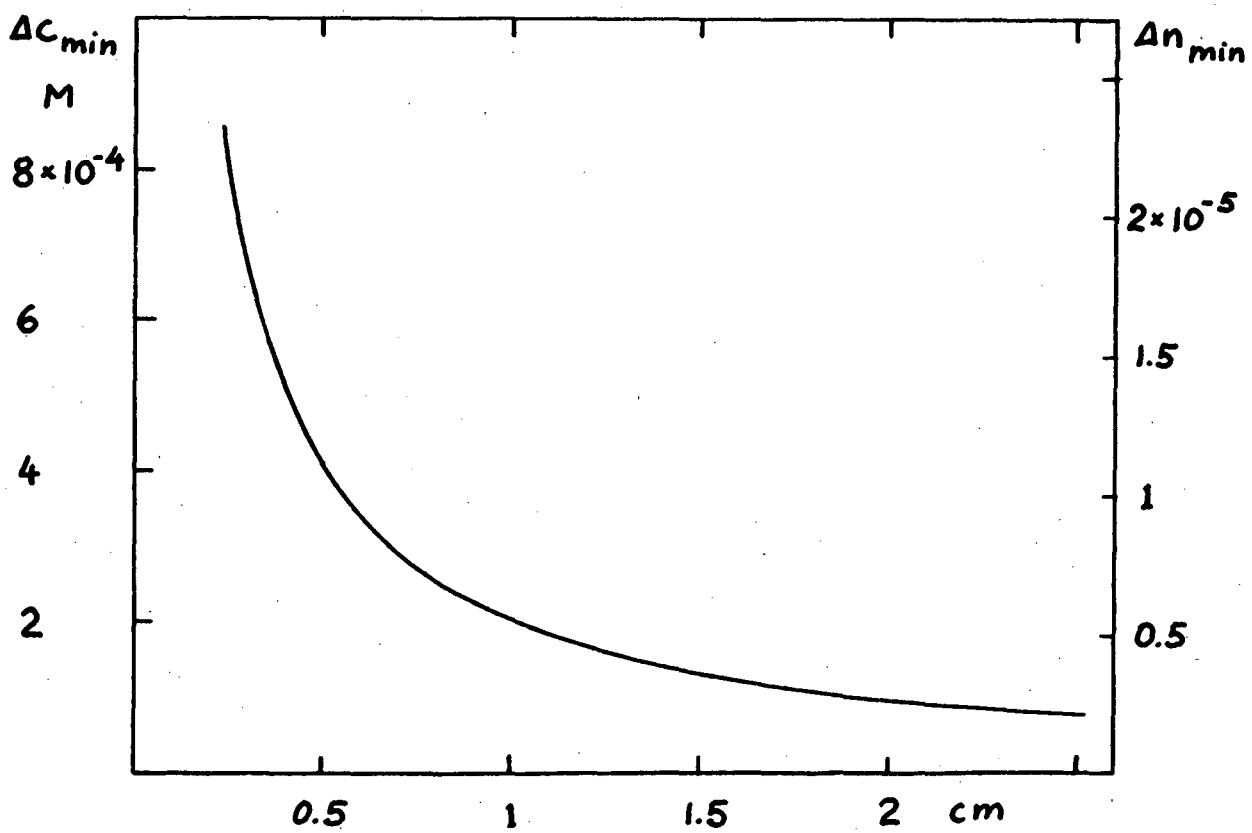

INTERFEROMETER SENSITIVITY AS A FUNCTION OF DIMENSION TRAVERSED BY THE LIGHT

MUB-6108

Fig. 19

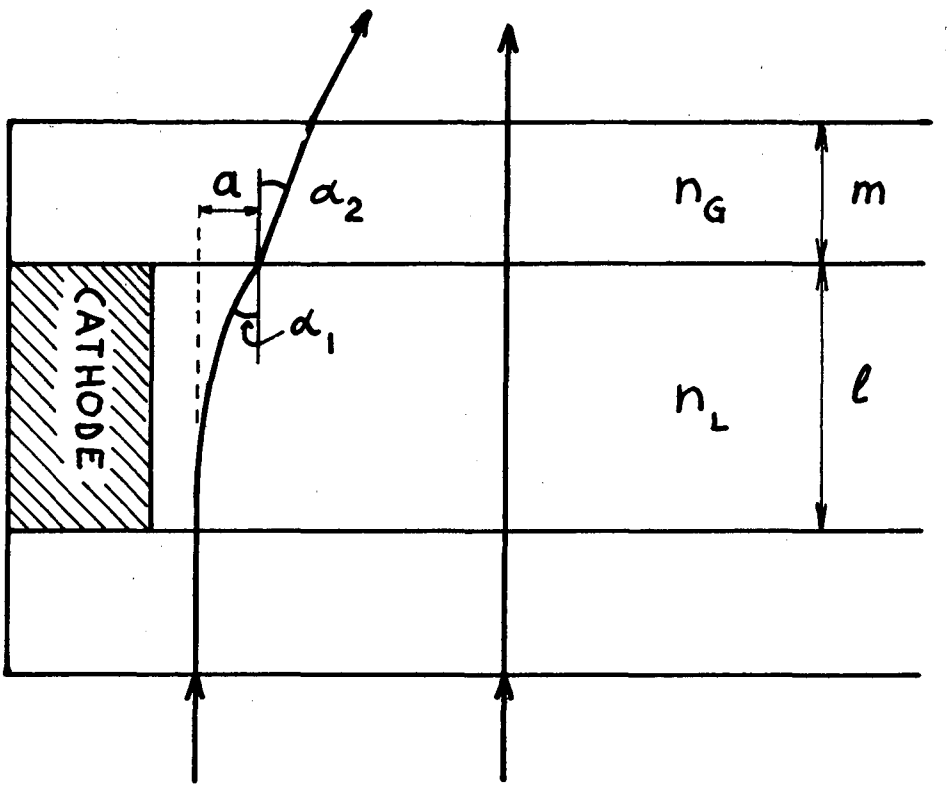

Errors Due to Light Deflection

MUB-6109

Fig. 20

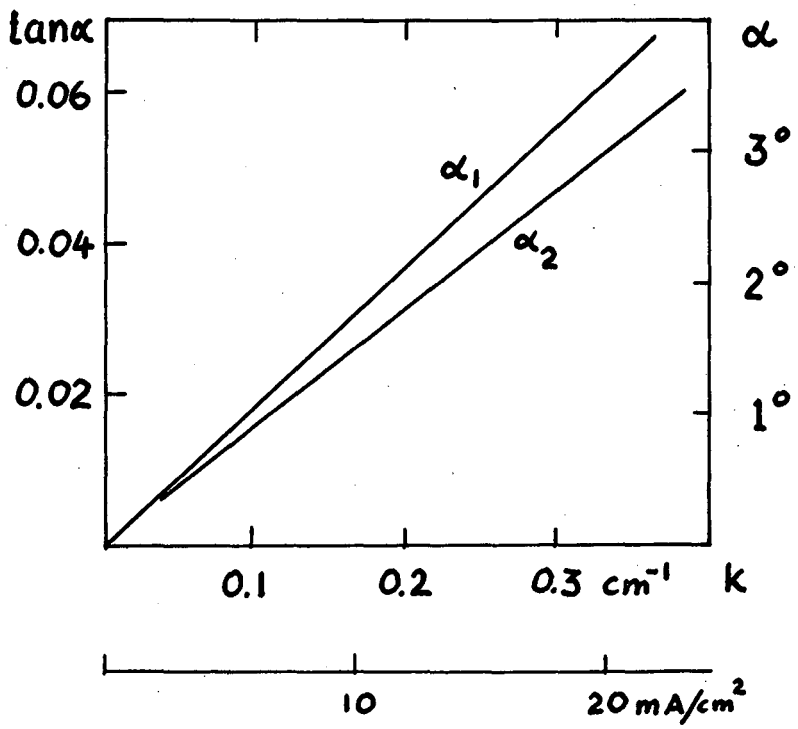

Angles of Deflection and Refraction
Cell 0.25 cm.

MUB-6110

Fig. 21

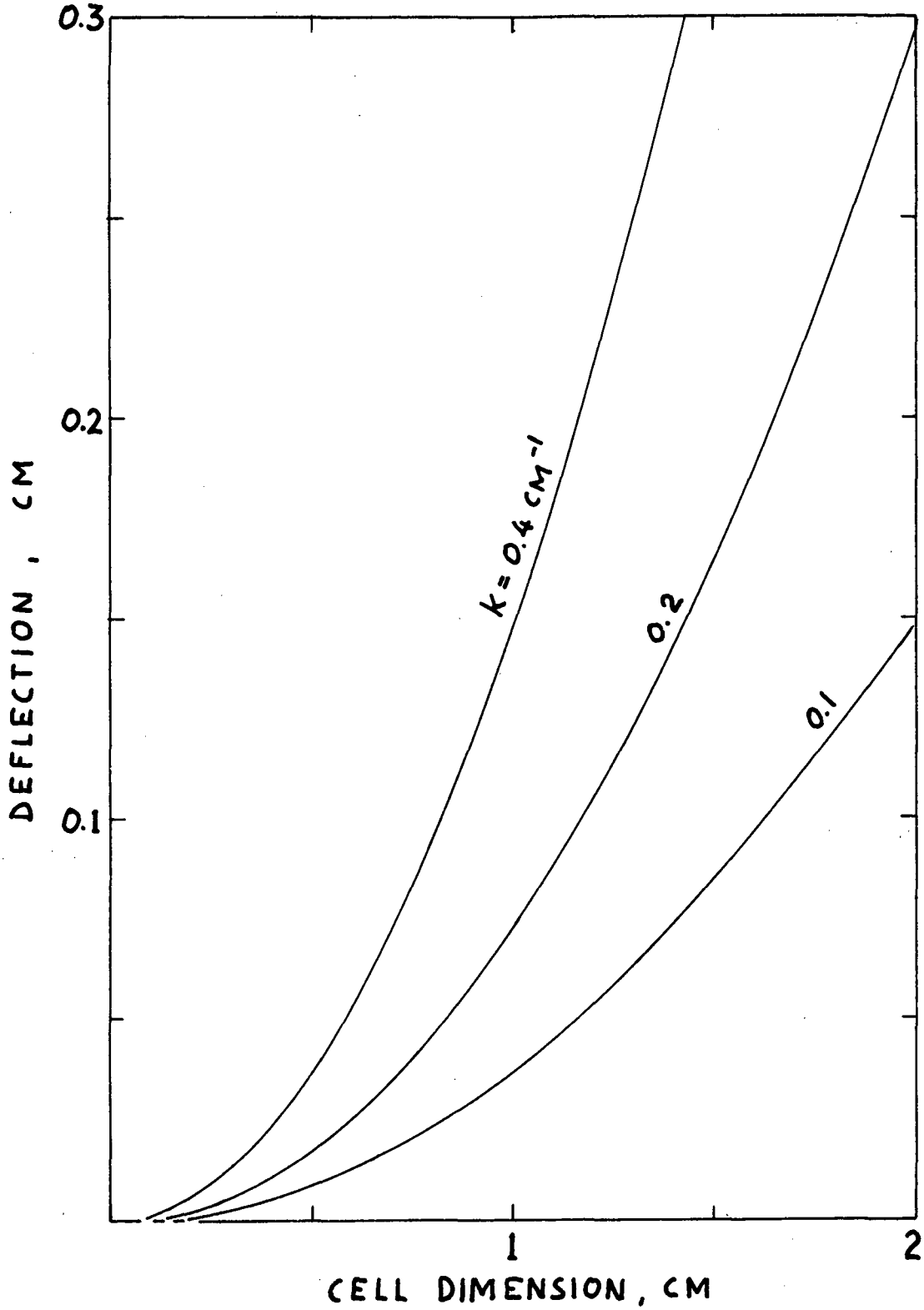

LIGHT DEFLECTION IN REFRACTIVE INDEX GRADIENTS
(6, 12, 24 mA/cm^2, $CuSO_4$)

MUB-6111

Fig. 22

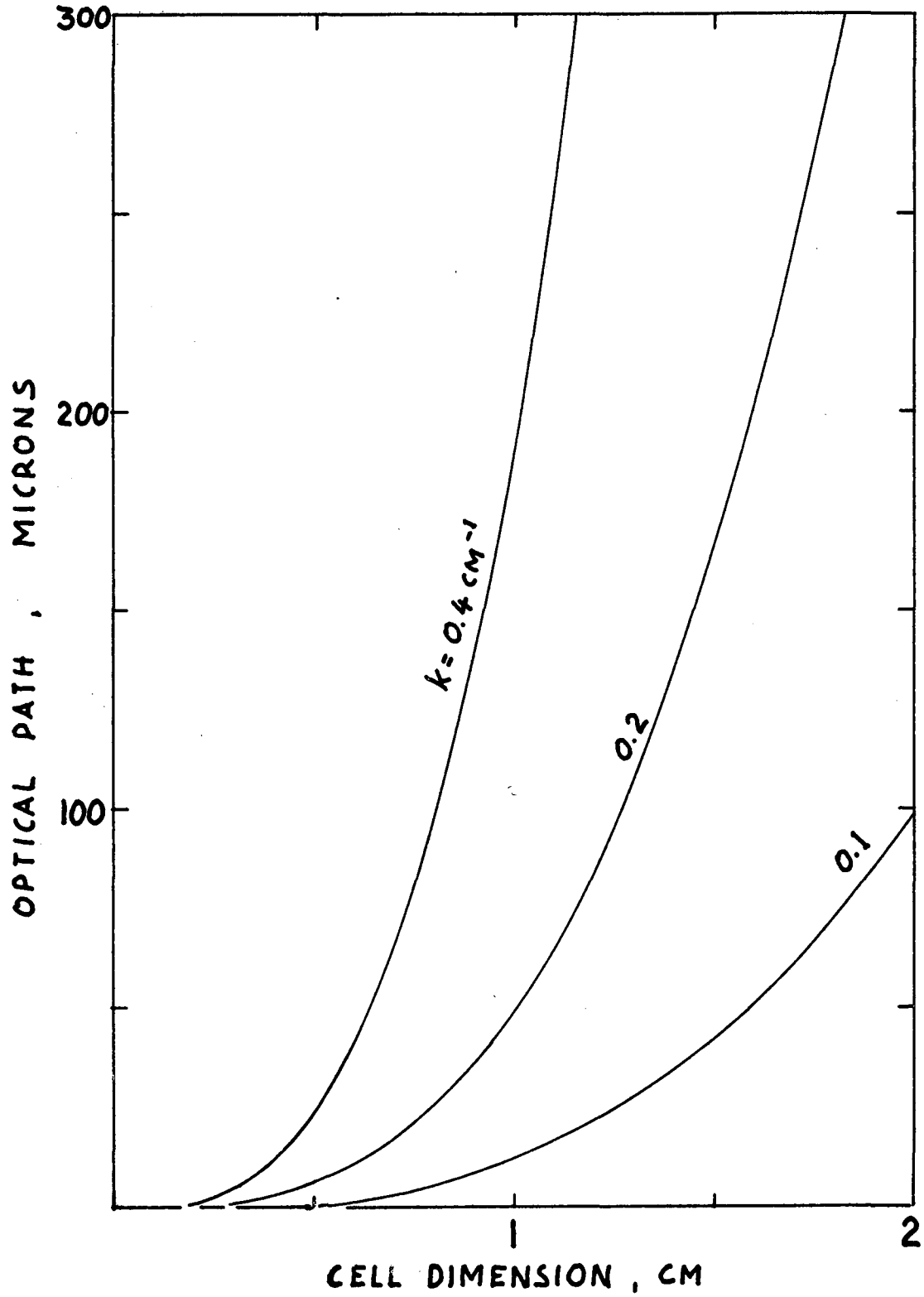

OPTICAL PATH ERROR DUE TO LIGHT DEFLECTION

MUB-6112

Fig. 23

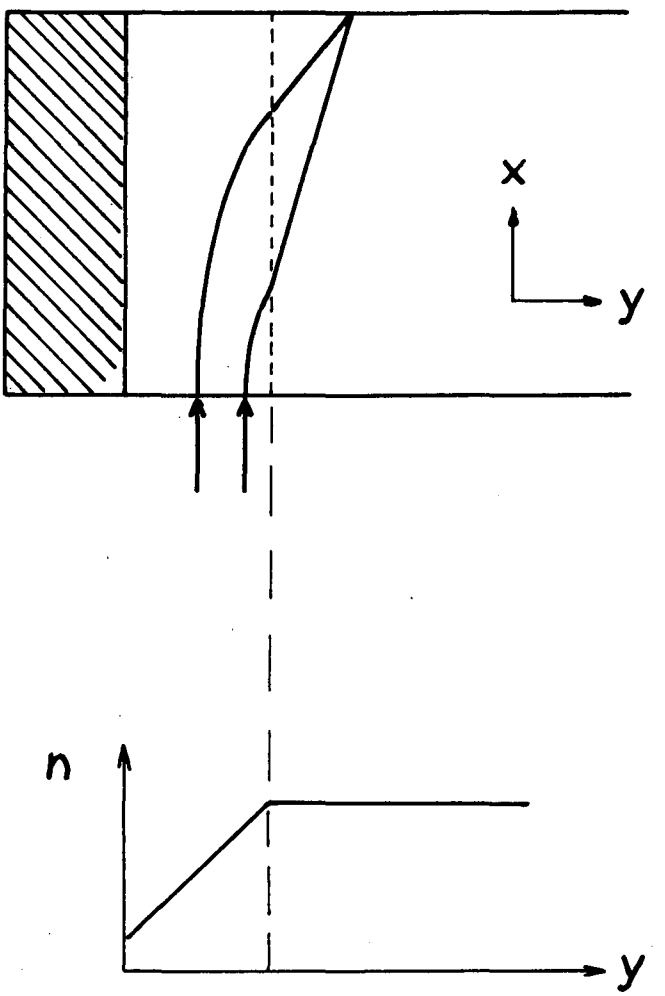

Light Deflection in Boundary Layer

MUB-6113

Fig. 24

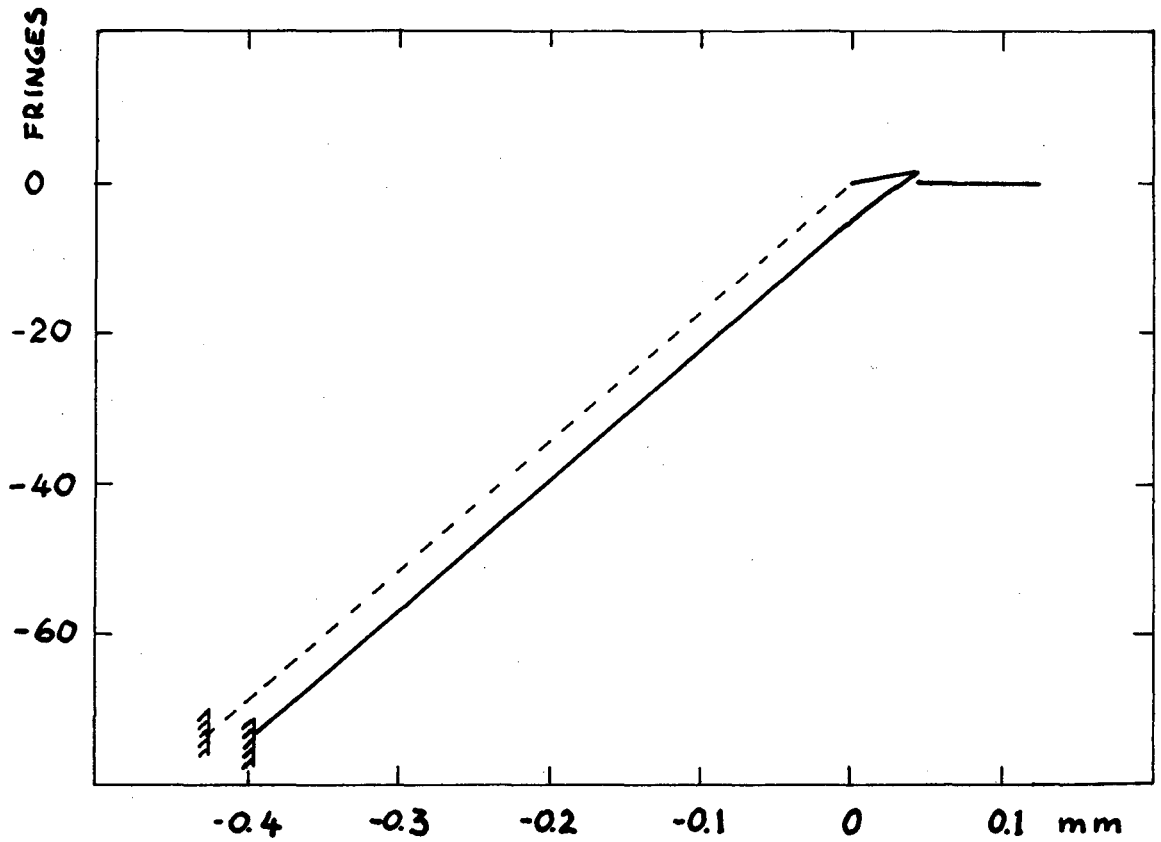

Fringe Pattern with Light Deflection
$K = 0.37\ cm^{-1}$; $\ell = 0.25$ cm

MUB-6114

Fig. 25

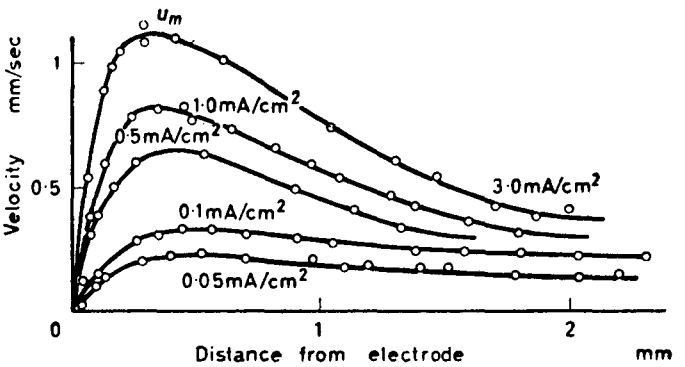

MU-35605

Fig. 26

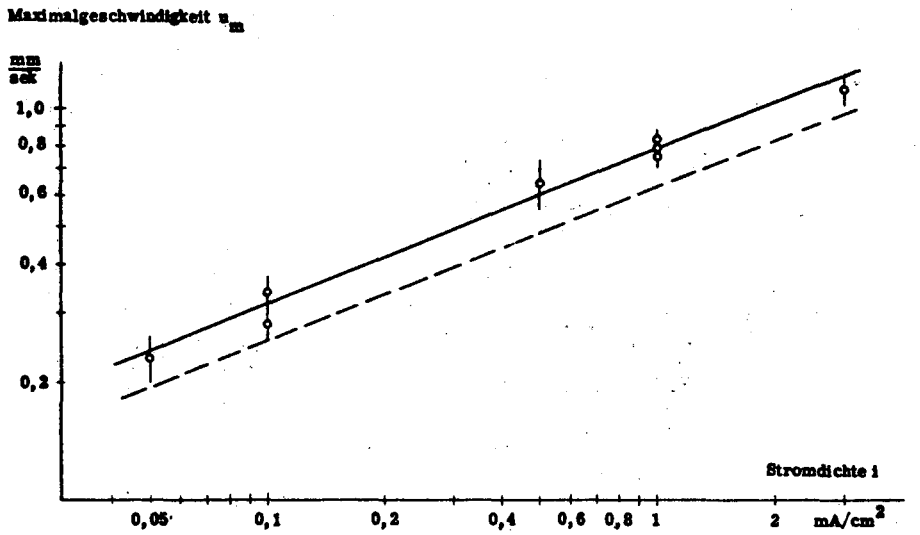

MU-35606

Fig. 27

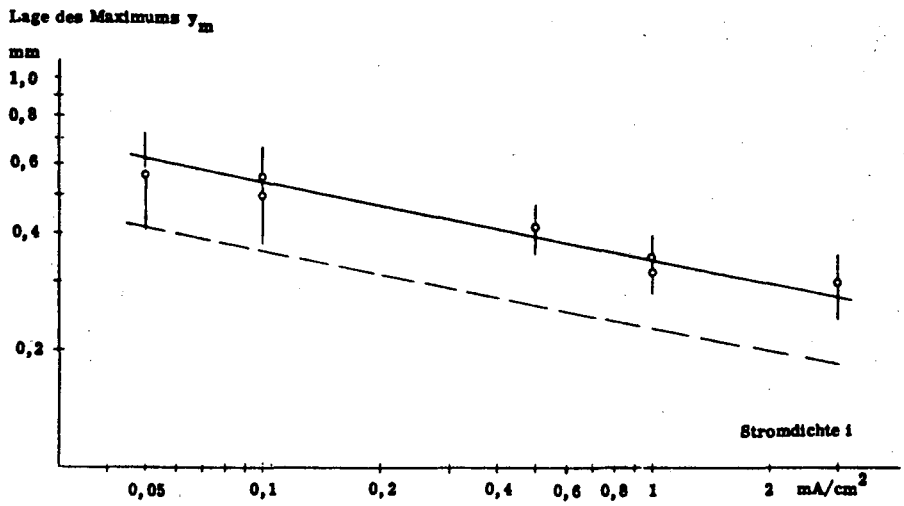

MU-35607

Fig. 28

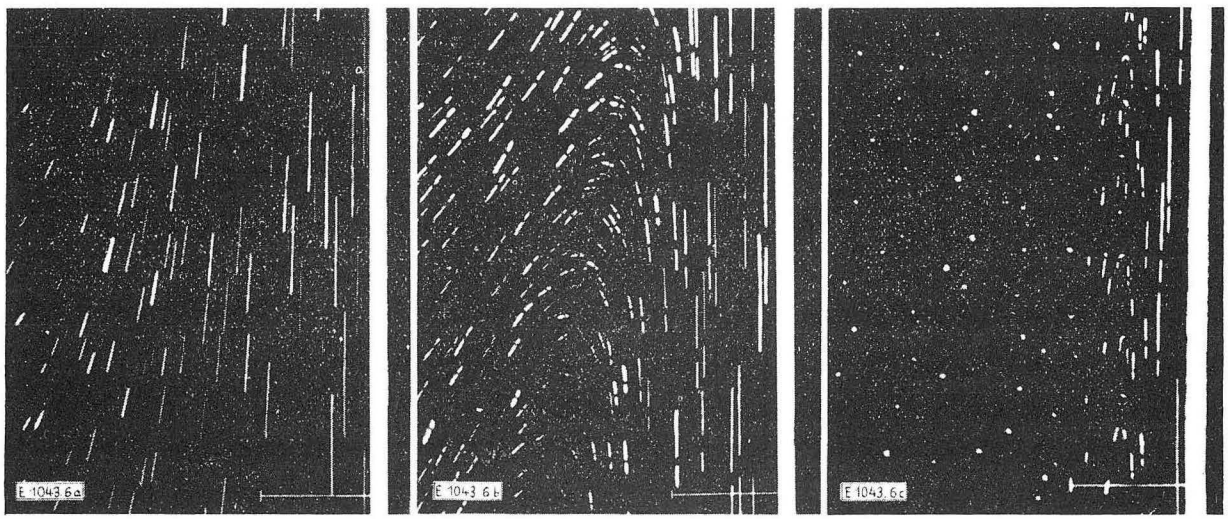

MU-35608

Fig. 29

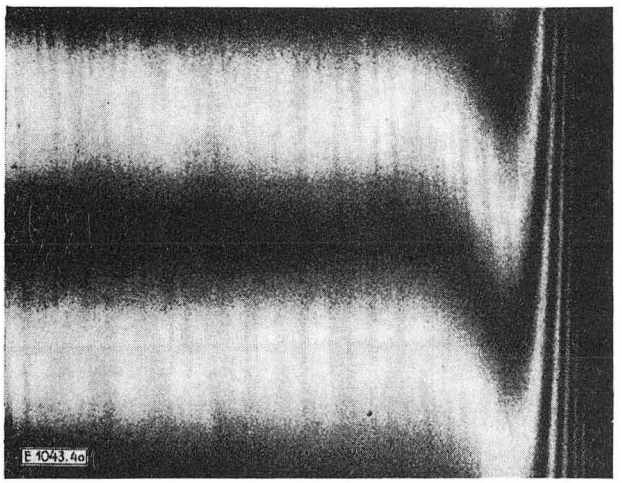

9,6 mA/cm²

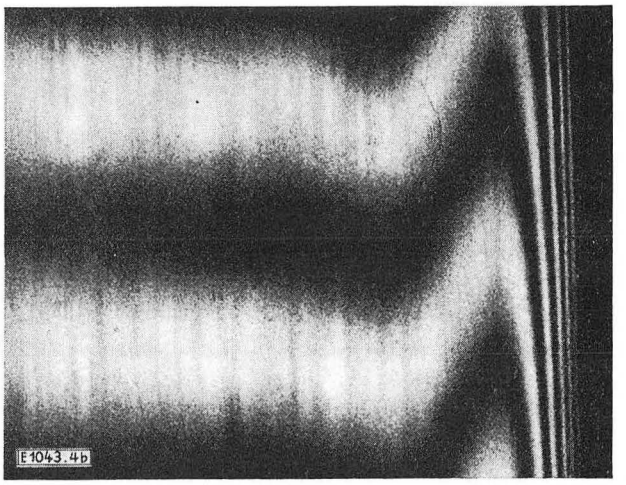

$CuSO_4$ 0,1 m

MU-35609

Fig. 30

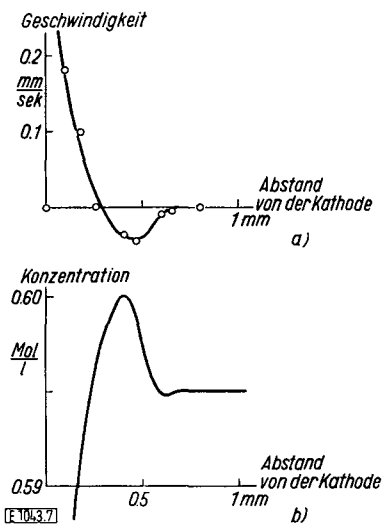

a) Geschwindigkeitsverteilung, b) Konzentrationsverteilung 5 mA/cm² $CuSO_4$ 0,6 m gemessen in 22 mm Höhe über dem unteren Kathodenrand nach 15 Minuten

MU-35610

Fig. 31

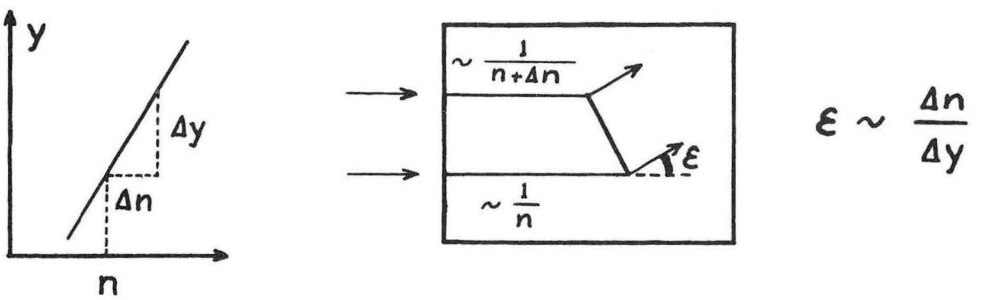

Light Deflection by Refractive Index Gradient

MU-35611

Fig. 32

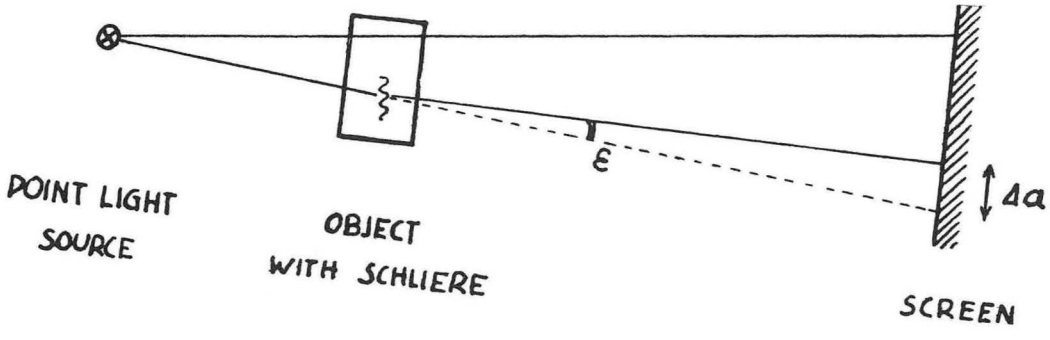

Schlieren - Shadowgraph System

MU-35612

Fig. 33

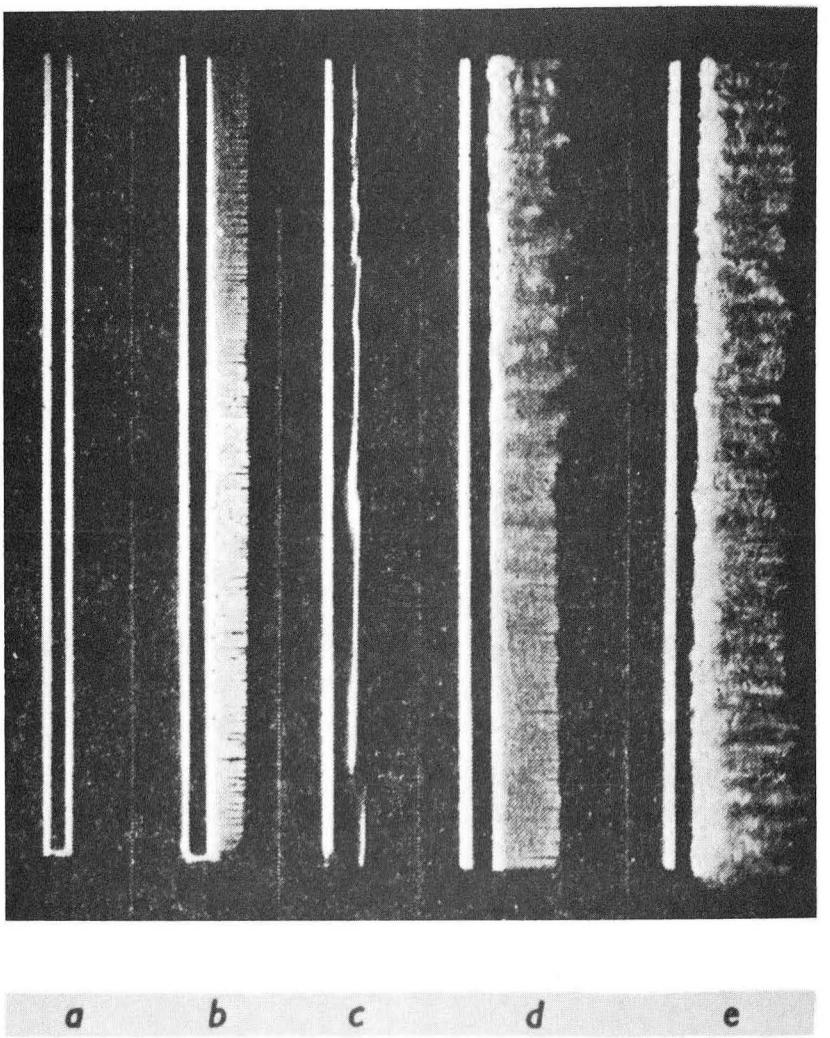

ZN-5136

Fig. 34. a) Current shut off; b) Cathode from 2 A/dm^2 on right side; c) Anode with 2 A/dm^2 on right side; d) Transition from laminar to turbulent flow at 1.5 A/dm^2; e) Fully developed turbulence at 4 A/dm^2. With a), b), and c) slit 2 was 2 mm wide and a = 25 mm, b = 7 mm. With d) and e) slit was 3 mm wide and a = 45 mm, b = 10 mm. In exps. d) and e), the total cathode height was 180 mm, but only the height between 80 and 140 mm from the lower end of the cathode was photographed.

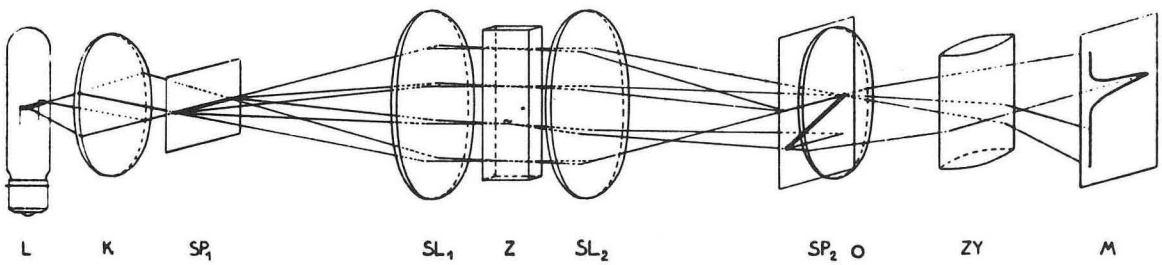

MU-35613

Fig. 35

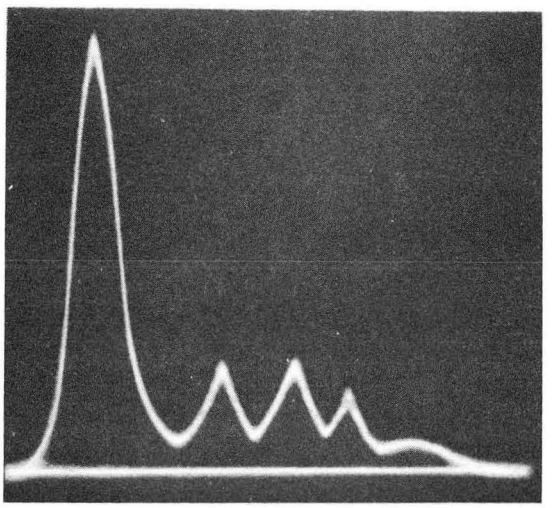

(a)

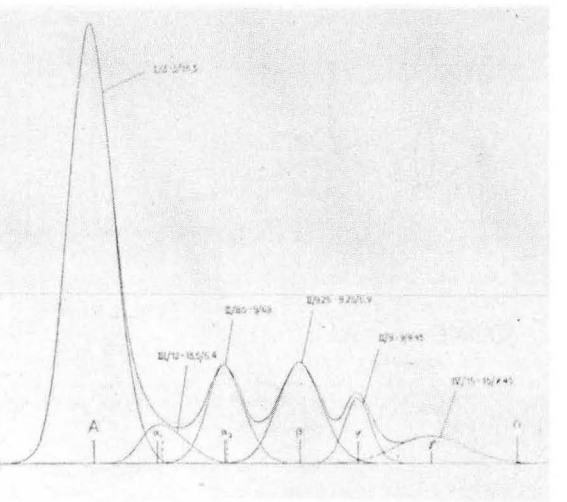

(b)

ZN-5137

Fig. 36

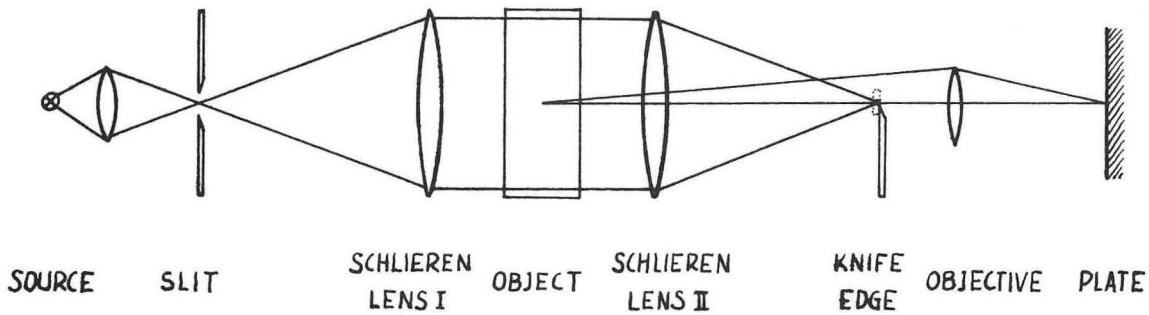

Toepler Schlieren System

MU-35614

Fig. 37

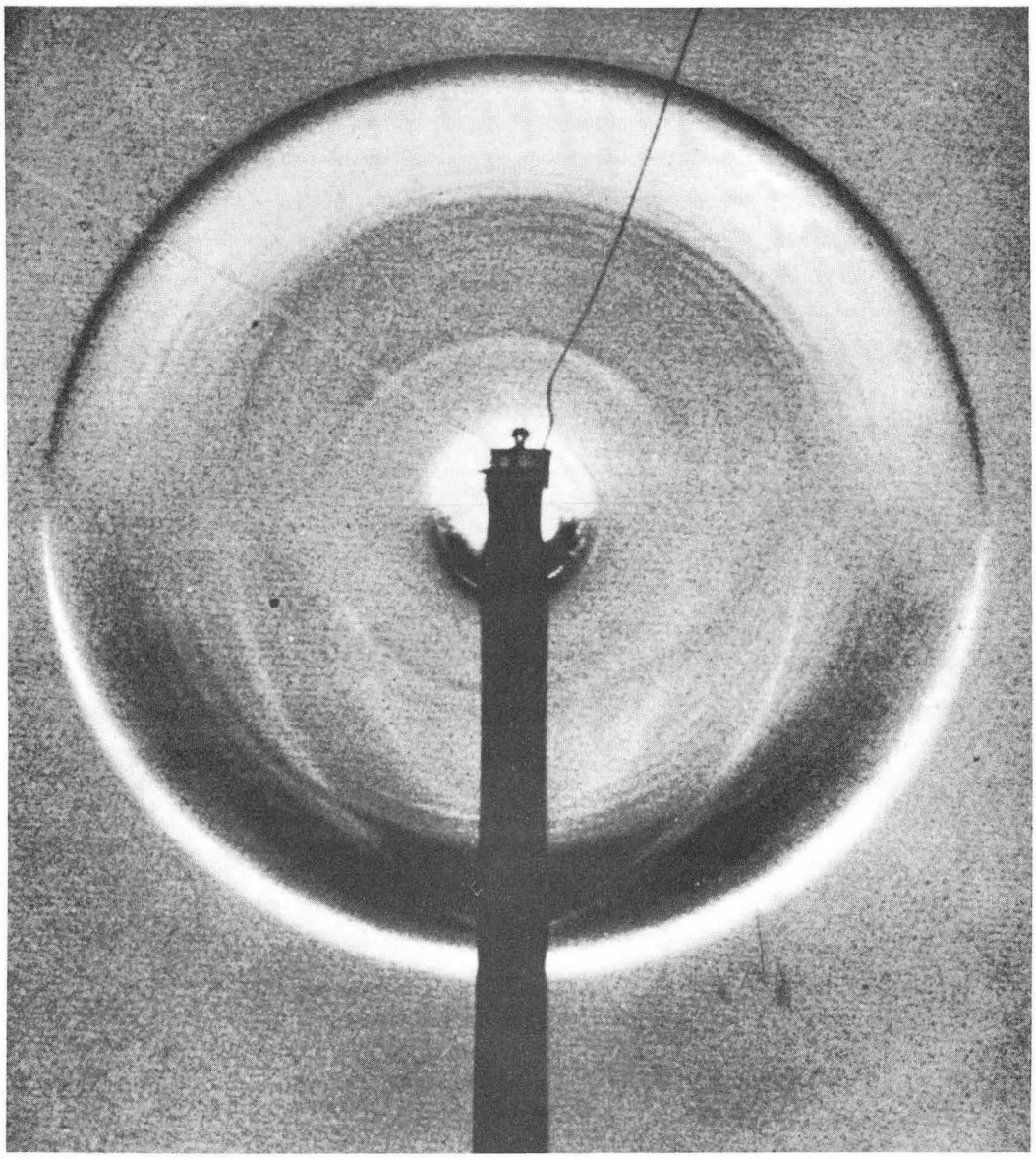

ZN-5138

Fig. 38

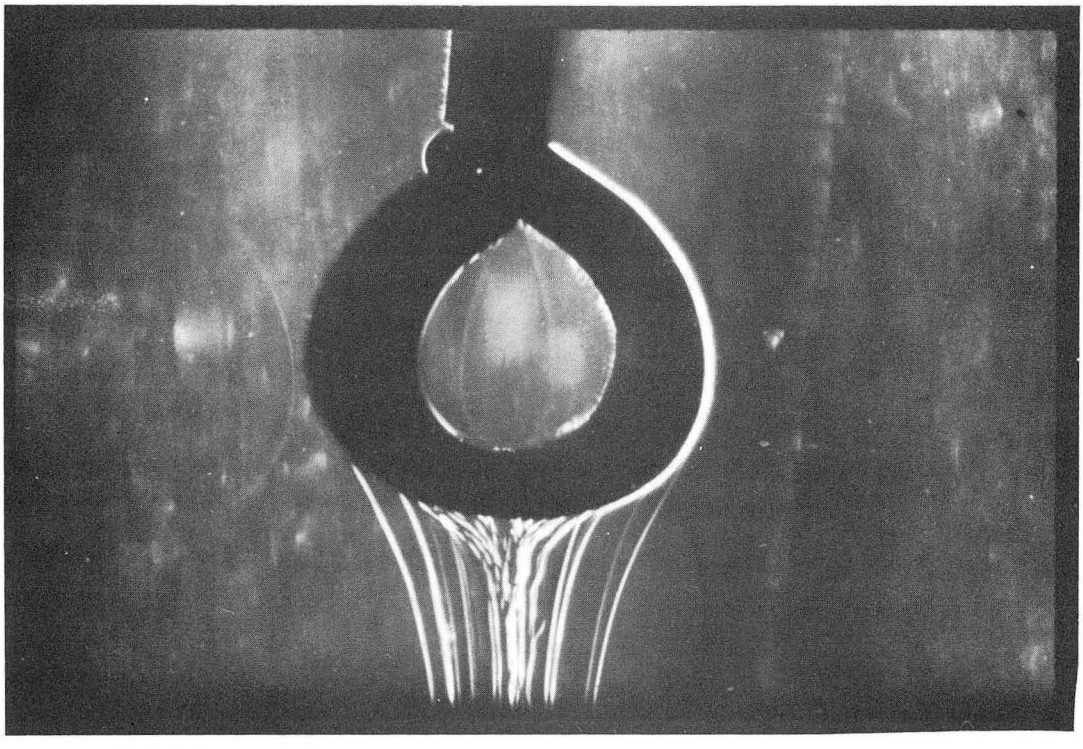

ZN-5139

Fig. 39

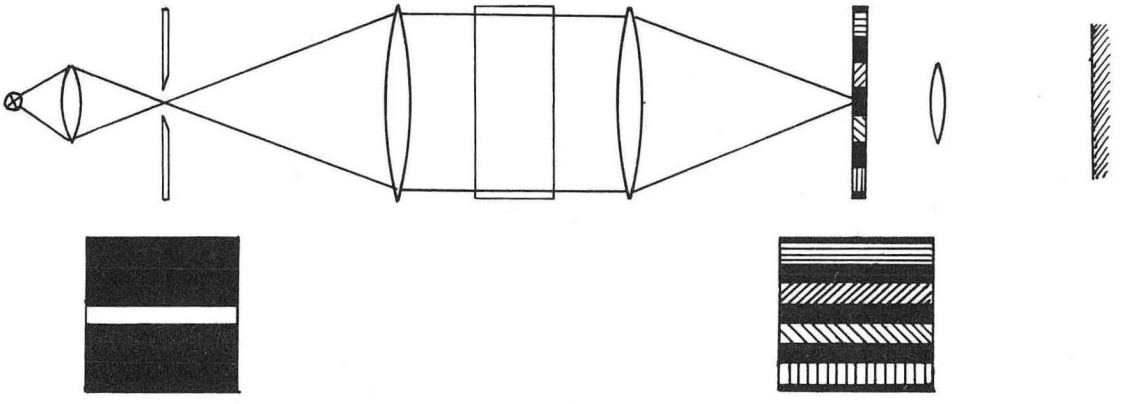

COLOR SCHLIEREN METHOD FOR DIFFERENTIATION BETWEEN
INCREMENTS OF LIGHT DEFLECTION IN ONE DIRECTION

MUB-6115

Fig. 40

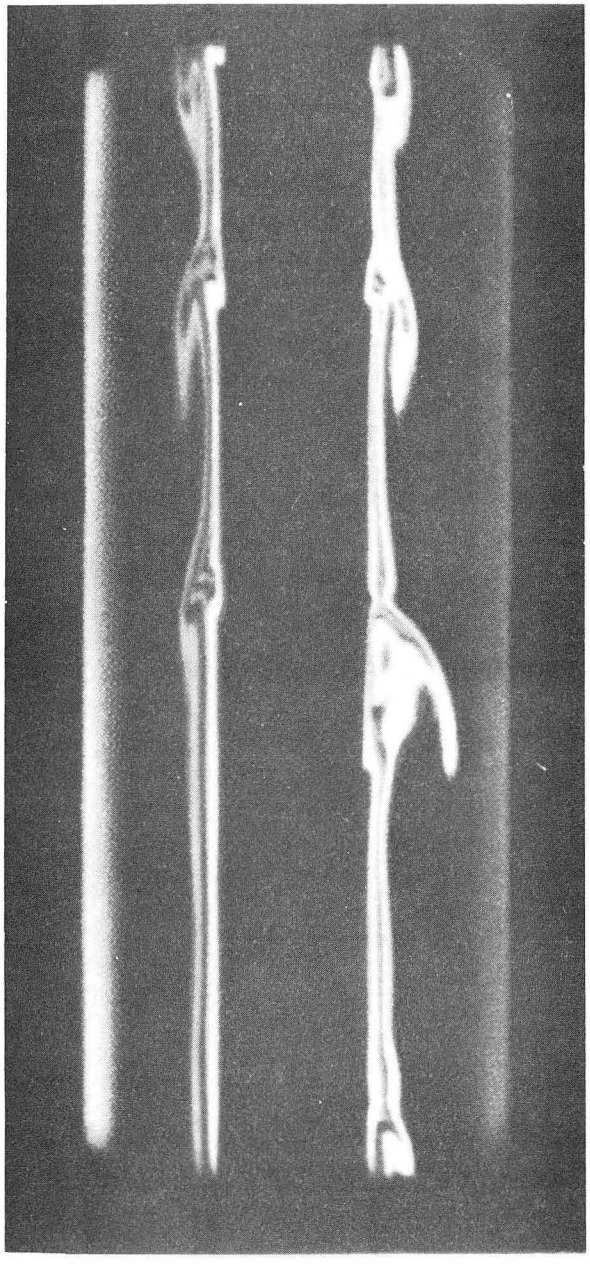

ZN-5140

Fig. 41

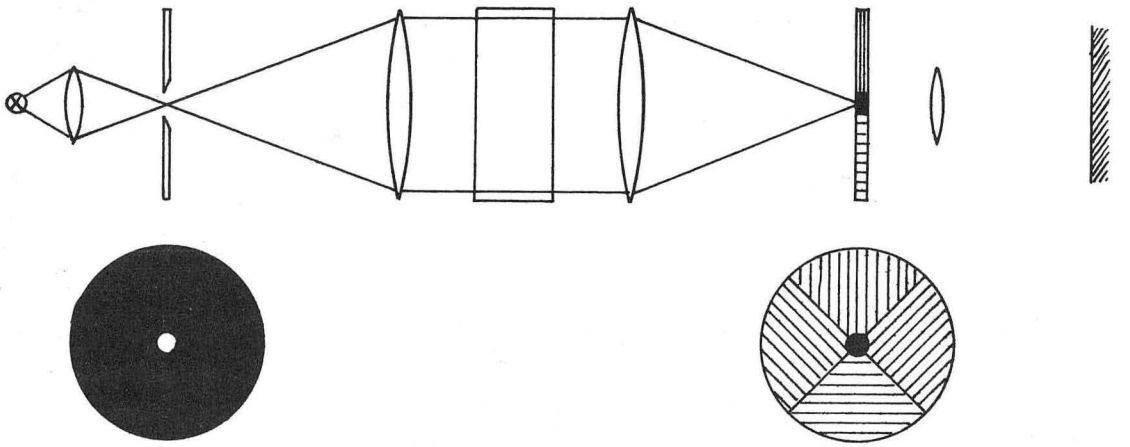

Color Schlieren Method

For differentiation between directions of light deflection

MUB-6116

Fig. 42

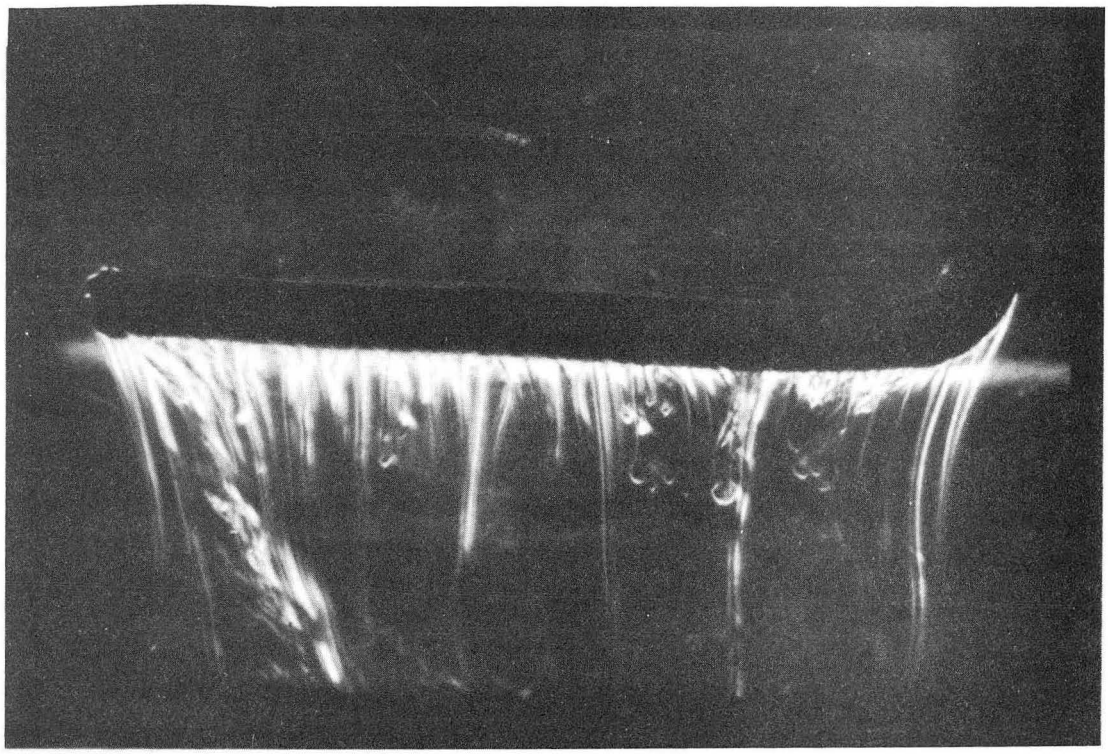

ZN-5141

Fig. 43

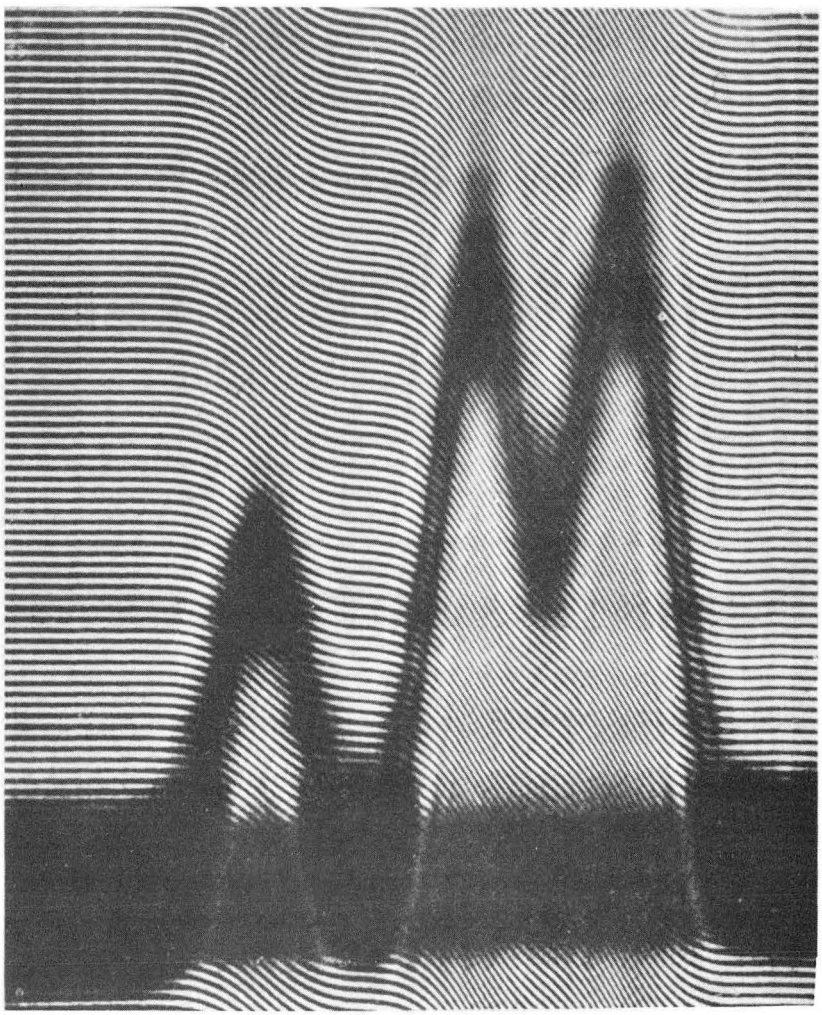

ZN-5142

Fig. 44

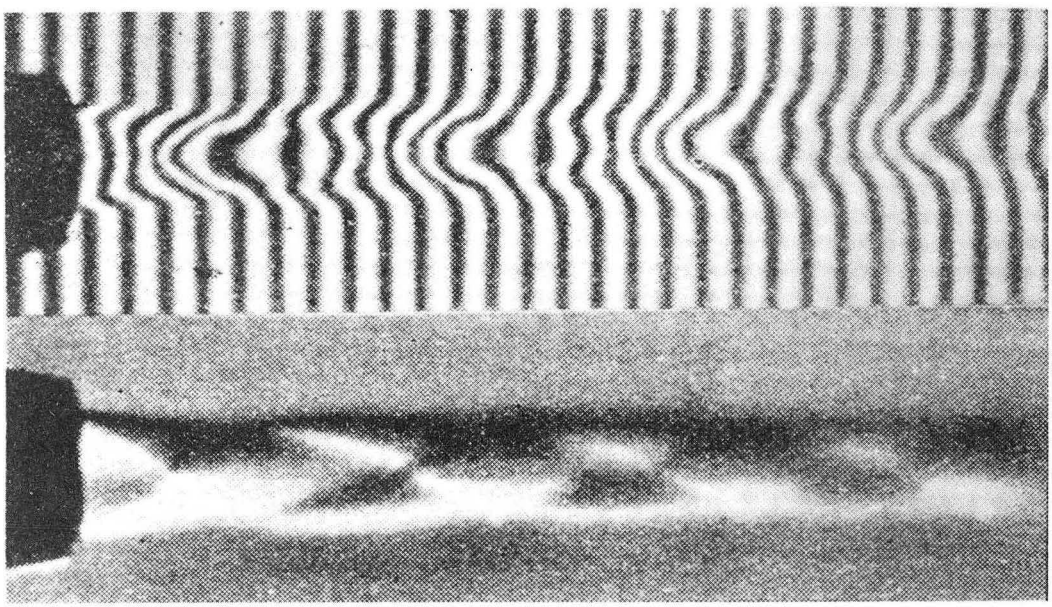

ZN-5143

Fig. 45

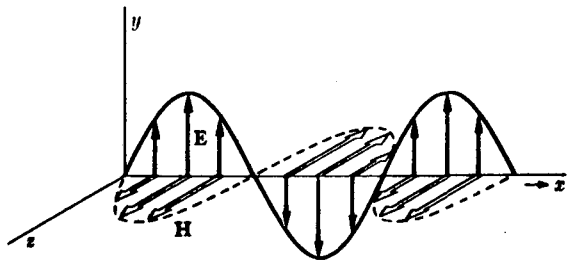

MU-35615

Fig. 46

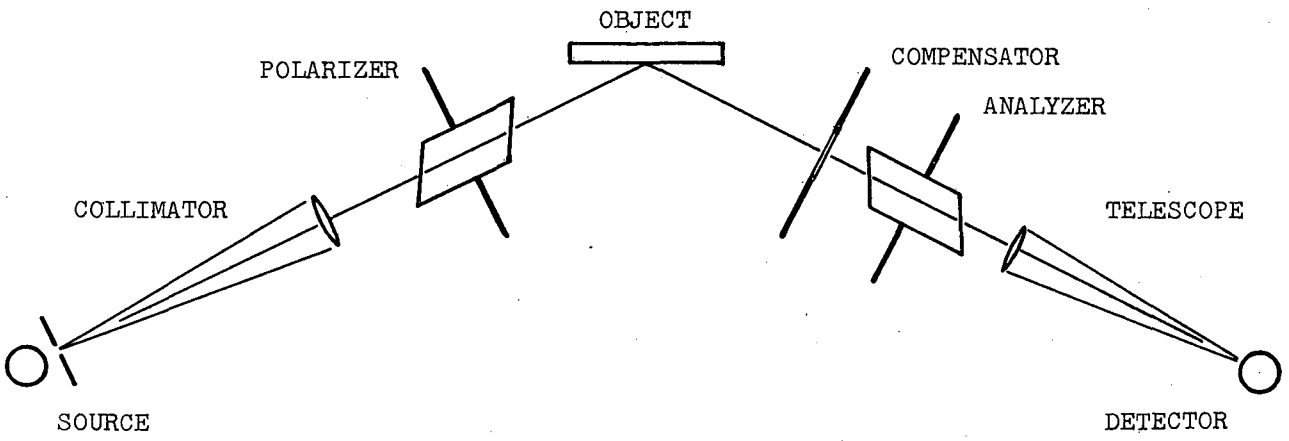

ELLIPSOMETER

MUB-6117

Fig. 47

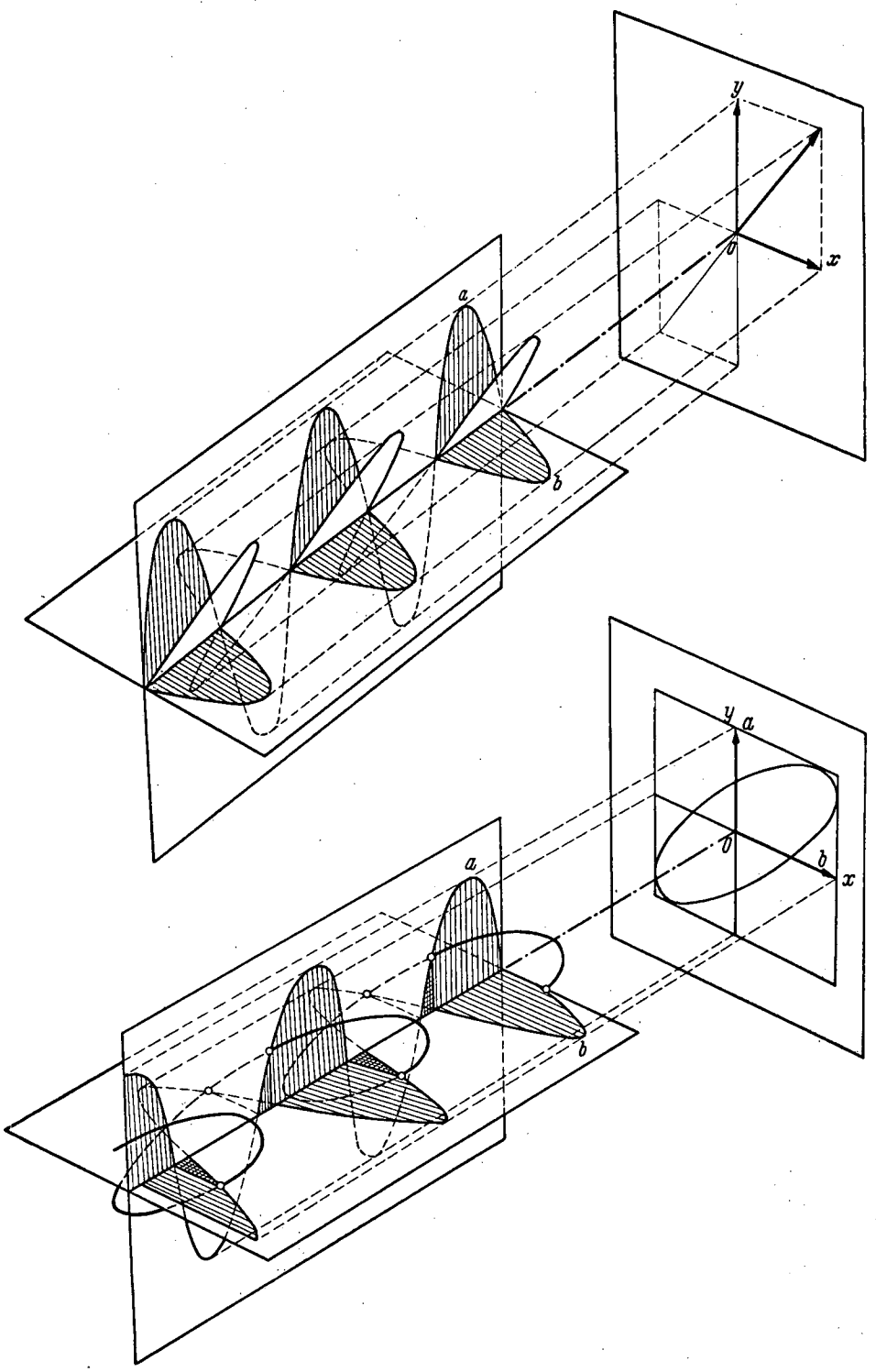

MUB-6118

Fig. 48

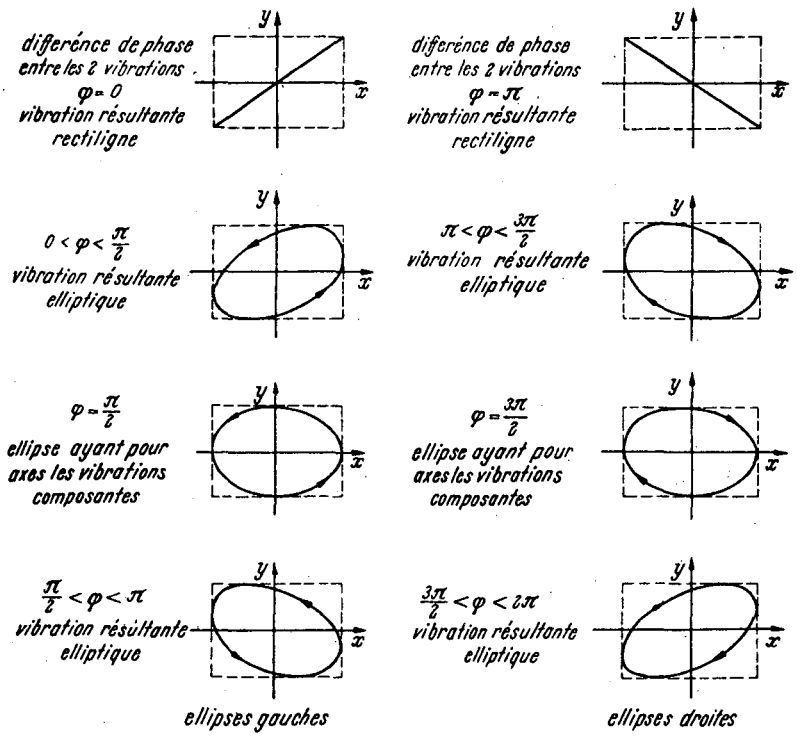

MUB-6119

Fig. 49

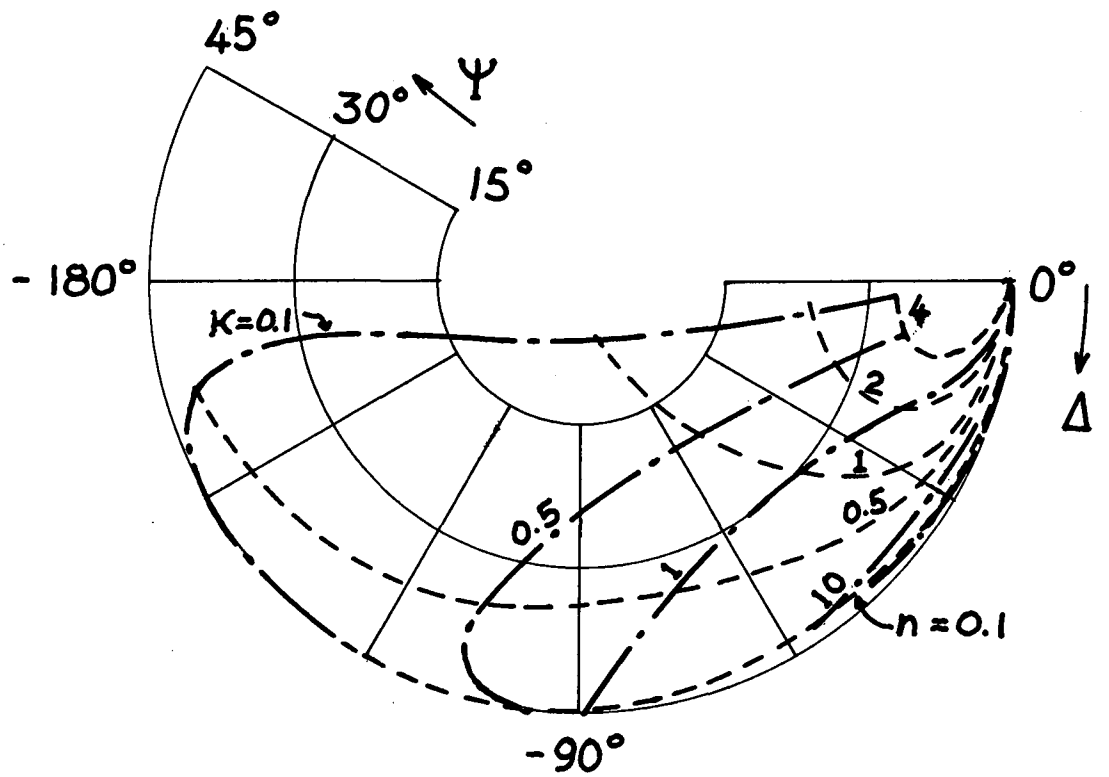

MUB-6120

Fig. 50

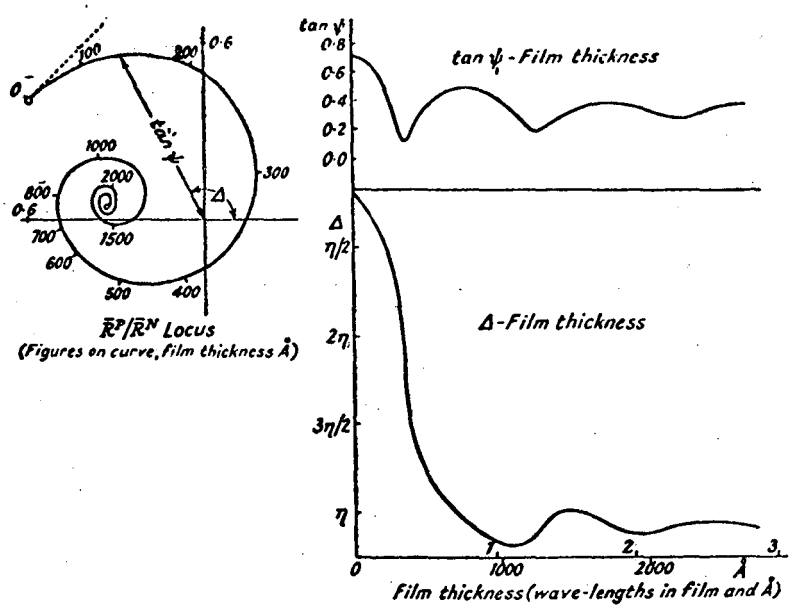

FIG. 140.—Reflection of Polarized Light at Metal Surface covered with Absorbing Film. Calculations assume incidence at $\pi/3$ and constants corresponding to Fe (Base) and Fe_2O_3 (Film) for $\Lambda_0 = 5461$ Å.

MUB-6121

Fig. 51

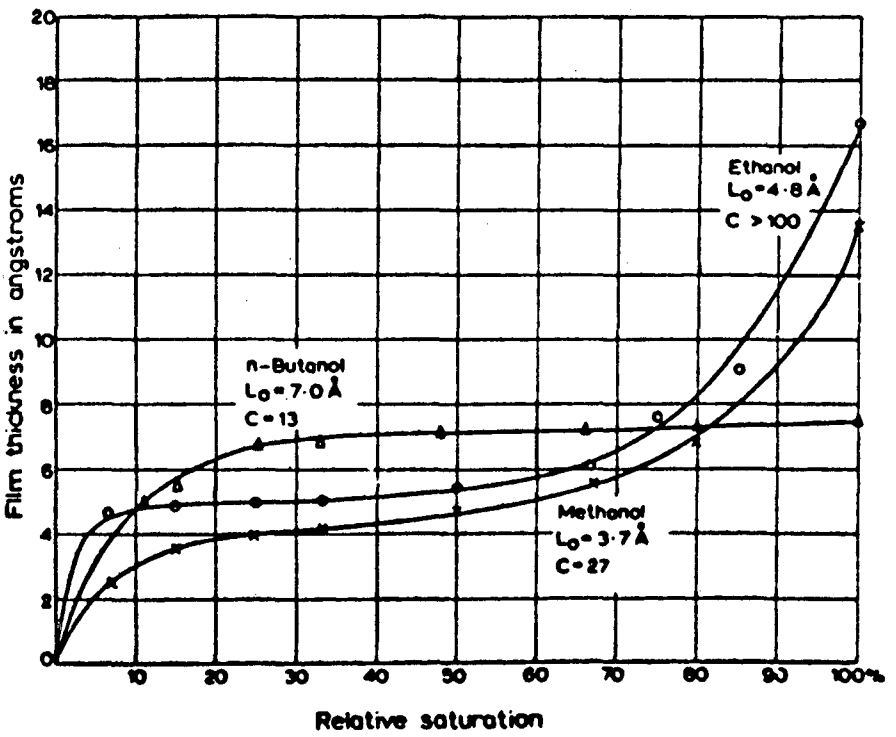

MU-35616

Fig. 52

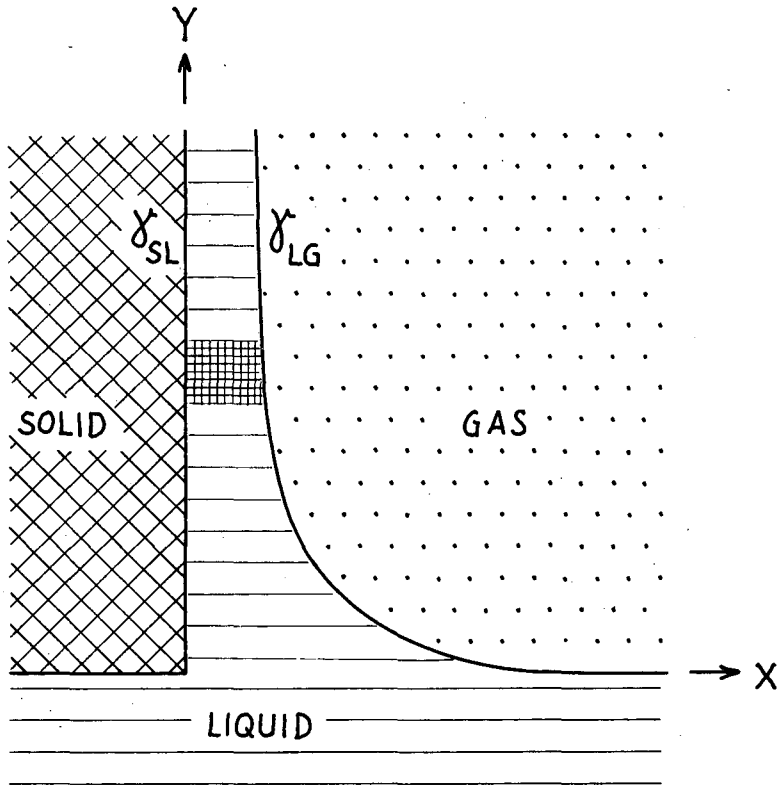

MU-35617

Fig. 53

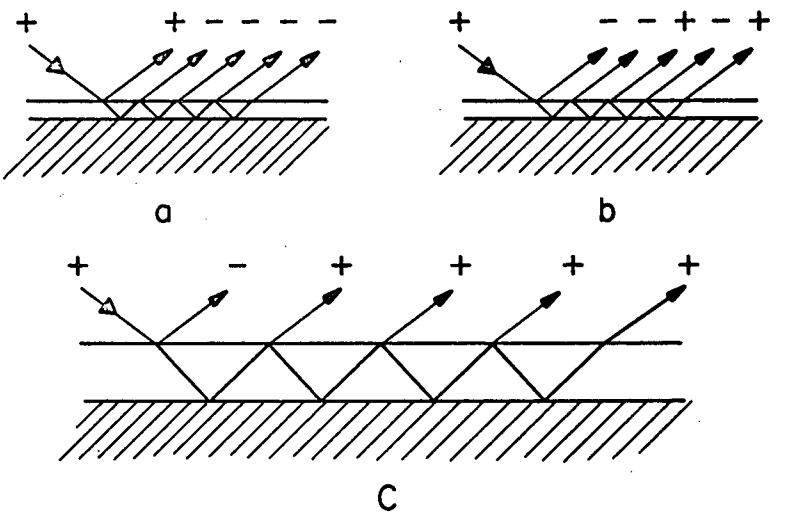

PHASE RELATIONSHIP OF INCIDENT AND REFLECTED LIGHT

(a) For destructive interference with vanishing film thickness
(b) For constructive interference with vanishing film thickness
(c) For destructive interference with $\lambda/2$ path in the film

MUB-6122

Fig. 54

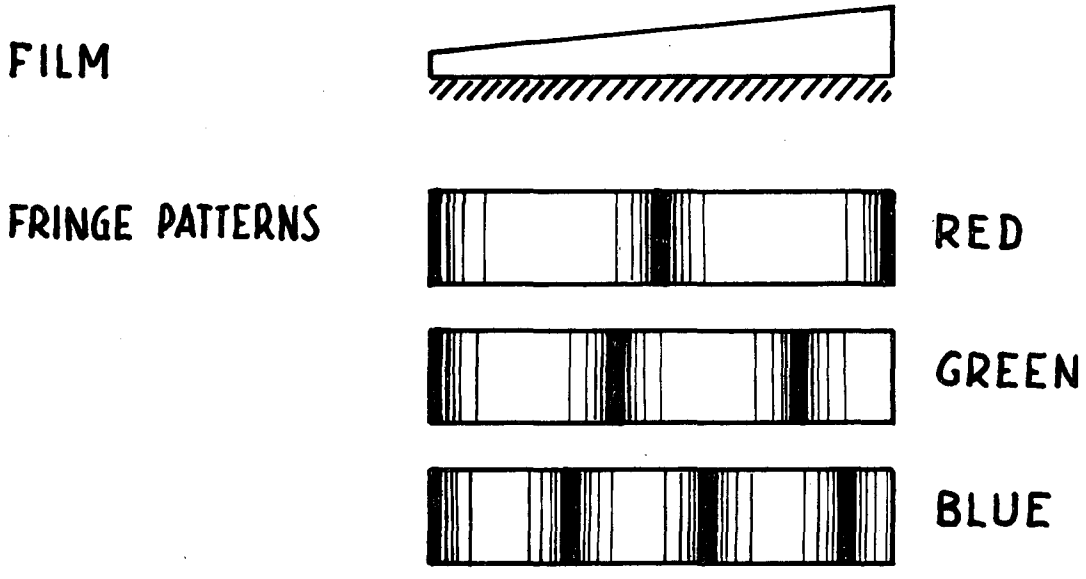

Fig. 55

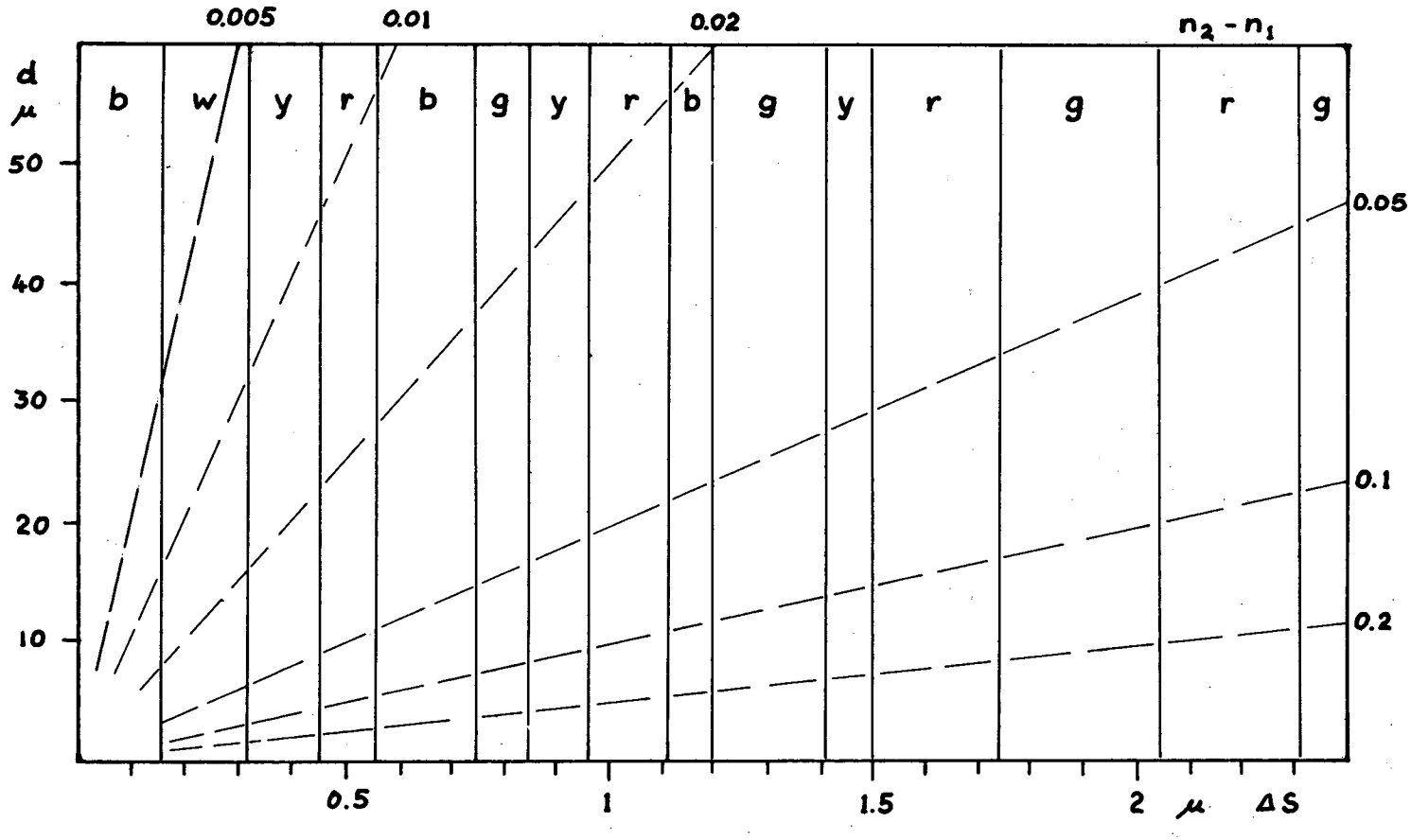

MICHEL-LEVY SCALE OF INTERFERENCE COLORS

b = blue, w = white, y = yellow, r = red, g = green

MUB-6123

Fig. 56

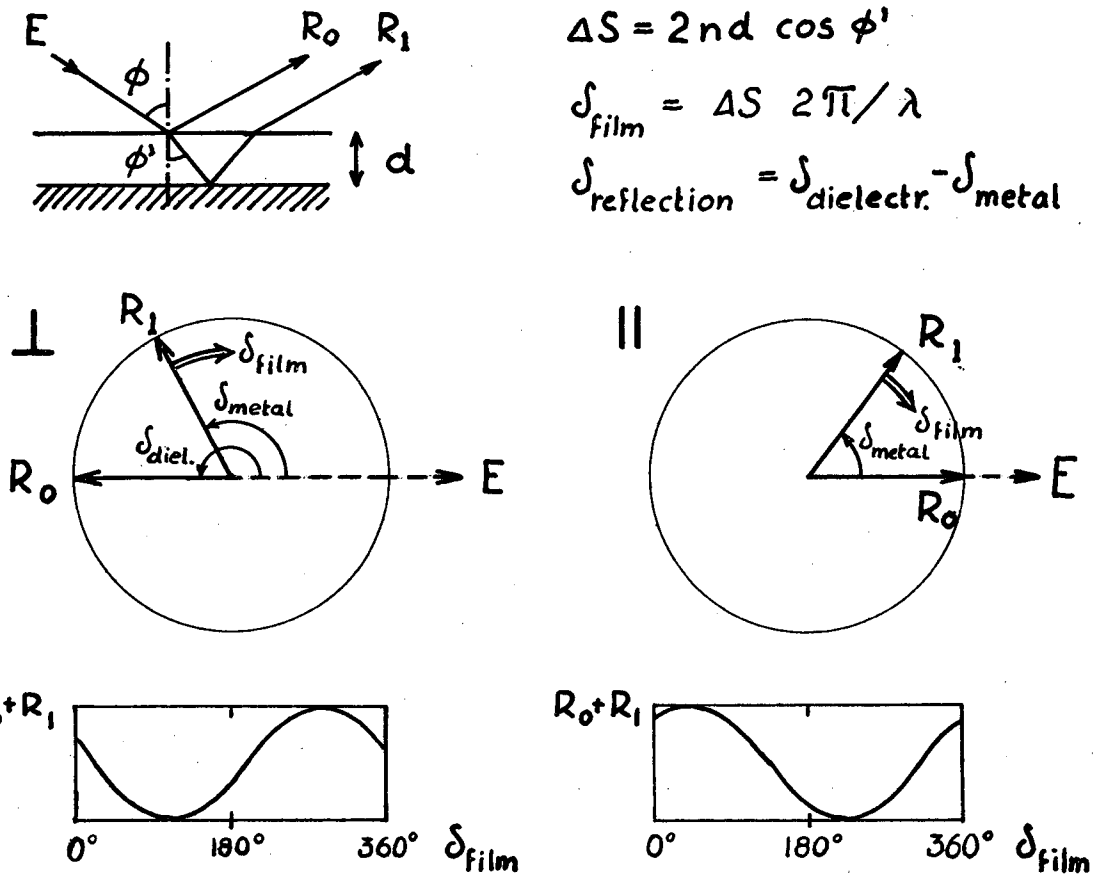

FILM INTERFERENCE, PHASE RELATIONSHIPS

MUB-6124

Fig. 57

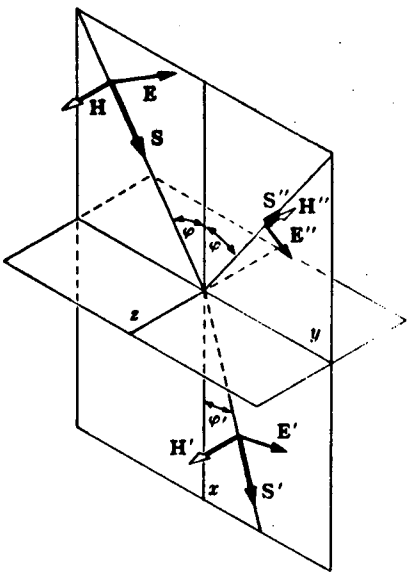

FIG. 8–9. Reflection and refraction of electromagnetic waves; **E** in the plane of incidence.

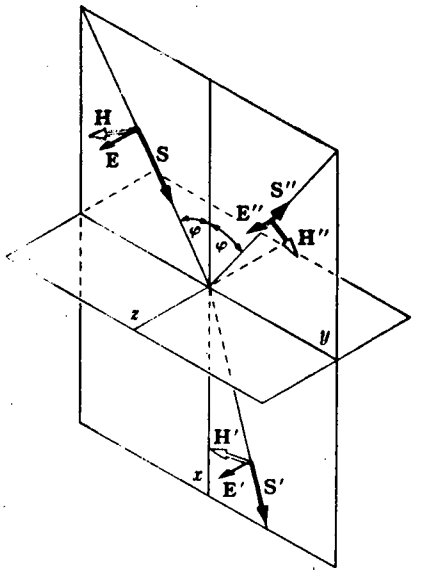

FIG. 8–10. Reflection and refraction of electromagnetic waves; **E** perpendicular to the plane of incidence.

MUB-6125

Fig. 58

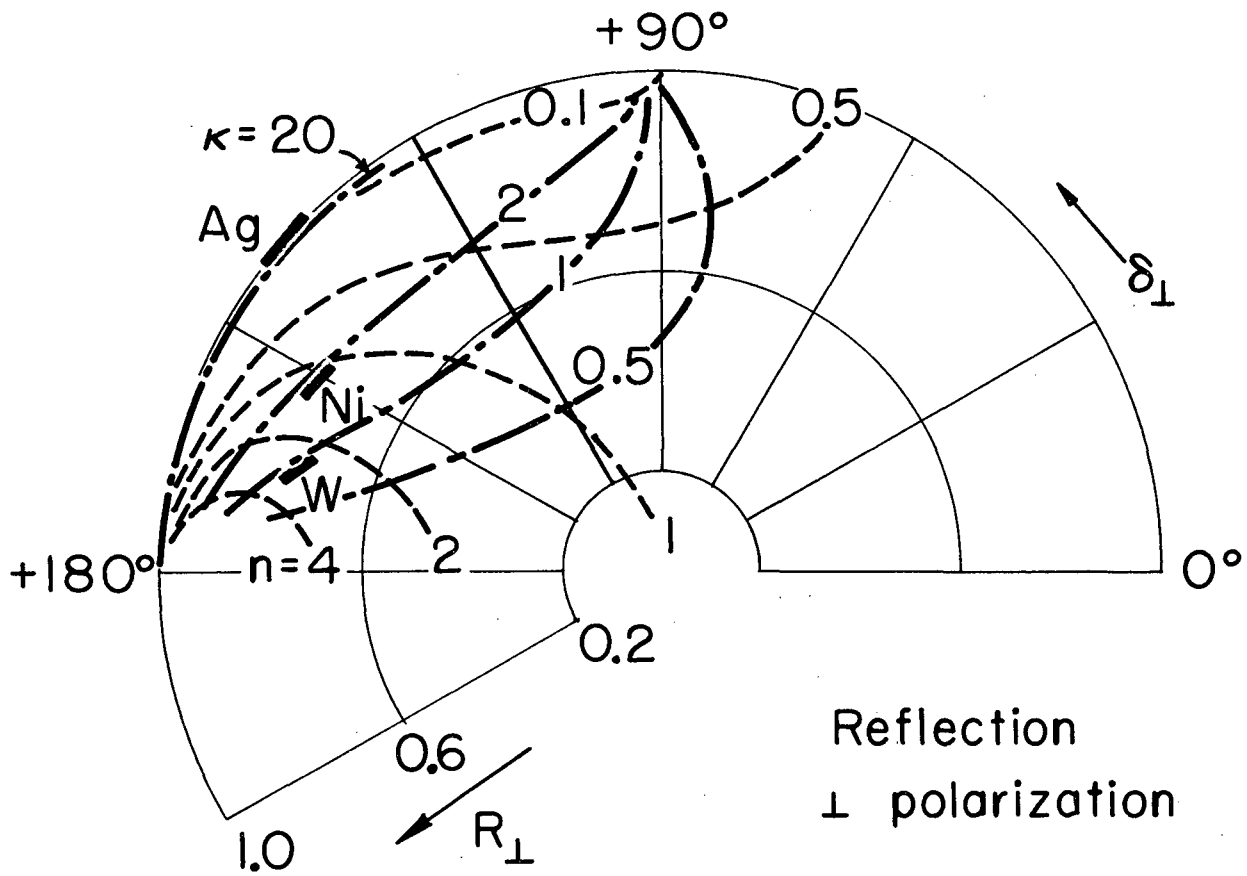

MUB-4080

Fig. 59

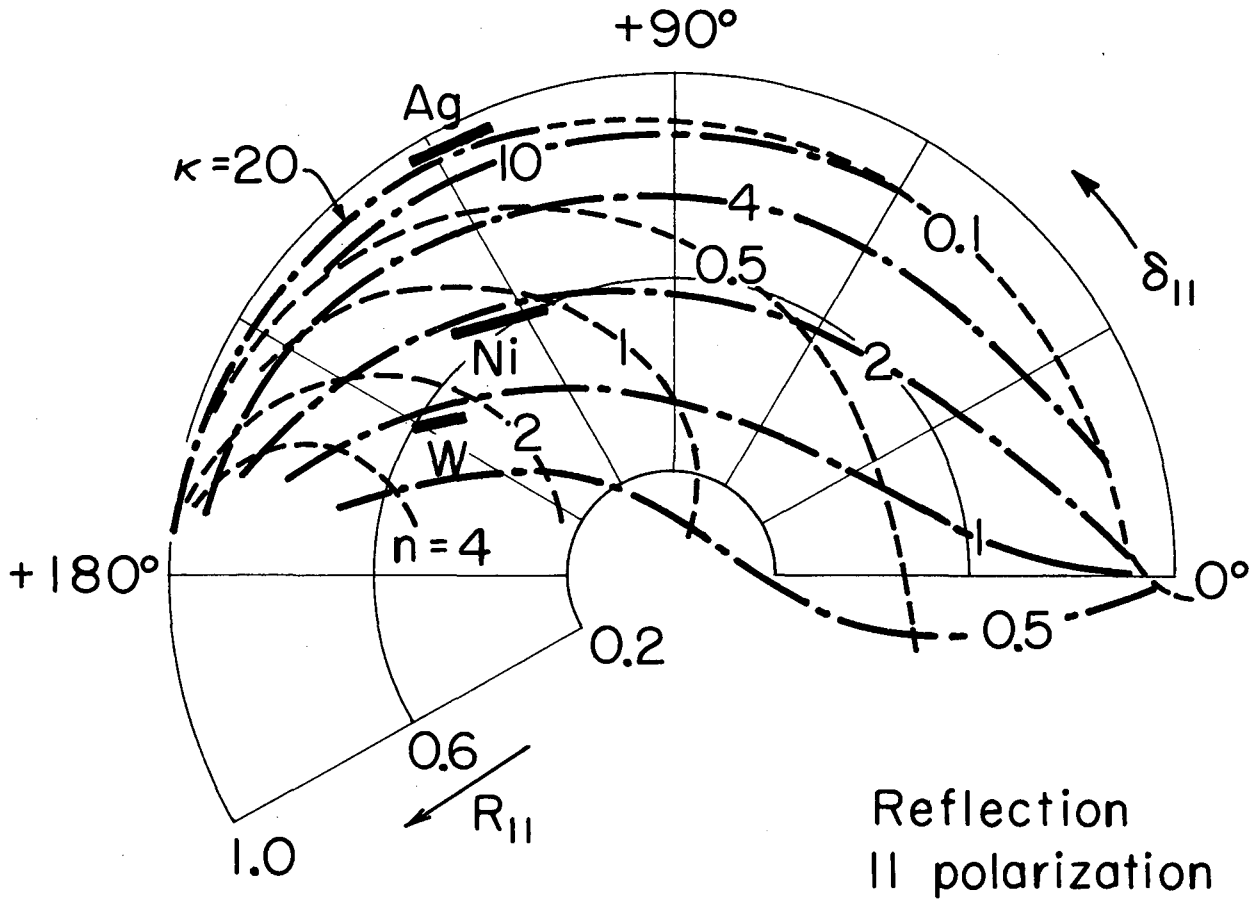

MUB-4081

Fig. 60

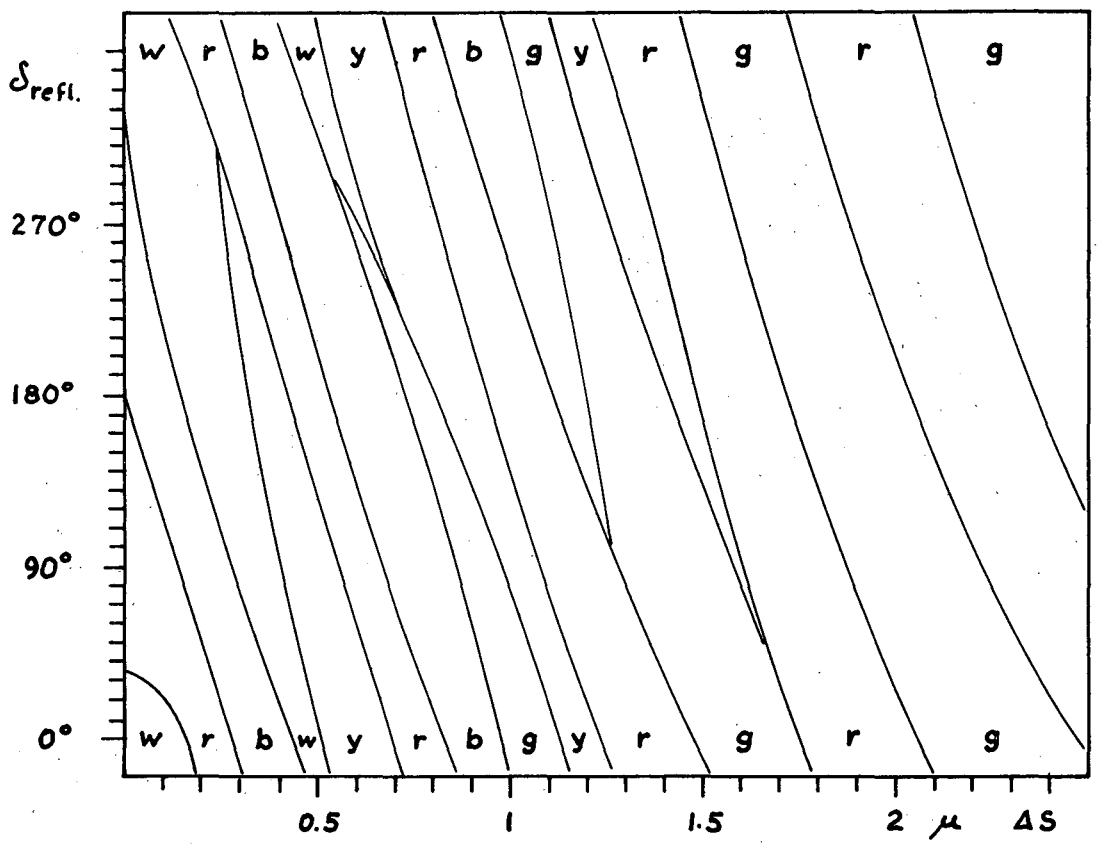

GENERALIZED SCALE OF INTERFERENCE COLORS

w = white, r = red, b = blue, y = yellow, g = green

MUB-6126

Fig. 61

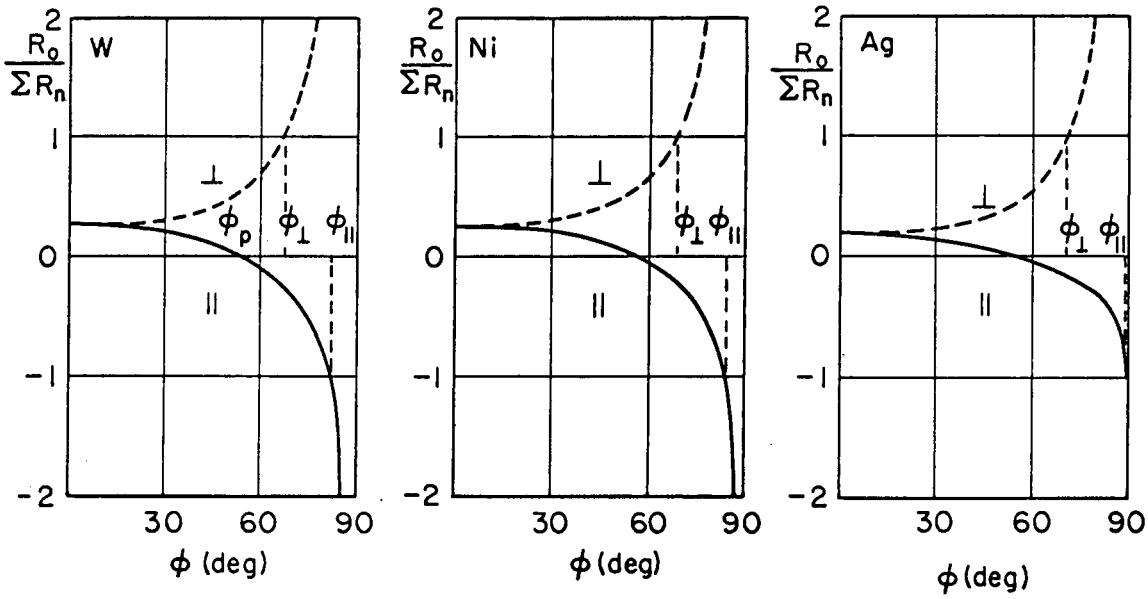

AMPLITUDE RATIO OF INTERFERING WAVES REFLECTED BY A TRANSPARENT THIN FILM (n_1 = 1.365) ON DIFFERENT METAL SURFACES

MUB-6127

Fig. 62

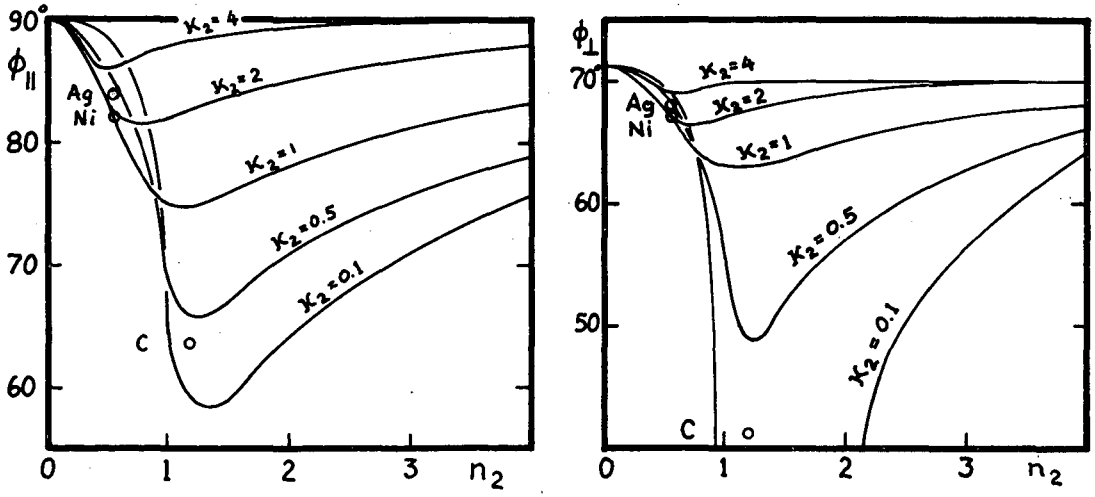

MU-35619

Fig. 63

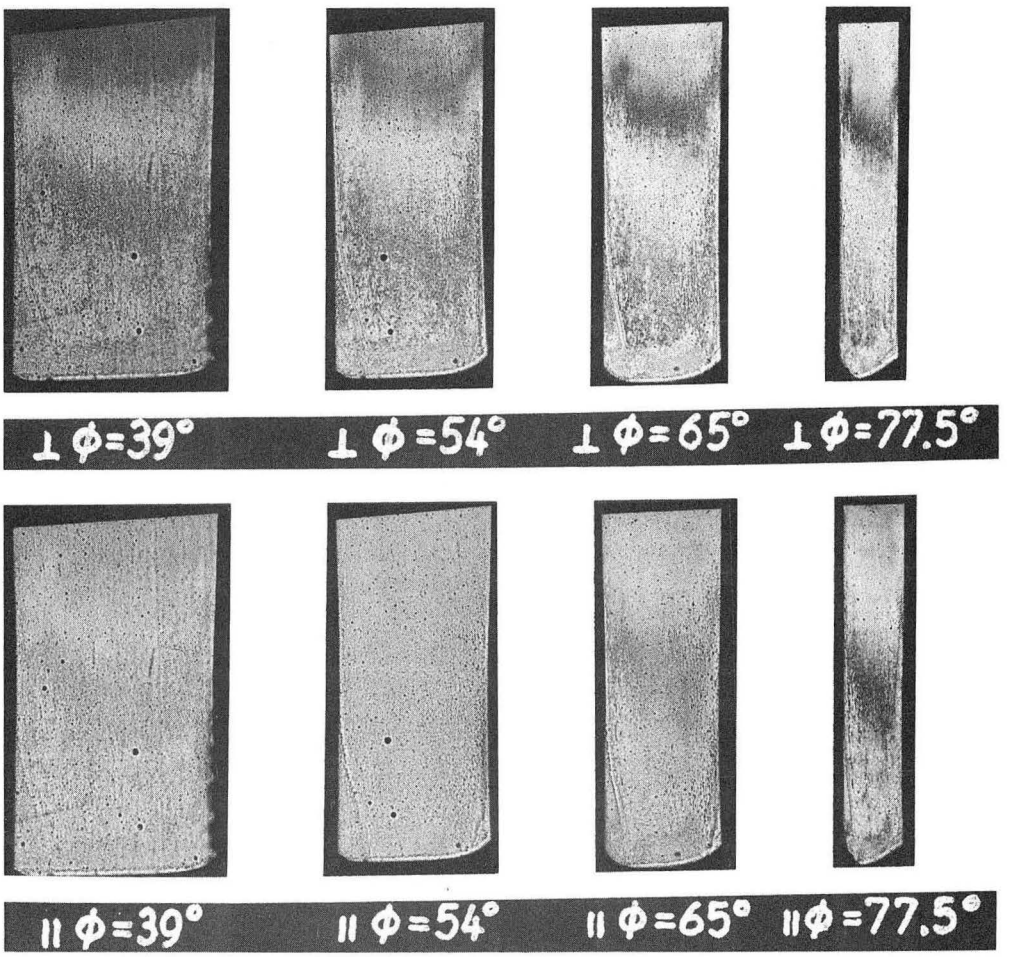

ZN-3960

Fig. 64

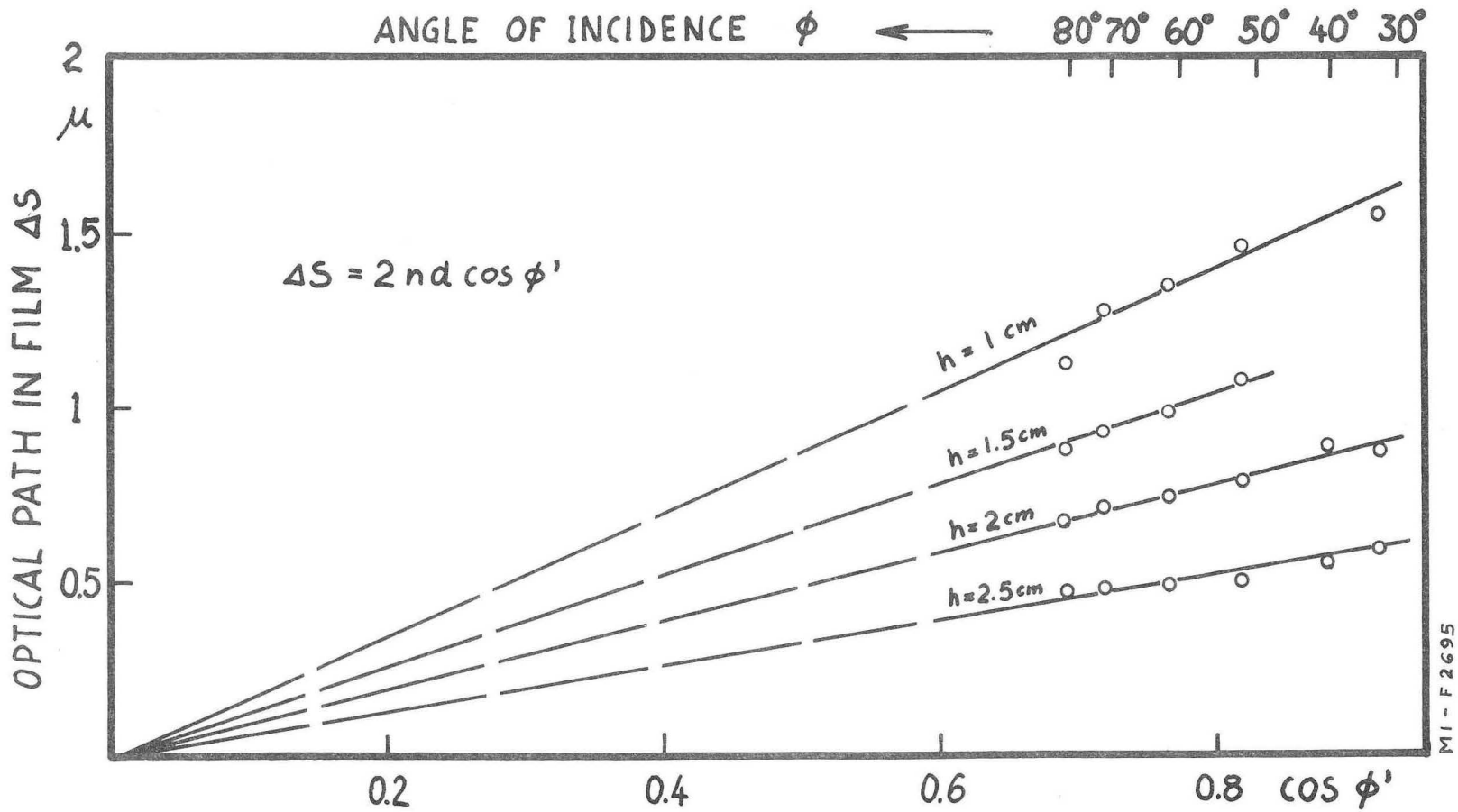

FILM INTERFERENCE UNDER DIFFERENT ANGLES OF INCIDENCE

MUB-6128

Fig. 65

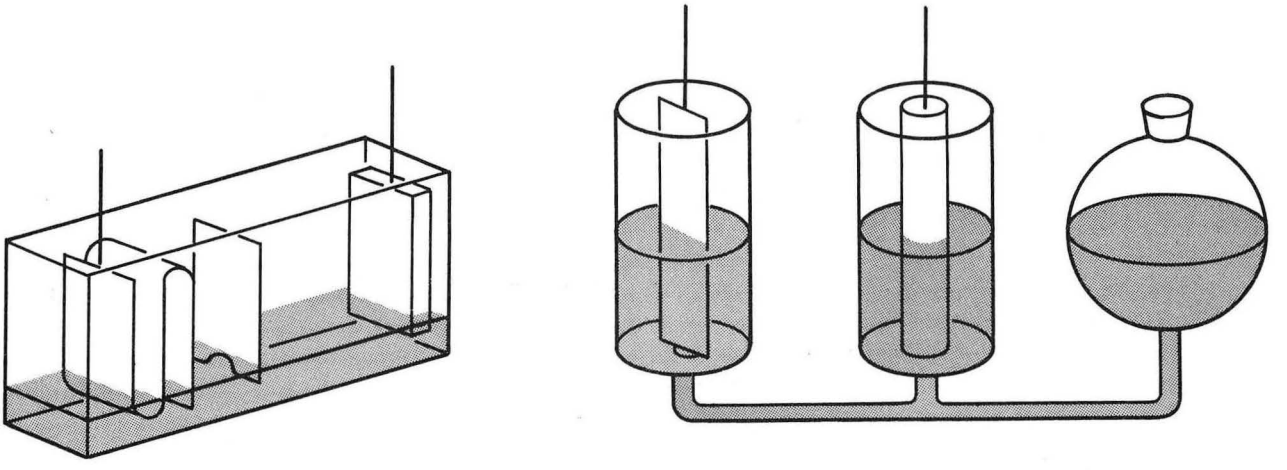

Electrolytic cells for film studies

MUB-5222

Fig. 66

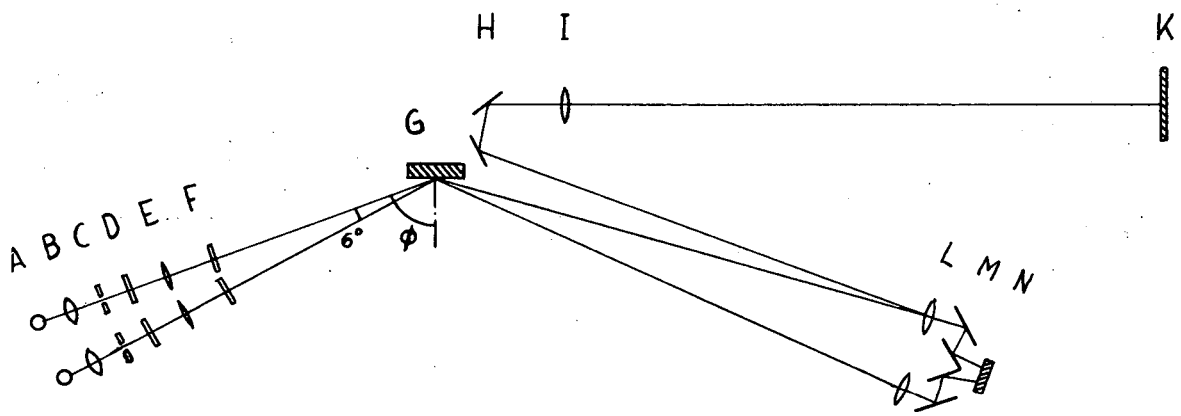

Fig. 67

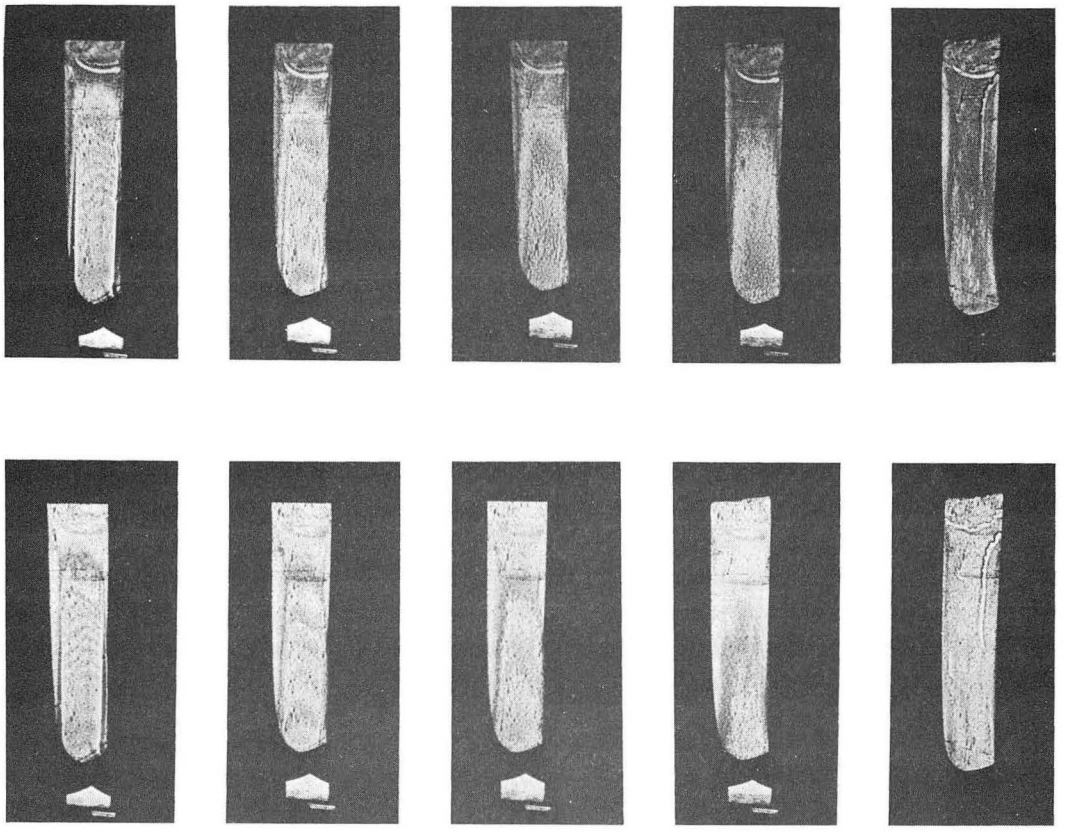

ZN-5144

Fig. 68

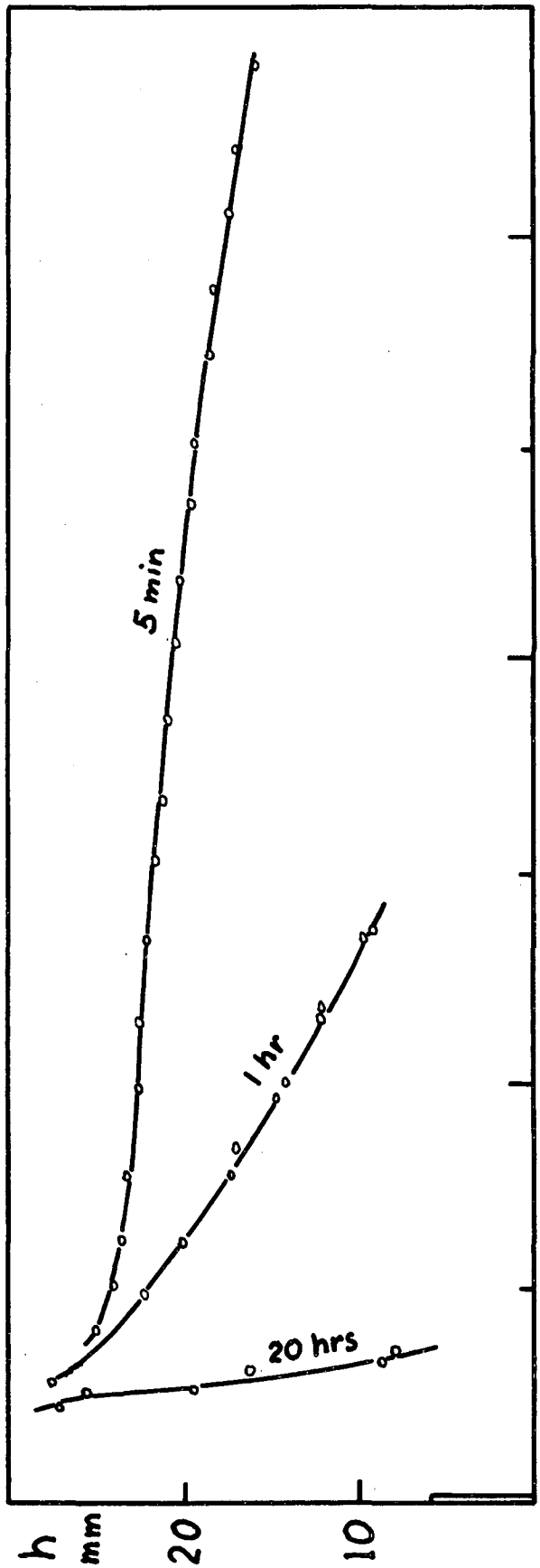

FORMATION OF ELECTROLYTE FILM ON UNPOLARIZED FLAT NICKEL ELECTRODE

3.5 N KOH, N_2

MUB-6129

Fig. 69

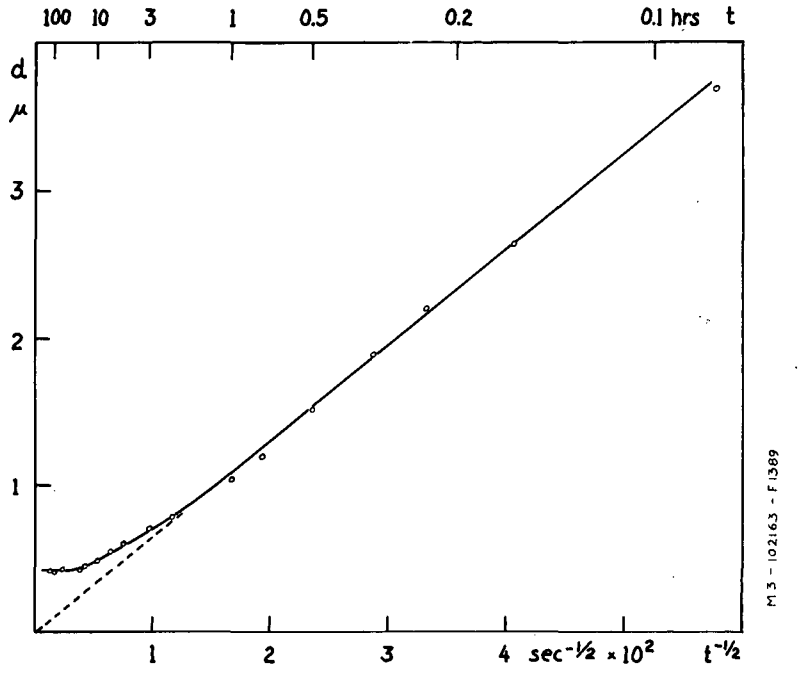

FORMATION OF KOH FILM ON POLISHED NICKEL SURFACE AFTER WITHDRAWAL FROM THE LIQUID
(3.4 M, h = 1.5 cm, N_2)

MU-35621

Fig. 70

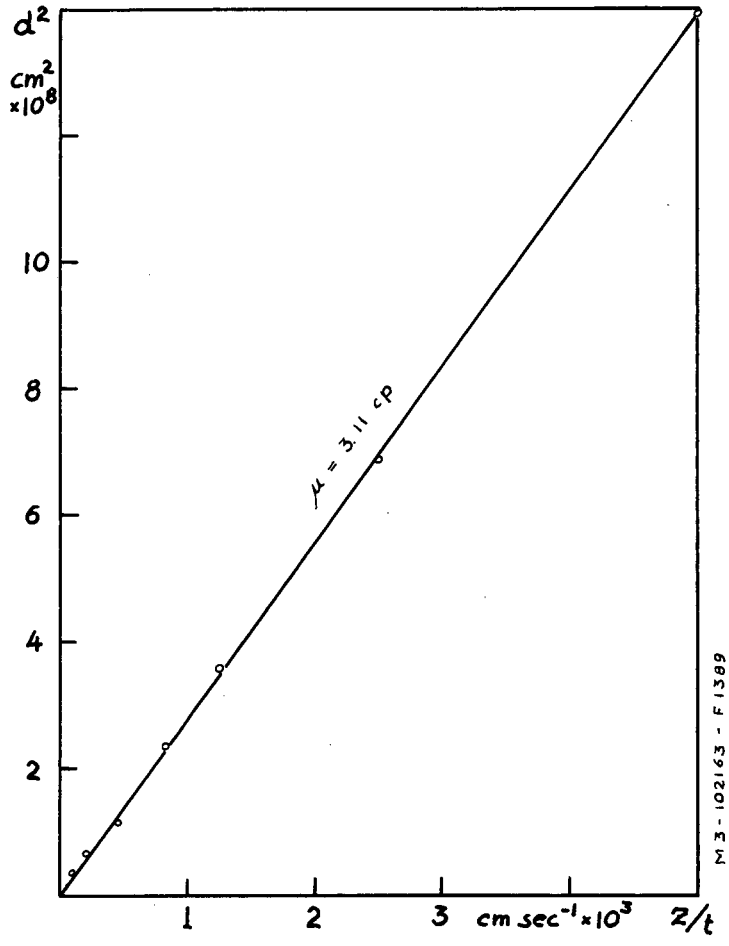

APPARENT VISCOSITY μ FROM FILM THINNING
(N_2, h = 15 mm)

MU-35622

Fig. 71

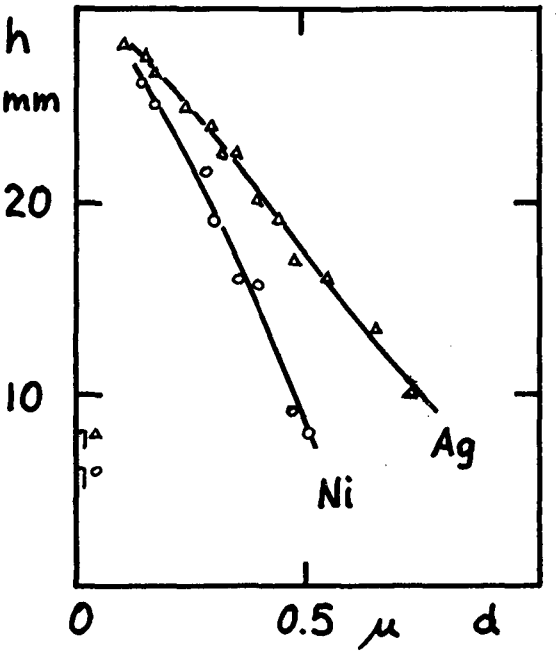

EQUILIBRIUM FILM PROFILES
ON DIFFERENT METALS

3.5 N KOH, O_2, 50 μA/cm

MUB-6130

Fig. 72

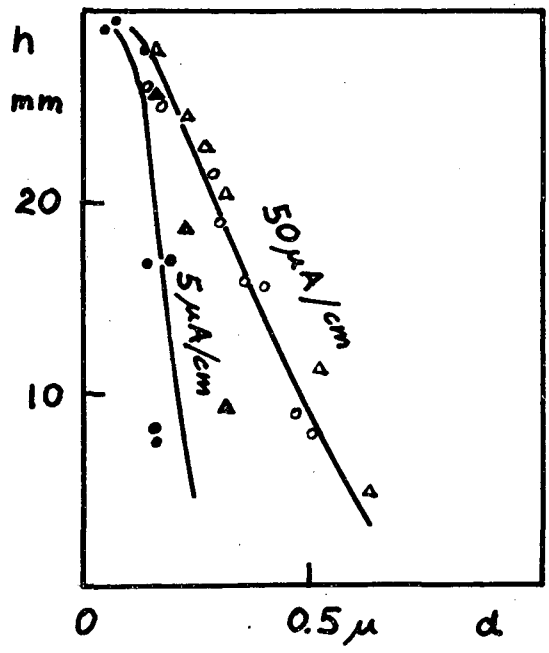

EQUILIBRIUM FILM PROFILES AT DIFFERENT CURRENT DENSITIES

NICKEL, 3.5N KOH, O_2, o FLAT △ CYLINDRICAL ELECTR.

MUB-6131

Fig. 73

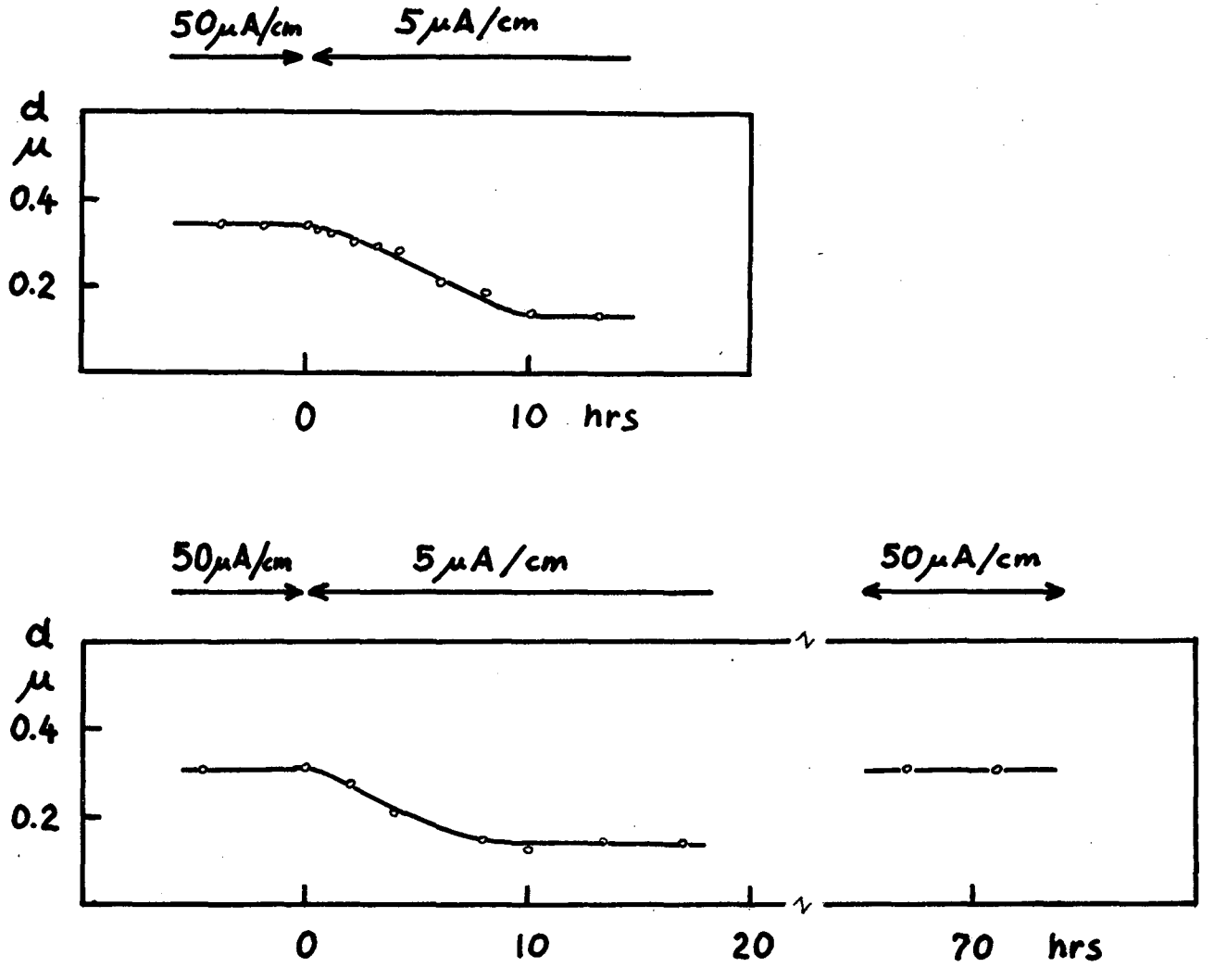

FILM RESPONSE TO VARIABLE POLARIZATION

FLAT AND CYLINDRICAL NICKEL ELECTRODES, 3.5 N KOH, O_2

MUB-6132

Fig. 74

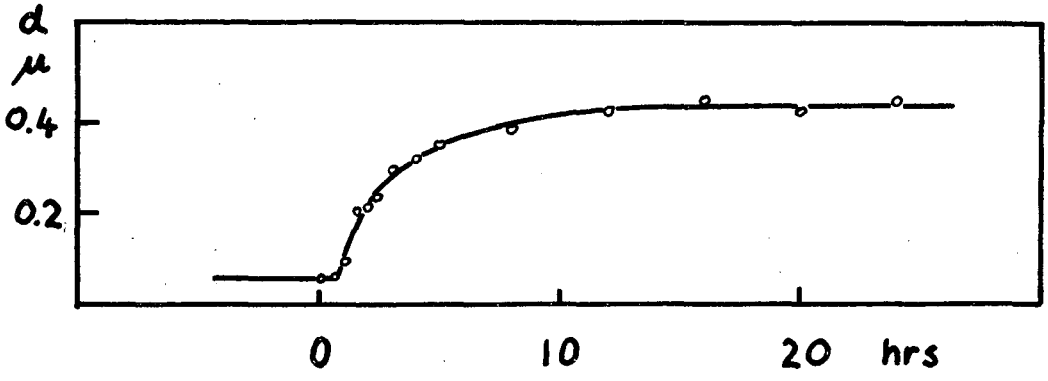

FILM GROWTH, NICKEL UNPOLARIZED

3.5 N KOH ON H_2O, h = 15 MM

MUB-6133

Fig. 75